

# NUMERICAL SIMULATION OF TORNADO-LIKE VORTICES

(Spine title: Numerical Simulation of Tornado-like Vortices)

(Thesis format: Integrated-Article)

by

Diwakar Natarajan

Graduate Program in Civil and Environmental Engineering

A thesis submitted in partial fulfillment  
of the requirements for the degree of  
Doctor of Philosophy

The School of Graduate and Postdoctoral Studies  
The University of Western Ontario  
London, Ontario, Canada

© Diwakar Natarajan 2011

THE UNIVERSITY OF WESTERN ONTARIO  
SCHOOL OF GRADUATE AND POSTDOCTORAL STUDIES

**CERTIFICATE OF EXAMINATION**

Supervisor

\_\_\_\_\_  
Dr. Horia Hangan

Examiners

\_\_\_\_\_  
Dr. Rupp Carriveau

\_\_\_\_\_  
Dr. Chao Zhang

\_\_\_\_\_  
Dr. Raouf Baddour

\_\_\_\_\_  
Dr. Ashraf El Damatty

The thesis by

**Diwakar Natarajan**

entitled:

**Numerical Simulation of Tornado-like Vortices**

is accepted in partial fulfillment of the  
requirements for the degree of  
Doctor of Philosophy

Date \_\_\_\_\_

\_\_\_\_\_  
Chair of the Thesis Examination Board

## **Abstract**

The thesis investigates by numerical simulation the flow characteristics of tornado like vortices produced by three types of vortex generators, namely, Ward-type Tornado Vortex Chamber (TVC), WinDEEE Dome and Atmospheric Vortex Engine (AVE).

Laboratory scale (Ward-type TVC) tornado-like vortices were simulated for swirl ratios 0.1 to 2.0 using the CFD code Fluent 6.3. The simulations with Reynolds stress model compare well with past experimental results. Multiple vortices were observed for high swirl ratios in LES simulation. These simulations have generated a comprehensive benchmark data for future modelers and experimenters.

The effects of translation and surface roughness on laboratory scale tornado-like vortices have been investigated. The simulated results show that the effect of translation is not uniform over the range of swirl ratios. For lower swirl ratios the translation reduces the maximum mean tangential velocity and for high swirl ratios it causes a slight increase in the maximum mean tangential velocity. The introduction of roughness reduces the mean tangential velocity at all swirl ratios, in other words the roughness causes an effect similar to reducing the swirl ratio.

Numerical simulations for the WinDEEE dome, a novel hexagonal wind tunnel, were performed. Suitable inlet and outlet configurations were identified. The study shows the feasibility for generating axi-symmetric (tornado-like and downburst-like) and straight flow wind profiles in the dome. Also presented are the results of numerical simulation of Atmospheric Vortex Engine (AVE), which is intended to generate a tornado-like vortex to capture the mechanical energy produced during upward heat convection. The results show that the prototype design of AVE is capable of generating a vortex flow in the atmosphere much above the AVE and the vortex acts as a physical chimney limiting the mixing of surrounding air into the rising plume of hot air. The geometrical parameters considered in the simulations provide a good starting point for future designs.

**Keywords:** Tornado, LES, RSM, Tornado Vortex Chamber, Swirl ratio, Surface roughness, Vortex translation, WinDEEE dome, Atmospheric Vortex Engine

## **Co-Authorship**

Chapter 4: This chapter presents numerical simulation of WindEEE dome facility. The WindEEE dome concept was developed by Dr. Horia Hangan. The numerical simulations were done by both Diwakar Natarajan and AIOLOS consultants. The data analysis presented here were performed by Diwakar Natarajan

Chapter 5: This chapter presents the numerical simulation of Atmospheric Vortex Engine (AVE). The AVE concept was developed by Louis Michaud. The numerical simulations and data analysis presented here were performed by Diwakar Natarajan.

## **Acknowledgements**

I would like to thank Dr. Horia Hangan for introducing me to this wonderful field of Computational Fluid Dynamics. This dissertation would not have been possible without his guidance and support. Dr Jongdae Kim deserves special thanks for his helpful suggestions during the initial phase of the research.

I am indebted to all the past and present members of Dr. Hangan's research team for their constructive comments and suggestions. I am also thankful to Anthony Burggraaf for the computer related technical support and Karen Norman for assistance with administrative work.

I would also like to acknowledge the Civil and Environmental Engineering Department and Manitoba Hydro for their financial support during my doctoral program.

There are a lot of people who made my stay in London very memorable and enjoyable. I would like to thank my friends – Bilal, Padma, Sampat, Sundaram, Shyam and Sathya. They made me feel at home and our weekend get-togethers helped me to unwind and relax.

Finally, I would like to thank my parents Rajam and Natarajan, my brother Arun and my sister-in-law Gayathri for their love, encouragement and support.

# CONTENTS

	Page No.
<b>Certificate of Examination</b>	... ii
<b>Abstract</b>	... iii
<b>Co-Authorship</b>	... v
<b>Acknowledgement</b>	... vi
<b>List of Tables</b>	... xi
<b>List of Figures</b>	... xii
<b>List of Symbols and Abbreviations</b>	... xxi
 <b>Chapter 1 Introduction</b>	 ... 1
1.1 General introduction	... 1
1.2 Scope and objective of thesis	... 2
1.3 Thesis format	... 5
1.4 Reference	... 5
 <b>Chapter 2 Numerical Simulation of Laboratory Scale Tornado-like Flows</b>	 ... 9
2.1 Introduction	... 9
2.1.1 Laboratory models	... 10
2.1.2 Numerical models	... 11
2.2 RSM simulations	... 14

2.2.1 Numerical Setup	...	14
2.2.2 Benchmarking	...	16
2.2.3 Mean velocity profiles	...	17
2.2.4 Pressure Deficit	...	20
2.2.5 Core radius	...	22
2.3 LES Simulation	...	24
2.3.1 Numerical setup	...	24
2.3.2 Multiple vortices	...	24
2.3.3 Turbulence characteristics	...	25
2.4 Conclusion	...	26
2.5 Reference	...	27
<b>Chapter 3 Effects of translation and surface roughness on tornado-like vortices</b>	...	54
3.1 Introduction	...	54
3.2 Translation Effects	...	55
3.2.1 Numerical Setup	...	55
3.2.2 Results and Discussion	...	56
3.2.2.1 Low swirl ratio	...	57
3.2.2.2 High swirl ratio	...	58
3.3 Surface Roughness Effects	...	58



3.3.1 Equivalent sand grain roughness model	...	59
3.3.1.1 Numerical setup	...	61
3.3.1.2 Results and Discussions	...	63
3.3.2 Physical modeling of roughness blocks	...	64
3.3.2.1 Numerical Setup	...	64
3.3.2.2 Results and discussion	...	65
3.4 Conclusion	...	65
3.5 Reference	...	66
<b>Chapter 4 Numerical Simulation of WindEEE Dome Facility</b>	...	81
4.1 Introduction	...	81
4.2 Preliminary Design	...	82
4.2.1 Numerical Setup	...	82
4.2.2 Downburst	...	83
4.2.3 Tornado	...	84
4.3 Design optimization	...	86
4.3.1 Numerical setup	...	88
4.3.2 Downburst	...	89
4.3.3 Tornado	...	90
4.3.4 Straight flow	...	92

4.4 Conclusion	...	93
4.5 References	...	94
<b>Chapter 5 Numerical Simulation of Atmospheric Vortex Engine</b>	...	107
5.1 Introduction	...	107
5.2 Numerical simulation	...	108
5.2.1 Preliminary laminar simulations on model-scale AVE	...	110
5.2.2 $k-\varepsilon$ simulations on model-scale AVE	...	111
5.2.3 Design optimization	...	111
5.2.4 Full-scale AVE simulations with cross wind	...	112
5.3 Conclusion	...	113
5.4 Reference	...	114
<b>Chapter 6 Conclusion</b>	...	128
<b>Appendix A</b> RANS turbulence modeling	...	133
<b>Appendix B</b> LES turbulence modeling	...	140
<b>Appendix C</b> Rayleigh number calculation for AVE simulations	...	142
<b>Curriculum Vitae</b>	...	143

## LIST OF TABLES

			Page No.
<b>Chapter 2</b>			
Table 2.1(a)	Boundary conditions used in the current simulations	...	33
Table 2.1(b)	Domain dimensions used in the current simulations	...	33
<b>Chapter 4</b>			
Table 4.1	Boundary conditions for the preliminary WindEEE dome domain for the simulations of tornado-like and downburst-like flows	...	96
Table 4.2	The H/D ratio and Reynolds number for the three downburst cases simulated using the preliminary WindEEE dome domain.	...	96
Table 4.3	Boundary conditions for the tornado, downburst and straight flow simulations in the modified WindEEE dome domain	...	96
<b>Chapter 5</b>			
Table 5.1	Dimensional specifications for prototype model-scale AVE	...	116
Table 5.2	Dimensional specifications for prototype full-scale AVE	...	116
Table 5.3	Boundary conditions for both model-scale and full-scale AVE simulations	...	117

## LIST OF FIGURES

		Page No.
<b>Chapter 2</b>		
Figure 2.1	Sketch of the pathlines flow observed at various swirl ratios. Lugt (1989), Davies-Jones (1986)	... 34
Figure 2.2	Sketch of a Ward-type TVC (Church et.al. 1979)	... 34
Figure 2.3	Sketch of an Iowa-type TVC (Haan Jr, 2007)	... 35
Figure 2.4	Sketch of the four regions of the low swirl vortex flow. (Wilson and Rotunno 1986)	... 35
Figure 2.5a	Schematic diagram of the cross section of Ward type Purdue TVC with blue region showing domain modeled in the current simulations. (Adapted from Church et.al. 1979)	... 36
Figure 2.5b	Schematic diagram of the domain modeled in the current simulations.	... 36
Figure 2.6	Plots comparing the radial velocity of the current CFD simulation and Baker (1981) experimental results. (a) $S = 0.28$ , $R/R_0 = 0.1025$ (b) $S = 0.28$ , $R/R_0 = 0.2125$ .	... 37
Figure 2.7	Plots comparing the tangential velocity of the current CFD simulation and Baker (1981) experimental results. (a) $S = 0.28$ , $R/R_0 = 0.1025$ (b) $S = 0.28$ , $R/R_0 = 0.2125$ .	... 37
Figure 2.8	Plots comparing the axial velocity of the current CFD simulation and Baker (1981) experimental results. (a) $S = 0.28$ , $R/R_0 = 0.1025$ (b) $S = 0.28$ , $R/R_0 = 0.2125$ .	... 38
Figure 2.9	Sketch of flow observed in no-swirl $S = 0$ case. (Church et al. 1979)	... 38
Figure 2.10	Contour plot of the velocity for Swirl ratios $S = 0.2, 0.28$ ,	... 39

0.5, 0.8, 1.0, 2.0.

Figure 2.11	Velocity profile for Swirl ratio $S = 0.28$ (a) Azimuthally averaged axial, radial and tangential velocity along the radial distance at height $Z_{\max}$ (Height of maximum tangential velocity) (b) Azimuthally averaged axial, radial and tangential velocity along the height at radial locations inside and outside the core of the tornado.	...	40
Figure 2.12	Velocity profile for Swirl ratio $S = 0.5$ (a) Azimuthally averaged axial, radial and tangential velocity along the radial distance at height $Z_{\max}$ (Height of maximum tangential velocity) (b) Azimuthally averaged axial, radial and tangential velocity along the height at radial locations inside and outside the core of the tornado.	...	41
Figure 2.13	Velocity profile for Swirl ratio $S = 0.8$ (a) Azimuthally averaged axial, radial and tangential velocity along the radial distance at height $Z_{\max}$ (Height of maximum tangential velocity) (b) Azimuthally averaged axial, radial and tangential velocity along the height at radial locations inside and outside the core of the tornado.	...	42
Figure 2.14	Velocity profile for Swirl ratio $S = 1.5$ (a) Azimuthally averaged axial, radial and tangential velocity along the radial distance at height $Z_{\max}$ (Height of maximum tangential velocity) (b) Azimuthally averaged axial, radial and tangential velocity along the height at radial locations inside and outside the core of the tornado.	...	43
Figure 2.15	Surface pressure deficit along the radial distance for different swirl ratios (a) $S = 0.1, 0.2, 0.28, 0.4, 0.5$ , and $0.6$ (b) $S = 0.7, 0.8, 0.9, 1.0, 1.5$ , and $2.0$	...	44

Figure 2.16	The plot of maximum central pressure deficit vs. swirl ratio	...	45
Figure 2.17	The plot of maximum pressure deficit at $R/R_0 = 0$ along the normalized height for swirl ratios $S = 0.1, 0.2, 0.28, 0.5, 0.8, 1.0$ .	...	45
Figure 2.18	The plot of normalized core radius ( $R_{\max}/R_0$ ) and the normalized height from the base at which the radius is measured ( $Z_{\max}/R_0$ ) for various Swirl ratios (0.2-2.0)	...	46
Figure 2.19	Contour plot of tangential velocity for Swirl ratio $S = 0.2, 0.5, 0.8, 1.0, 2.0$	...	47
Figure 2.20	LES velocity contours for $S = 1.0$ at $Z/R_0 = 0.02$	...	48
Figure 2.21	LES velocity contours for $S = 2.0$ at $Z/R_0 = 0.02$	...	49
Figure 2.22	The plot of RMS velocities and Reynolds shear stress along the height for Swirl ratio $S = 0.28$ at radial locations inside the core ( $R < R_{\max}$ ) at $R/R_0 = 0.016$ and outside the core ( $R > R_{\max}$ ) at $R/R_0 = 0.08$ .	...	50
Figure 2.23	The plot of RMS velocities and Reynolds shear stress along the height for Swirl ratio $S = 0.5$ at radial locations inside the core ( $R < R_{\max}$ ) at $R/R_0 = 0.02$ and outside the core ( $R > R_{\max}$ ) at $R/R_0 = 0.14$ .	...	51
Figure 2.24	Turbulence characteristics for $S = 1.0$	...	52
Figure 2.25	Turbulence characteristics for $S = 2.0$	...	53

### Chapter 3

Figure 3.1	Contour plots of velocity magnitude in the XZ plane for tornadic flow with translation. ( $V_T = 1.07$ m/s)	...	69
------------	---	-----	----

Figure 3.2	Normalized tangential velocity along the normalized radial distance for various swirl ratios of stationary (T0) and translating (T2) tornado-like vortices at height $Z/R_0 = 0.02$ .	...	70
Figure 3.3	Base surface pressure coefficients for various swirl ratios of stationary (T0) and translating (T2) tornado-like vortices.	...	71
Figure 3.4	LES velocity contours for $S = 1.0$ with translation velocity $V_T = 1.07$ m/s, at height $Z/R_0 = 0.02$	...	72
Figure 3.5	LES velocity contours for $S = 2.0$ with translation velocity $V_T = 1.07$ m/s, at height $Z/R_0 = 0.02$	...	73
Figure 3.6	Turbulence characteristics for $S = 2.0$ with translation $V_T = 1.07$ m/s	...	74
Figure 3.7	Computational domain for simulating the effects of surface roughness using equivalent sand grain roughness model.	...	75
Figure 3.8	Normalized axial velocity along the normalized height for different radial location for swirl ratio 0.1	...	75
Figure 3.9	Normalized radial velocity along the normalized height for different radial location for swirl ratio 0.1	...	76
Figure 3.10	Normalized tangential velocity along the normalized height for different radial location for swirl ratio 0.1	...	76
Figure 3.11	Normalized axial velocity along the normalized height for different radial location for swirl ratio 2.0	...	77
Figure 3.12	Normalized radial velocity along the normalized height for different radial location for swirl ratio 2.0	...	77
Figure 3.13	Normalized tangential velocity along the normalized height	...	78

	for different radial location for swirl ratio 2.0		
Figure 3.14	Sketch showing the physically modeled rough surface. (a) The base wall of the domain with the roughness blocks. (b) The roughness block.	...	78
Figure 3.15	Maximum time-averaged central base pressure deficit vs. swirl ratio smooth (Y0) and rough surface (Y2).	...	79
Figure 3.16	Maximum time-averaged tangential velocity vs. swirl ratio for smooth (Y0) and rough surface (Y2).	...	79
Figure 3.17	Core radius along the height for various swirl ratios of smooth (Y0) and rough (Y2) surface tornadoes.	...	80

## Chapter 4

Figure 4.1	The computational domain: the inner chamber of WindEEE dome.	...	97
Figure 4.2	The plot of normalized radial velocity vs. normalized height at $R/D = 1$ , the numerical result of Kim and Hangan (2007) was for a $Re = 2,000,000$ , $H/D = 4$ .	...	97
Figure 4.3	The plot of normalized radial velocity vs. normalized height at various $R/D$ ratios, the experimental results of Hangan and Xu (2005) were for a $Re = 27,000$ , $H/D = 4$ and the current CFD results were for $Re = 2,251,656$ , $H/D = 4$ .	...	98
Figure 4.4	Conceptual schematic of inlet condition for tornado-like flows (a) Guide louver method: (b) Horizontal shear method	...	98
Figure 4.5	The contour plot of the velocity magnitude (m/s) of the current CFD simulation of tornado in the WindEEE dome	...	99



showing the two-celled tornado.

Figure 4.6	The plot of normalized tangential velocity vs. the normalized radial distance, comparing the current CFD simulation of tornado for the preliminary dome design (Case1: guide louver type input) and the real scale tornado velocities measured with Doppler radar.	...	99
Figure 4.7	The plot of normalized tangential velocity vs. the normalized radial distance, comparing the current CFD simulation of tornado for the preliminary dome design (Case2: horizontal shear type input) and the real scale tornado velocities measured with Doppler radar.	...	100
Figure 4.8	The modified inner chamber of WindEEE dome.	...	100
Figure 4.9	The computational domain: Downburst-like flow simulation.	...	101
Figure 4.10	The computational domain: Tornado-like flow simulation.	...	101
Figure 4.11	The computational domain: Straight flow simulation.	...	102
Figure 4.12	The velocity vectors in the vertical plane showing the ring vortex evolution in the downburst flow at different non-dimensional time frames a) $T = 0.9$ , b) $T = 1.8$ , c) $T = 2.7$ , d) $T = 3.6$ , e) $T = 4.5$ , f) $T = 5.4$	...	103
Figure 4.13	The plot of normalized radial velocity vs. the normalized radial distance, comparing the current CFD simulation of downburst flow for the modified domain and the semi-empirical model for downburst flow by Holmes and Oliver (2000).	...	104
Figure 4.14	The plot of normalized tangential velocity vs. the normalized radial distance, comparing the current CFD	...	104

simulation of tornado for the modified domain and the real scale tornado velocities measured with Doppler radar.

Figure 4.15	The plot of normalized velocity vs. the normalized height at core radius $R_{\max}$ , comparing the current CFD simulation of tornado in the WindEEE dome and the CFD simulation of tornado of a Ward type TVC. (TV: Tangential velocity, RV: Radial velocity, AV: Axial velocity)	...	105
Figure 4.16	The computational domain: straight flow with side slotted walls.	...	105
Figure 4.17	The plot of velocity vs. span-wise horizontal distance at mid height (2 m) at different length-wise distances ( $X=2.5\text{m}$ , $7.5\text{m}$ , and $12.5\text{m}$ ) from the wall (with the array of fans) for the straight flow.	...	106
Figure 4.18	The plot of velocity vs. span-wise horizontal distance at mid-section ( $X = 12.5\text{ m}$ ) at different heights ( $Z= 1\text{m}$ , $2\text{m}$ , and $3\text{m}$ ) from the base wall for the straight flow.	...	106

## Chapter 5

Figure 5.1	The radial and tangential velocity along the height at the core radius of a typical numerically simulated laboratory scale tornado.	...	118
Figure 5.2a	Geometry of the prototype AVE used in the current simulations (Elevation)	...	118
Figure 5.2b	Geometry of the prototype AVE used in the current simulations (Plan view)	...	119
Figure 5.3	The computational domain	...	119

Figure 5.4	The contour plot of tangential velocity (m/s) in the YZ plane for model-scale AVE (Laminar Simulations)	...	120
Figure 5.5	The vector plot of velocity magnitude (m/s) in the Z=0.4m plane for model-scale AVE (Laminar Simulations)	...	120
Figure 5.6	The contour plot of temperature (K) in the YZ plane for model-scale AVE (Laminar Simulations)	...	121
Figure 5.7	The contour plot of velocity magnitude (m/s) in the YZ plane for model-scale AVE (Laminar Simulations)	...	121
Figure 5.8	The contour plot of static pressure (Pa) in the YZ plane for model-scale AVE (Laminar Simulations)	...	122
Figure 5.9	The contour plot of velocity magnitude (m/s) in the YZ plane for model-scale AVE (Turbulent Simulations)	...	122
Figure 5.10	The contour plot of tangential velocity (m/s) in the YZ plane for model-scale AVE (Turbulent Simulations)	...	123
Figure 5.11	The contour plot of velocity magnitude (m/s) in the YZ plane for model-scale AVE with increased roof opening diameter D3 (Turbulent Simulations)	...	123
Figure 5.12	The contour plot of velocity magnitude (m/s) in the YZ plane for the extended domain (Z = 6000mm) model-scale AVE (Turbulent Simulations)	...	124
Figure 5.13	The contour plot of temperature (K) in the YZ plane for the extended domain (Z = 6000mm) model-scale AVE (Turbulent Simulations)	...	124
Figure 5.14	The contour plot of velocity magnitude (m/s) in the YZ plane for model-scale AVE with increased temperature difference between the inlet air and ambient air ( $\Delta T = 30$	...	125

## K) (Turbulent Simulations)

Figure 5.15	The contour plot of velocity magnitude (m/s) in the YZ plane for the full-scale AVE	...	125
Figure 5.16	The contour plot of static pressure (Pa) in the YZ plane for the full-scale AVE	...	126
Figure 5.17	The contour plot of velocity magnitude (m/s) in the YZ plane for the full-scale AVE with cross wind	...	126
Figure 5.18	The contour plot of temperature (K) in the YZ plane for the full-scale AVE with cross wind	...	127
Figure 5.19	The contour plot of static pressure (Pa) in the YZ plane for the full-scale AVE with cross wind	...	127

## Symbols and Abbreviations

### Chapter 2

A	Aspect ratio
$C_p$	Pressure coefficient
CAPE	Convective Available Potential Energy
$H_0$	Depth of inflow in a tornado vortex chamber
LDV	Laser Doppler Velocimeter
LES	Large Eddy Simulations
$\nu$	Kinematic viscosity of air
$P_0$	Static pressure
RANS	Reynolds Averaged Navier-Stokes (equation)
RSM	Reynolds Stress Model
$R_{\max}$	Core radius, the radius at which the maximum tangential velocity occurs
$R_0$	Radius of updraft
$\rho$	Density of air
S	Swirl ratio
TI	Turbulence Intensity
TVC	Tornado Vortex Chamber
TVR	Turbulence Viscosity Ratio
UDF	User Defined Function

$U_0$	(Average) radial velocity at $R_0$
$U_1$	Reference velocity
$U_{\text{rms}}$	Root mean square of the fluctuating radial velocity
$U_{R0}$	Radial velocity at inlet
$u^*$	Friction velocity
VBD	Vortex Break Down
VTD	Vortex Touch Down
$V_{\text{max}}$	Maximum tangential velocity (time averaged)
$V_{\text{rms}}$	Root mean square of the fluctuating tangential velocity
$V_{R0}$	Tangential velocity at inlet
$W_{\text{rms}}$	Root mean square of the fluctuating axial velocity
$z$	Distance to the wall
$Z$	Height
$z_1$	Reference height
$Z_{\text{max}}$	Height at which the maximum tangential velocity occurs

### Chapter 3

$C_\mu$	Constant with default value 0.09
$\Delta B$	Roughness function intercept
$E$	An empirical constant of the wall function (for the smooth wall with a value 9.793)

$\kappa$	von Karman constant ( $\sim 0.41$ )
$\kappa$	Turbulent kinetic energy
$\kappa_p$	Turbulent kinetic energy at centre point of wall adjacent cell
$(1/\kappa)$	Slope of universal near-wall velocity distribution (log law)
$K_s$	Equivalent sand grain roughness height
$K_s^+$	dimensionless sand grain roughness height
$\tau_w$	Wall shear stress
$U_h$	Reference velocity (for Equations 8 and 9 in chapter 2, (Richards and Hoxey (1993))
$U_p$	Velocity at the centre point of the wall adjacent cell
$u_{ABL}^*$	ABL friction velocity
$V_T$	Translation velocity ( along the positive x-direction)
$y_0$	Aerodynamic roughness lengths
$y_p$	Height of the centre point of the wall adjacent cell
$z_h$	Reference height (for Equations 8 and 9 in chapter 2, (Richards and Hoxey (1993))

#### Chapter 4

CFI	Canadian Foundation for Innovation
D	Diameter of circular opening (Roof opening)
d	Diameter of side wall Fan (Preliminary design)
d1	Diameter of side wall Fan (Modified design)

$d_2$	Diameter of plenum Fan (Modified design)
$D_{Hex}$	Inner diameter of hexagonal test chamber
$D_p$	Diameter of hexagonal top plenum
$H$	Base to roof height of hexagonal test chamber
$\theta$	Guide louver angle
ORF	Ontario Research Fund
$Re$	Reynolds number
SST-KW	Shear-stress transport KW model
$U_{Fan}$	Speed of the fan
$U_{in}$	Normal velocity at the inlet
$V_{in}$	Tangential velocity at the inlet
$V_{Jet}$	Inlet jet velocity
WindEEE	Wind Engineering, Energy and Environment Dome

## Chapter 5

AVE	Atmospheric Vortex Engine
$\beta$	Thermal expansion coefficient
$d_1$	Deflector diameter ring
$\Delta T$	Temperature difference between actual and ambient temperature
FVM	Finite Volume Method



$g_1$	Deflector gap
$h_1$	Tangential entry height
$h_2$	Octagonal cylinder height
$Ra$	Rayleigh number

## **Chapter 1: Introduction**

### **1.1 General introduction:**

Tornadoes occur in many parts of the world. In Canada they occur in southern Alberta, Manitoba, Saskatchewan, southern Ontario, southern Quebec, interior of British Columbia and western New Brunswick. The risk of tornadoes is the highest in southern Ontario and seven F4 tornadoes have been recorded in the region (Natural Resources Canada). It has also been assessed that on an average a F3 category tornado occurs in southwestern Ontario every five years (Newark 1984). Tornadoes generally last for an hour or more producing wind speeds exceeding 100 m/s close to the ground surface and generally leaving behind a trail of tremendous destruction a mile or more wide. Studying and understating these violent flows are necessary to reduce and prevent material and human losses.

A tornado is defined as a violently rotating column of air extending from a thunderstorm to the ground. Significant advances in understanding tornadoes were made in the 1970's with the pioneering work of T.T. Fujita. Prime means of measurement for deducing the vortex structure of tornadoes in nature are photogrammetry, local and aerial surveys of damage. A notable outcome from the aerial surveys has been the development of the Fujita scale (F-scale) for classifying a tornado according to its damage potential (Fujita, 1981). In recent years mobile Doppler radars have been used to capture the velocity fields of real tornadoes for studying its flow features (Zrnic et.al 1985, Wurman et.al 1996, Wurman 2002, Bluestein et. al 2004, Lee and Wurman 2005). The availability of a combination of physical observation techniques and mobile radar techniques has paved way for better understating of tornadoes.

There is a need to reproduce these uncontrollable vortices into more controllable laboratory-scale model vortices in order to gain a more comprehensive understanding of their flow dynamics. As it happens, the simulation of tornadoes in the laboratories started even prior to the studies on real scale tornadoes and a review of these laboratory models

are presented in detail by Davies-Jones (1976). Ward (1972) was the first to build a Tornado Vortex Chamber (TVC) with geometric and dynamic similarity to real scale tornadoes. The TVC was able to capture all the flow features observed in a real tornado including the evolution of multiple vortices starting from a single, primary tornado vortex (Ward 1972, Church et. al. 1979, Church and Snow 1979).

The observational studies in real tornadoes and laboratory simulated tornadoes have been complemented by fluid dynamic modeling studies. Numerical simulations provide a cost effective means to analyze the vortex flows. The objective of the simulations could be varied, some attempt to capture the parent super cell storm (Klemp and Wilhelmson, 1978, Wicker and Wilhelmson, 1995, Grasso and Cotton, 1995) and others like the tornado scale simulation models focus on the lower part of the tornado vortex with emphasis on the interaction between the tornado vortex and the ground surface (Rotunno 1977, 1979, 1984, Lewellen et.al 1997, Lewellen et.al 2000, Hangan and Kim 2008). The region close to the ground surface is of interest for engineering applications and is the topic of interest in the present thesis.

The progress made with experimental and computational modeling has been extensively and critically reviewed by Church and Snow (1993). A brief outline of some of the relevant works is included in the latter chapters of this thesis.

## **1.2 Scope and objective of the thesis:**

The objective of the thesis is to carry out numerical simulation for investigating the flow characteristics of tornado like vortices produced by different types of laboratory scale vortex generators. In particular, three types of generators are considered: Ward-type TVC, WinDEEE Dome and Atmospheric Vortex Engine (AVE). The objectives of each case are presented below.

Past numerical simulations of tornado-like vortices have been fairly successful in reproducing the laboratory scale and real scale tornadoes. The non-dimensional swirl

ratio has been recognized as the main fluid mechanics parameter for a tornado-like laboratory vortex (Lewellen 1962 and Davies-Jones 1973). The swirl ratios ranging from 0.1 to 2.0 are considered to be relevant for simulating the entire range of phenomena associated with different stages of evolution of the vortex. Past simulations have been limited to some select ranges of swirl ratios. Also, the observable parameters considered have not been consistent. Therefore, there is a need to generate consistent data over the exhaustive range of swirl ratios. Such data could serve as a database for both modelers and experimenters.

While the laboratory scale vortex simulations are characterized by the swirl ratio, the real scale tornado vortices are characterized by the Fujita scale. For purposes of comparison of the laboratory scale measurements with the real scale ones, correlation between the swirl ratio and Fujita scale need to be established. One such exploratory relation was proposed by Hangan and Kim (2008), in which F4 scale is found to correspond with the swirl ratio of 2. The availability of benchmarked data over a comprehensive range would be helpful while seeking further relations of this kind.

A numerical simulation of vortex in Ward-type TVC has been carried out with the objective of generating such benchmarked data. The simulations have been carried out using Fluent 6.3 code. Initial simulation was done for a swirl ratio of 0.28 for which good experimental data are available. The favorable comparison between the model results and the experiment indicated the validity of the modeling. Subsequently, computations were extended for other values of swirl ratios. Considering the inability of Reynolds Stress Model (RSM) to capture the formation of multiple vortices in the case of large swirl ratios, Large Eddy Simulation (LES) scheme was employed.

The dataset generated is later used in the thesis to study how the flow pattern in vortex close to the ground surface is affected by surface roughness and translation. An important objective of the study is to examine how the effects of surface roughness and translation vary as a function of the swirl ratio. Consistent data for a set of swirl ratios

representing different stages of evolution of the vortex flow are generated. These computations employ LES model. The above topics form the subject of Chapters 2 and 3.

The Wind Engineering, Energy and Environment (WinDEEE) Dome is a novel, multipurpose wind research facility proposed and conceptually designed by Dr. Horia Hangan, which is being built at the University of Western Ontario, funded by the Canadian Foundation for Innovation (CFI) and the Ontario Research Fund (ORF). It can produce tornado-like, downburst-like and synoptic wind profile in a single chamber by modifying the inlet and outlet boundary conditions. When constructed and commissioned, the dome would allow wind testing of large scale models of buildings and structures in complex terrain under sheared/straight and axi-symmetric flows. The purpose of the numerical simulation is to identify the optimum inlet and outlet configurations for generating each of the wind profiles, and assess the design adequacy of the dome for the intended applications. The desirable flow characteristics to meet the targeted applications are identified and are used as acceptance criteria to decide the adequacy of the design. The simulated results are compared with available real scale and laboratory scale tornadoes and downbursts. The simulation work and results for WinDEEE dome are described in Chapter 4.

The atmospheric vortex engine (AVE) uses an artificially created vortex to capture the mechanical energy produced during upward heat convection. The heat source can be solar energy, warm seawater or waste industrial heat. The mechanical energy is produced in peripheral turbo-generators. The AVE has the same thermodynamic basis as a solar chimney (Schlaich et.al, 2005, Haff et.al, 1983 and Haaf, 1984). The latter have been studied and their energy conversion efficiency has been shown to be a function of the height of the chimney. Louis Michaud proposed a possible way of eliminating the impractically tall chimneys by exploiting a characteristic of tornado like vortices (Michaud 1977, 1995, 1996, 1999). The centrifugal force of the vortex arrests the mixing of air, thus acting as a virtual wall obviating the need for a tall chimney. Numerical simulation of a preliminary design of the AVE was done to study the effectiveness of AVE in generating tornado-like vortices. The effects due to changing geometrical and

physical parameters were considered with a view to facilitate future design optimization. The influence of cross wind flow is also examined. The results of simulation for AVE are presented in Chapter 5.

### **1.3 Thesis format:**

This thesis is written in the 'Integrated Article Thesis' format specified by the Faculty of Graduate Studies of the University of Western Ontario. Each chapter except the first and last chapters is presented as a technical paper without an abstract but with its own references. Tables and Figures for each chapter are presented at the end of each chapter. The symbols and abbreviations for each chapter are listed in the prefatory pages.

### **1.4 Reference:**

Bluestein, H. B., Weiss, C. C. and Pazmany, A. L., 2004. The vertical structure of a tornado near happy, Texas, on 5 May 2002: High-Resolution, Mobile, W-band, Doppler Radar Observations. *Monthly Weather Review* 132, 2325-2333.

Church, C.R., Snow, J. T., Baker, G. L., Agee, E. M., 1979. Characteristics of tornado like vortices as a function of swirl ratio: A laboratory investigation, *Journal of the Atmospheric Sciences* 36, 1755-1776.

Church, C. R., and Snow, J. T., 1979. The dynamics of natural tornadoes as inferred from laboratory simulations. *Journal de Recherches Atmospheriques* 13, 111-133.

Church, C. R., and Snow, J. T., 1993. Laboratory models of tornadoes, *The Tornado: Its Structure, Dynamics, Prediction, and Hazards*, Geophysical Monograph 79, Church et al., Eds., American Geophysical Union, 277-295.

Davies-Jones, R. P., 1973. The dependence of core radius on swirl ratio in a tornado simulator. *Journal of the Atmospheric Sciences* 30, 1427-1430.

Davies-Jones, R.P., 1976. Laboratory simulations of tornadoes. Proc. Symp. On Tornadoes, Lubbock, TX, Texas Tech University, 151–174.

Fujita, T. T., 1981. Tornadoes and downbursts in the context of generalized planetary scales. *Journal of the Atmospheric Sciences* 38, 1511-1534.

Grasso, L. D., and Cotton, W. R., 1995. Numerical simulation of a tornado vortex, *Journal of the Atmospheric Sciences* 52(8), 1192–1203.

Haaf, W., 1984. Solar Chimneys - Part II: Preliminary Test Results from the Manzanares Pilot Plant. *International Journal of Solar Energy* 2(2), 141–161.

Haaf, W., Friedrich, K., Mayr, G., and Schlaich, J., 1983. Solar Chimneys. Part 1: Principle and Construction of the Pilot Plant in Manzanares. *International Journal of Solar Energy* 2(1), 3–20.

Hangan, H., and Kim, J., 2008. Swirl ratio effects on tornado vortices in relation to the Fujita scale. *Wind and Structures* 11(4), 291-302.

Klemp, J. B., and Wilhelmson, R. B., 1978, The simulation of three dimensional convective storm dynamics, *Journal of the Atmospheric Sciences* 35, 1070–1096.

Lee, W-C., Wurman, J., 2005. Diagnosed three-dimensional axisymmetric structure of the Mulhall tornado on 3 May 1999. *Journal of the Atmospheric Sciences*, 62, 2373-2394.

Lewellen, W. S., 1962. A solution for 3 dimensional vortex flows with strong circulation. *The Journal of Fluid Mechanics* 14, 420-432.

Lewellen, W. S., Lewellen, D. C., Sykes, R. I., 1997. Large-eddy simulation of a tornado's interaction with the surface. *Journal of the Atmospheric Sciences* 54, 581–605.

Lewellen, D. C., Lewellen, W. S., and Xia, J., 2000. The influence of a local swirl ratio on tornado intensification near the surface, *Journal of the Atmospheric Sciences* 57, 527–544.

Michaud, L. M., 1977. On the energy and control of atmospheric vortices. *Journal de Recherches Atmospheriques* 11(2), 99-120.

Michaud, L. M., 1995. Heat to work conversion during upward heat convection. Part I: Carnot engine method. *Atmospheric Research* 39, 157-178.

Michaud, L. M., 1996. Heat to work conversion during upward heat convection. Part II: Internally generated entropy method. *Atmospheric Research* 41, 93-108.

Michaud, L. M., 1999. Vortex process for capturing mechanical energy during upward heat-convection in the atmosphere. *Applied Energy* 62, 241-251.

Newark, M. J., 1984. Canadian tornadoes, 1950-1979. *Atmospheric-Ocean* 22, 243-253.

Rotunno, R., 1977. Numerical simulation of a laboratory vortex, *Journal of the Atmospheric Sciences* 34, 1942-1956, 1977.

Rotunno, R., 1979. A study in tornado like vortex dynamics, *Journal of the Atmospheric Sciences* 36, 140-155.

Rotunno, R., 1984. An investigation of a three dimensional asymmetric vortex, *Journal of the Atmospheric Sciences* 41, 283-298.



Schlaich, J., Bergermann, R., Schiel, W., and Weinrebe, G., 2005. Design of commercial solar tower systems—utilization of solar induced convective flows for power generation, *Journal of Solar Energy Engineering* 127, 117-124.

Ward, N. B., 1972. The exploration of certain features of tornado dynamics using a laboratory model. *Journal of the Atmospheric Sciences* 29, 1194-1204.

Wicker, L. J., and Wilhelmson, R. B., 1995. Simulation and analysis of tornado development and decay within a three dimensional supercell thunderstorm, *Journal of the Atmospheric Sciences* 52(15), 2675–2703.

Wurman, J., Straka, J., and Rasmussen, E., 1996. Fine scale Doppler radar observation of tornadoes. *Science*, 272, 1774-1777.

Wurman, J., 2002. The multiple-vortex structure of a tornado. *Weather and forecasting* 17, 473–505.

Zrnic, D., Burgess, D. W., and Hennington, L., 1985. Doppler spectra and estimated windspeed of a violent tornado. *Journal of Climate and Applied Meteorology* 24, 1068-1081.

## Chapter 2: Numerical Simulation of Laboratory Scale Tornado-like Flows

### 2.1 Introduction:

Tornadoes are violent vortex flows in nature, with wind speeds exceeding 100 m/s near the surface. Studying the flow dynamics of tornadoes necessitates the reproduction of these uncontrollable vortices into more controllable laboratory-scale model vortices. For a tornado-like laboratory vortex, Lewellen (1962) and Davies-Jones (1973) have shown that the main governing non-dimensional parameters are aspect ratio (A), Swirl ratio (S), Reynolds number and Froude number ( $Fr = (\Delta P / 2g\Delta\rho z)^{0.5}$ ;  $\Delta P$  = pressure drop,  $\Delta\rho$  = density change within the flow,  $g$  = acceleration due to gravity and  $z$  = height above the ground). The aspect ratio and swirl ratio are defined below.

$$A = H_0/R_0 \quad (2.1)$$

$$S = V_0/2AU_0 \quad (2.2)$$

Where  $R_0$  is the radius of the updraft and  $H_0$  is the depth of inflow in a tornado vortex chamber (see Figure 2.5b).  $U_0$  and  $V_0$  are the radial and axial velocities at  $R_0$ . Ward (1972), Rotunno (1977), and Church et. al. (1979) have identified the Swirl ratio as the dominant governing parameter and observed that the flow pattern in a laboratory scale vortices varies with swirl ratio as shown in Figure 2.1. With increasing swirl ratio the tornado vortex develops from a jet-like flow to a one-cell laminar vortex (Figure 2.1a), further increase in swirl ratio results in a stagnation point and vortex break down (VBD) aloft (Figure 2.1b). The VBD moves upstream touches the surface with increase in swirl ratio resulting in the formation of turbulent two-cell vortex (Figure 2.1c). At very high swirl ratio multiple vortices appear around the main vortex core (Figure 2.1d). Tornado sightings (Maxworthy 1973, Fujita 1981, Lugt 1989) and Doppler radar observations (Wurman et.al 1996, Wurman 2002, Bluestein et. al 2004, Lee and Wurman

2005) have confirmed the occurrence of these flow patterns in real scale tornadoes. Therefore laboratory scale models are effective tools to study tornado-like flows.

This chapter focuses on the numerical simulation of a tornado-like laboratory scale vortex. Numerical simulations, while introducing approximations, have the advantage of describing the overall structure of the flow. These numerical models are therefore a useful tool for investigation. The objective of the study is to simulate the tornado vortex for the full range of swirl ratios (0.1-2.0) which can be later used as a base case to study the changes in the flow pattern due to the effects of translation and surface roughness. Before describing the present work, a brief outline of the past laboratory and numerical models are presented below as background.

### **2.1.1 Laboratory models:**

Many experimental models for tornado generation are available. Davies-Jones (1976) presents a detailed review of these laboratory models and concludes that the Ward-type Tornado Vortex Chamber (TVC) (Ward, 1972) demonstrates both geometric and dynamic similarity to natural vortices. Figure 2.2 shows a sketch of the Ward-type TVC. It has two stacked cylindrical chambers separated by a partition having a circular hole for updrafts. The lower chamber side-wall has a rotating screen to provide angular momentum to inlet flow. The roof of the upper cylindrical chamber has flow straightening baffles and a suction fan above it. By controlling the volume flow through the suction fan and angular momentum through the rotating screen, a wide range of swirl ratios can be generated. The model produces tornadoes with one-cell, vortex break down, two-cell and multiple vortex configurations.

Experiments by Ward (1972), Davies-Jones (1973) showed that the core size is primarily a function of swirl ratio. Snow et.al (1980), Pauley et.al (1982), Church and Snow (1985) and Pauley (1989) present surface pressure profiles as a function swirl ratio for the Ward-type TVC. Snow and Lund (1988) improved the Ward-type TVC by replacing the rotating screen with adjustable vanes and adding non-intrusive velocity

measurement instrumentation like Laser Doppler Velocimeter (LDV). Preliminary LDV results are presented in Lund and Snow (1993).

Haan Jr et al. (2007) present a TVC (Iowa-TVC) with translation ability. The TVC is as shown in Figure 2.3. It consists of two concentric cylinders forming a duct with a fan in the center. The air circulates between base surface and the duct. The swirl component is added through vanes in the roof of the inner cylinder. The Iowa-TVC produces one-celled turbulent vortices but does not produce the multiple vortex flows. Hashemi-Tari (2007) presents a TVC similar to the Iowa-TVC without the translation feature and presents an exhaustive set of PIV measurements for a range of swirl ratios less than 1. These results are essentially the first complete set of PIV measurements in a TVC characterizing both the mean and the turbulent flow fields. These experiments are nevertheless limited by the size of the apparatus and by the range of possible swirl ratios (Hashemi-Tari et al. 2010).

### **2.1.2 Numerical models:**

Numerical models are cost effective ways of analyzing the vortex flows. The numerical models can be divided into two broad categories: thunderstorm scale simulation and tornado scale simulation (Nolan and Farrell, 1999). The thunderstorm scale simulations are essentially meteorological models that tend to reproduce the parent super-cell storm with sufficient resolution to resolve tornado vortices spawned during the simulation (Klemp and Wilhelmson, 1978, Wicker and Wilhelmson, 1995, Grasso and Cotton, 1995). Tornado-genesis (formation of tornado) can also be studied using these models. The tornado scale simulation models the lower part of the tornado vortex with emphasis on the interaction between the tornado vortex and the ground surface. These engineering models provide the flow structure and the wind fields of tornado-like vortices close to the surface, a region of interest for engineering applications. Further discussions in this chapter are limited to the tornado scale models.

Harlow and Stein (1974) developed the first numerical model to simulate tornado-like vortices in a Ward-type TVC. The two dimensional axisymmetric model produced the one-celled and two-celled vortices using a free-slip lower boundary condition. Rotunno (1977, 1979) was able to capture the VBD using a no-slip lower boundary condition. The simulations also showed the vortex core size to be a function of swirl ratio and nearly independent of Reynolds number thereby confirming the experimental results of Ward (1972), and Davies-Jones (1973). Rotunno (1984) simulated multiple vortices by introducing random noise to a three dimensional model of Ward-type TVC and observed secondary vortices with 20-30% more tangential velocity than the mean flow. Wilson and Rotunno (1986) simulated a low swirl ratio ( $S = 0.28$ ) laminar vortex and matched the experimental results of Baker (1981). Their work identified four principal regions in the low swirl ratio single-cell vortex flow as shown in Figure 2.4. The vortex was found to be mostly inviscid and rotational with a small viscous sub-layer whose depth decreased towards the central axis and a thin viscous region in the core along the central axis.

Fiedler (1994, 1995, 1997, and 1998) used an axisymmetric model to study vortices that form within a domain with rigid boundaries by introducing buoyancy in a rotating cylinder of fluid. The results showed that the vortex touch down produces wind speeds that exceed the thermodynamic speed limit by a factor of 5 and at higher swirl ratios produced multiple vortices with addition of random fluctuations. When the fluid is considered compressible, their simulations showed that even at subsonic flow, compressibility only slightly decreases the extremes in the wind speeds, as compared with a corresponding incompressible numerical simulation. Nolan and Farrell (1999) further modified the model and observed that a non-dimensional parameter Vortex-Reynolds number (Ratio of far field circulation to eddy viscosity) was more effective than the conventional swirl ratio in predicting the structure of a vortex.

Lewellen et.al (1997) and Lewellen et.al (2000) model real scale tornadic flow in a  $1\text{km} * 1\text{km} * 2\text{km}$  domain using LES simulations and analyze the flow dynamics close to the surface. The results showed the influence of turbulence in generating high wind speeds near the ground and production of multiple vortices at high swirl ratio. The time

averaged maximum velocity was observed to occur at very close proximity to the surface at less than 50 m from the ground. Xia et.al (2003) extended the simulation to include compressibility and observed similar to Fiedler (1997) that compressibility effects are unlikely to change the basic dynamics of vortex flows near the surface.

Hangan and Kim (2008) used Reynolds Stress Model (RSM) for Ward-type laboratory scale tornado to match the Doppler radar data for real scale tornado and thereby tentatively related the swirl ratio with the Fujita scale. Their work inferred that F4 Fujita scale tornado approximately corresponds to a swirl ratio of  $S = 2.0$ . Also recently Kuai et.al (2008) have simulated the Iowa-type TVC using the RNG k- $\epsilon$  model and compared the results with real scale tornado.

Numerical simulations of tornado-like vortices have been successful in producing both laboratory-scale and full-scale flow patterns. However, there was no consistent attempt to simulate these vortices over an exhaustive range of swirl ratios. As the work of Hangan and Kim (2008) pointed out, there is an exploratory relation between the fluid mechanics parameter swirl ratio ( $S = 2.0$ ) and the forensic Fujita scale parameter (F4). To extend this kind of relation to other Fujita scales, there is a need for benchmarked laboratory scale data for a wide range of swirl ratios. Herein we attempt to generate such data using numerical simulations.

For the current simulations, a Ward-type TVC model was chosen, as it is known to produce all the observed flow patterns across the full range of swirl ratios ( $S = 0.1-2.0$ ) including the complex multiple vortices at high swirl ratio. In section 2.2 the Reynolds Stress Model (RSM) simulations are presented and the mean velocity, pressure profiles and vortex core sizes are compared with past observations. The RSM model fails to generate multiple vortices at high swirl ratios; so Large Eddy Simulations (LES) were performed. These simulations captured the multiple vortices and are presented in section 2.3 along with the turbulence characteristics for selected swirl ratios ( $S = 0.28, 0.5, 1.0, 2.0$ ).

## 2.2 RSM simulations:

### 2.2.1 Numerical Setup:

The Computational Fluid Dynamics software, Fluent 6.3 was used for the current three-dimensional numerical simulation of laboratory scale tornado-like vortices. Unsteady Reynolds Averaged Navier-Stokes (RANS) equations were solved on structured grids and a quasi-steady state solution was reached. The simulations were performed for swirl ratios  $S = 0.1, 0.2, 0.28, 0.4, 0.5, 0.6, 0.7, 0.8, 0.9, 1.0, 1.5$ , and  $2.0$ . An initial grid with boundary layer at the base and Hex/Wedge mesh elements with around 150,000 cells was developed using the commercial software 'Gambit'. Subsequent grid adaptations were performed using the 'Velocity-Gradient-adaptation', 'Region-adaptation' and 'Wall-Y+-adaptation' features in Fluent (Fluent 2006). Since the study was focused on the surface-layer wind profiles, the grid adaptations were also focused near the base surface. Following grid convergence criterion of less than 2% variation in maximum velocity near the base, a maximum of around 1,000,000 cells were used in the simulations. Based on the previous results obtained by Hangan and Kim (2008) the Reynolds Stress Model (RSM) was used for modeling turbulence. The basic equations defining this model are presented in Appendix A. The segregated implicit solver, SIMPLEC pressure velocity coupling and second order discretization for pressure, momentum, turbulent kinetic energy and specific dissipation rate were used.

Figure 2.5a shows the schematic diagram of the Purdue TVC (Church et al., 1977) which was used as a basis for the present simulation. The TVC is a modification of the Ward type TVC (Ward 1972). As mentioned in section 2.1.2 the flow volume is controlled by the suction fan above the flow straightening baffles and angular momentum is added at the air inlet using a rotating screen. The air enters the confluence region through the rotating screen and has weakly coupled radial and tangential velocity. Axial velocity is negligible. This region models the sub-cloud region surrounding a tornado and the upper wall (at height  $H$  from base) in the region is an analogy to the layer of stable air in the environment, which restricts the inflow to a low level in a tornado. The flow

converges in the convergence region and has significant tangential and axial velocity and the region contains the vortex. This region models the sub-cloud region containing a tornado. The air exits the system through the convection region and the increase in diameter of the region acts as a distributed sink (Church et al., 1977).

In the current simulation, the blue shaded region of the Purdue TVC shown in Figure 2.5a is modeled. This region includes the convergence region which contains the tornado vortex close to the center. The details of the domain geometry are shown in Figure 2.5b. Table 2.1a lists the types of boundary conditions and Table 2.1b lists the domain dimensions used in the simulations. The selected radius of the domain  $R_0 = 0.4$  m represents the typical size of experimental geometries. This value is adequate considering the fact that tornado forms close to the centerline. Moreover, simulations with a larger radius of  $R_0 = 0.6$  m have not led to any noticeable differences in the flow profile.

The inlet surface has a velocity-inlet boundary condition, wherein the radial and tangential velocities on the inlet surface are specified using a User Defined Function (UDF) and the axial velocity is assumed to be zero. The boundary layer type velocity profiles used in the UDF are given below.

$$U_{R_0}(z) = U_1 * (z/z_1)^{1/7} \quad (2.3)$$

$$V_{R_0}(z) = (2H_0/R_0) * S * U_{R_0}(z) \quad (2.4)$$

Where  $U_{R_0}$  and  $V_{R_0}$  are the radial and tangential velocity at inlet,  $S$  is the swirl ratio,  $U_1$  is the reference velocity and  $z_1$  is the reference height. By matching the velocity profile at the inlet with the experimental results of Baker (1981) the values of  $U_1$  and  $z_1$  are set to 0.3 m/s and 0.025 m respectively. The Baker (1981) results do not state the turbulence characteristics at the inlet. In the current simulations turbulence is specified at the inlet with turbulence intensity  $TI = 1\%$  and turbulence viscosity ratio  $TVR = 10$ . For a converged solution the turbulence specified at the inlet does not affect the flow pattern (Fluent 6.3, 2006), nevertheless simulations with different turbulence at the inlet like  $TI =$



1% and  $TVR = 1$  were performed and it was observed that they did not produce any significant change in the results.

At the base, wall boundary condition with the ‘Enhanced wall treatment’ option in Fluent is used. In this near-wall modeling technique the viscous sub-layer is also resolved and requires very fine meshing near the wall. It requires the value of  $z^+$  ( $z^+ = u^* z / \nu$  where  $u^*$  is the friction velocity,  $z$  is the distance to the wall and  $\nu$  is the kinematic viscosity of air) at the wall-adjacent cell to be of the order of 1 (Fluent 2006). In this study the  $z^+$  values were below 1.5.

Numerical analysis of Smith (1987) show that the choice of side wall boundary condition in the convection region does not affect the vortex development in the convergence region (flow measurements are made in this region) even for large values of swirl ratio where the vortex core approaches this boundary in the convection region. Therefore, a free-slip wall boundary condition was chosen for the side wall. In the experimental setup the outlet has a flow-straightening baffle and its function is to prevent the contamination of the vortex by the swirling flow from the exhaust fan which is used to drive the flow (see Figure 2.2 for the experimental setup). The numerical simulation does not model the exhaust fan and is driven by the inlet velocities specified at the inlet surface, so a boundary condition representative of the ‘flow-straightening baffle’ need not be specified at the outlet surface. At the same time, an outflow boundary condition at the outlet surface is more representative of the actual atmospheric phenomena as argued by Smith (1987). Therefore, at the outlet surface an outflow boundary condition was used in the current simulation which assumes a zero normal gradient for all flow variables except pressure. (Fluent 2006)

### **2.2.2 Benchmarking:**

The results from the present simulations are compared with the experimental results of Baker (1981) for  $S = 0.28$ . The experiments were conducted in a Ward-type TVC similar to the one shown in Figure 2.5a and the velocity profiles were measured using hot-wire

anemometry. Figures 2.6, 2.7 and 2.8 compare respectively the radial, tangential and axial mean velocity profiles of the experiment with those of the numerical simulation for radial locations  $R/R_0 = 0.1025$  and  $R/R_0 = 0.2125$ , where measurements are available. The velocities are normalized with the average radial velocity  $U_0$  at inlet and the height is normalized using  $R_0$ . Considering the facts that the inlet boundary conditions are not identical and the Baker experiment used intrusive hot-wire anemometry the numerical simulations compare reasonably well with the experimental results. These comparisons show that the domain geometry and the boundary conditions considered in the simulation are able to reproduce the main flow in the TVC for  $S = 0.28$ . Therefore, simulations for other swirl ratios were performed using the same domain geometry along with suitable modification of the inlet boundary condition.

### 2.2.3 Mean flow field:

It is known that the flows with no swirl i.e.  $S = 0$ , are similar to a flow in a corner as shown in Figure 2.9. The decelerating radial inflow causes a negative pressure gradient and flow separation occurs with a stagnation region near the centerline (Church et al 1979). When the swirl ratio is increased ( $S < 0.1$ ), initially the separated flow region prevents low level angular momentum approaching the region close to the centre line. As a result a core develops aloft and builds downward and around  $S = 0.1$ , the swirl induced positive pressure gradient overcomes the above described negative pressure gradient and a concentrated core makes contact with the surface and the inflow boundary layer reattaches to the surface (Church et al 1979). Since flows with  $S < 0.1$  are of little interest in the context of the present studies, simulations were done for  $S = 0.1$  onwards. The evolution of the vortex profile as the swirl ratio  $S$  increases from 0.1 to 2.0 is described in this section in terms of the mean velocity profiles.

One-celled vortex ( $S = 0.1-0.4$ ):

At low swirl ratios like 0.1-0.2, a flow with a thin jet like laminar vortex is observed as shown in the contour plot of velocity for  $S = 0.2$  (Figure 2.10a). For further increase in swirl ratio the laminar vortex transitions to a turbulent vortex downstream. The region

where the transition occurs is called the vortex break down (VBD) and around the VBD the vortex expands and forms a bulb like structure as shown in Figure 2.8b for  $S = 0.28$ . The VBD moves upstream closer to the surface at  $S = 0.4$ . The VBD is considered to be an axisymmetric analog to the hydraulic jump phenomenon observed in channel flows (Benjamin 1962) and other theories consider it to be a type of flow separation phenomenon (Hall 1967, 1972).

Figure 2.11a shows the radial profile of the azimuthally averaged mean velocity components namely axial, radial and tangential velocities at the height  $Z_{\max}$  (height of maximum tangential velocity) for  $S = 0.28$ . Figure 2.11b shows the velocity components as a function of height at radial locations both inside ( $R < R_{\max}$ ) and outside ( $R > R_{\max}$ ) the core of the vortex. (Core radius  $R_{\max}$  is the radius at which the maximum tangential velocity occurs) In both the plots the velocities are normalized with  $U_0$  and distance is normalized with  $R_0$ . From these plots it can be observed that the axial velocity increases along the radial inward direction and reaches a maximum at the centerline. Also the axial velocity is in the upward direction both inside and outside the core. The tangential velocity along the radial direction varies as in a Rankine vortex. Along the height the tangential velocity gradually increases from zero at the base to a maximum value at  $Z/R_0 = 0.08$  for  $R < R_{\max}$  and  $Z/R_0 = 0.05$  for  $R > R_{\max}$  and reaches a constant value at further heights. The radial velocity along the height shows that the convergence is limited to low levels ( $Z/R_0 = 0-0.1$ ). Near the ground a nose like profile is observed with peak velocities around  $Z/R_0 = 0.02$ .

The vortex flows in this range of swirl ratios have been known and are seen here as well to exhibit one-celled structure. These vortex flows are called end wall vortex because axial velocity is in the upward direction both inside and outside the core and maximum axial velocity occurs within the core.

Vortex-touch-down ( $S = 0.5$ ):

For swirl ratio 0.5, VBD touches the base surface. This stage is called the vortex touch down (VTD) and Figure 2.10c shows the contour of velocity at VTD at  $S = 0.5$ .

Figures 2.12a and 2.12b are similar to the Figures 2.11a and 2.11b and are plotted for swirl ratio  $S = 0.5$ . It can be observed from Figure 2.12a that unlike the low swirl case (Figure 2.10a) the tangential velocity is greater than the axial velocity at  $R_{\max}$ . The tangential velocity along the radial direction follows the same Rankine vortex profile. The radial velocity profile along the height is similar to the low swirl case outside the core, but inside the core the height of convergent flow is reduced to  $Z/R_0 = 0.04$ . The axial velocity is in the upward direction along the height outside the core and inside the core it is initially upward (till  $Z/R_0 = 0.04$ ) and then becomes downward as the height increases. The axial velocity along the centerline in the flow is observed to be downward all along the height (a feature not shown in Figure 2.12b).

Past simulations have observed that the maximum tangential velocity in a laminar end-wall vortex ( $S < 0.4$ ) exceeds the maximum tangential velocity associated with ‘thermodynamic speed limit’ (Fiedler and Rotunno 1986, Fiedler 1994, Nolan and Farrell 1999). Fiedler (1994) observed that the maximum tangential velocity at VBD is greater than the laminar end wall vortex and is five times the thermodynamic speed limit. This trend is observed in the current simulation too; at  $S = 0.5$  the maximum tangential velocity is six times the maximum tangential velocity calculated using the artificial Convective Available Potential Energy (CAPE) equation (Eq.10, Fiedler and Rotunno 1986).

Two-celled vortex ( $S = 0.6\text{--}0.9$ ):

At these swirl ratios the VBD penetrates the base and the vortex develops into a two celled vortex. The vortex has a core with axial velocity in the downward direction and an outer region with axial velocity in the upward direction. Figure 2.10d shows a two celled vortex for  $S = 0.8$ .

Figures 13a and 13b are again similar to the Figures 2.11a and 2.11b and are plotted for swirl ratio  $S = 0.8$ . The velocity profiles along the radial direction (Figure 2.13a) are similar to the case of swirl ratio  $S=0.5$  outside the core but differ significantly inside the core. This can be seen better in Figure 2.13b. The tangential velocity is very less inside the core compared to outside the core and remains constant along the height. The radial velocity is negligible inside the core and the nose like profile observed in the low swirl cases is absent. Outside the core the profile of the radial velocity still retains the nose shaped profile but convergence is limited to  $Z/R_0 = 0.7$  and for further increase in height the radial velocity diverges till  $Z/R_0 = 1.7$  before reaching a constant value. The axial velocity is in the downward direction all along the height inside the core and in the upward direction outside the core, in accordance with the nature of the two-celled vortex flow.

Multiple vortices ( $S = 1.0-2.0$ ):

At such high swirl ratios, one expects the core to expand and the upward flow to be concentrated in the narrow annulus region around the core. The instabilities of the cylindrical shear layer associated with the radial variation of tangential velocity would then lead to the formation of multiple vortices around the core vortex (Ward 1972, Snow 1978 and Rotunno 1983). Laboratory experiments (Church et al. 1979) have also confirmed the formation of multiple vortices. However, the current simulation based on RSM is unable to capture these multiple vortices. While Figures 2.10e and 2.10f display the flow profile for  $S = 1.0$  and  $S = 2.0$ , Figures 2.14a and 2.14b show velocity components for swirl ratio  $S = 2.0$  in the same fashion as Figures 2.11a and 2.11b. Since the multiple vortices are not captured the profiles are similar to the two-celled profile of  $S = 0.8$ .

#### **2.2.4 Pressure deficit:**

For flow with swirl ratio  $S = 0$ , the deceleration of the radial velocity establishes a high pressure region at the centerline. As the swirl is added to the flow, the conservation of angular momentum induces a low pressure at the centerline countering the high pressure.

As the swirl ratio increases the pressure profiles are further influenced by the VBD, formation of double-cell and multiple vortices (Snow et.al 1980, Pauley et.al 1982). Pressure deficit with respect to ambient pressure is another convenient measurable parameter while describing the vortex structure. This section describes the changes in the pressure deficit profiles with increase in swirl ratio. In this context, we define the static pressure coefficient  $C_p$  as

$$C_p = \frac{P - P_0}{0.5\rho U_0^2} \quad (2.5)$$

Where  $P_0$  and  $U_0$  are the static pressure and average radial velocity at  $R_0$ , and  $\rho$  is the density of air.

Figure 2.15 presents the static pressure coefficient ( $C_p$ ) along the radial distance at the base for different swirl ratios and Figure 2.16 shows the variation of maximum base pressure deficit for a range of swirl ratios ( $S = 0.1-2.0$ ). Figure 2.17 shows the variation of the pressure coefficient ( $C_p$ ) along the height at the centerline.

Low swirl ratios:

In the results presented earlier, it has been seen that a single cell-vortex occurs for swirl ratios 0.1-0.4, a VTD occurs around  $S = 0.5$  and the single-cell vortex begins to evolve into a double-cell vortex at  $S = 0.6$ . In this range of swirl ratios the base pressure deficit increases with increase in swirl ratio i.e. increase in tangential velocity and reaches a maximum around VTD (Figures 2.15a and 2.16). The radial pressure gradient at the base also increases with swirl ratio and maximum base pressure deficit is in a narrow region around the center ( $R/R_0 = 0$ ). It is observed from Figure 2.17 that the VBD influences the pressure deficit profile along the height. For  $S = 0.1$  with no VBD, the pressure deficit gradually increases from close to zero at the surface to a maximum along the height and remains constant thereafter. At  $S = 0.28$  the pressure deficit increases along the height and reaches a maximum at  $Z/R_0 = 0.08$  where VBD appears in the flow and reduces

further along the height. The VBD touches the surface around  $S \sim 0.5$  and here the maximum pressure deficit is very close to the surface and reduces along the height.

High swirl ratios:

Recall that for swirl ratio  $S = 0.7-0.9$ , the VBD has fully penetrated the surface and a double cell vortex with the re-circulating flow in the core region was observed. In this range of swirl ratios the surface pressure deficit decreases with increase in swirl ratio and the profile of the pressure deficit flattens in the core region (Figures 2.15b and 2.16). The variation of the pressure deficit profile along the height, shown in Figure 2.17 for  $S = 0.8$ , indicates the pressure deficit to be maximum along the ground and having a decreasing trend with height.

For swirl ratio in the range  $S = 1.0-2.0$ , multiple vortices expected to occur around the main vortex was not captured in the present simulation. In this range of swirl ratios the surface pressure deficit again increases with the increase in swirl ratio (Figures 2.15b and 2.16) and the variation along the height is similar to the  $S0.7-S0.9$  range of swirl ratios as shown in Figure 2.17 for  $S = 1.0$ .

The pressure deficit profiles presented here are similar to the experimental results of Snow et.al (1980), Pauley et.al (1982), Church and Snow (1985) and Pauley (1989). The base pressure deficit is also qualitatively similar to the surface pressure deficit (low resolution micro-barograph traces) of a real tornado presented in Ward (1972).

### **2.2.5 Core radius:**

Core radius ( $R_{\max}$ ) defined as the radius at which the maximum tangential velocity ( $V_{\max}$ ) occurs is a salient characteristic of a tornado, and the height at which  $V_{\max}$  occurs is denoted by  $Z_{\max}$ . Experimental results of Davies-Jones (1973) and numerical simulations of Rotunno (1977) establish that the core radius is mainly a function of swirl ratio and is nearly independent of Reynolds number. Figure 2.18 shows the plot of normalized core radius ( $R_{\max}/R_0$ ) as a function of swirl ratio ( $S = 0.1-2.0$ ) and it can be seen that the core

radius generally increases with increase in swirl ratio. This is in agreement with the experimental results of Ward (1972), Davies-Jones (1973), Hashemi-Tari et al. (2010) and numerical results of Rotunno (1977). Figure 2.18 also shows  $Z_{\max}/R_0$  as a function of swirl ratios (S0.2-S2.0), the  $Z_{\max}/R_0$  for  $S = 0.1$  is not shown in the plot as it occurs higher than the plot limits (S0.1:  $Z_{\max}/R_0 = 0.09$ ). The  $Z_{\max}$  initially decreases with increase in swirl ratio ( $S = 0.1$ -0.5) and remains constant after  $S = 0.5$ . At low swirl ratio  $S = 0.1$ , the vortex is stronger aloft, so the  $Z_{\max}$  is high. As the swirl ratio increases from 0.2-0.4, VBD occurs aloft and moves upstream towards the base, the maximum tangential velocity occurs at the annular region that surrounds the VBD therefore  $Z_{\max}$  decreases. Around  $S \sim 0.5$  the VBD touches the base and the  $Z_{\max}$  remains constant for further increase in swirl ratio. The occurrence of maximum tangential velocity very close to the surface is in agreement with the results of Lewellen et.al (1997).

In real tornadoes the core is made visible by the presence of condensed water vapor, dust and debris. In a laboratory simulation the core can be made visible by introducing dry-ice or saw dust. In numerical simulations, an alternate definition of the core is used namely the locus of radial points along the height at which the maximum tangential velocity occurs at each height. Even though Jischke and Parang (1978) have shown that the core based on maximum tangential velocity differs from the observed visible core of a real tornado, it still can be used to visualize the changes in profiles of the tornado-like cores. Figure 2.19 shows the tangential velocity contours for swirl ratios  $S = 0.2, 0.5, 0.8, 1.0, 2.0$  and the maximum tangential velocity contour represents the core. It can be seen that shape of the core varies with height for each swirl ratio. For low swirl ratio  $S = 0.2$ , a thin narrow core is observed, the core increases in diameter and bulges near the base when VBD touches the surface at  $S = 0.5$ . This is similar to the observations made by Hashemi-Tari et al. (2010). For higher swirl ratios with two cell structure like  $S = 0.8$ , the core takes a conical shape near the surface and changes to an expanding cylindrical shape with increasing height. The vortex cores observed for  $S = 1.0, 2.0$  mainly resemble the  $S = 0.8$  case with increased diameter, as the multiple vortices generally expected in this range of swirl ratios is not captured in the current simulation.



The current core profiles (except for  $S = 1.0$  and  $S = 2.0$ ) match well with the experimental visualization results of Ward (1972), Church et.al (1979) and the observation of real tornadoes by Kuehnast and Haines (1971) and Lugt (1989).

## **2.3 LES simulations:**

### **2.3.1 Numerical setup:**

The computational software Fluent 6.3 was again used for the simulations. The domain and boundary condition are same as for the RSM simulation. Large Eddy Simulation (LES) was used for modeling turbulence with Dynamic Smagorinsky-Lilly subgrid model. The brief presentation of this model is provided in Appendix B. The segregated implicit solver, SIMPLEC pressure velocity coupling and bounded central difference discretization scheme for momentum equations were used. A time step of  $\Delta t = 0.0001$  was used. Grid convergence tests (2-3% variation in the maximum velocity near the base) were performed and a maximum of around 1,750,000 cells were used in the simulation

Considering the fact that LES simulations are computationally expensive, the simulations were not performed for the entire range of swirl ratios. Instead LES was performed for four important swirl ratios  $S = 0.28, 0.5, 1.0, 2.0$ . These swirl ratios were chosen because at  $S = 0.28$  the VBD starts to appear, at  $S = 0.5$  the VTD occurs and for  $S = 1.0, 2.0$  multiple vortices are expected.

### **2.3.2 Multiple vortices:**

The LES simulation produces multiple vortices at swirl ratios  $S = 1.0$  and  $S = 2.0$ . Figures 2.20 and 2.21 show the time averaged velocity magnitude, instantaneous velocity magnitude, instantaneous tangential velocity at height  $Z/R_0 = 0.02$  from the base for swirl ratios  $S = 1.0$  and  $S = 2.0$  respectively. For both the swirl ratios the instantaneous velocity contours show secondary vortices rotating about the main vortex. The instantaneous velocity at these secondary vortices exceeds the time averaged maximum velocities by

around 36 percent. The results are in sound agreement with the tornado-scale simulations of Lewellen et.al (1997) which produced secondary vortices having instantaneous velocities one-third more than the maximum time average velocities.

### 2.3.3 Turbulence characteristics:

Figures 2.22 and 2.23 show the root mean square (r.m.s) of the fluctuating axial ( $W_{rms}$ ), radial ( $U_{rms}$ ) and tangential ( $V_{rms}$ ) velocity and the Reynolds stresses  $\langle u'v' \rangle$ ,  $\langle u'w' \rangle$  and  $\langle v'w' \rangle$  along the height for swirl ratios 0.28 and 0.5 respectively. The profiles are plotted at radial locations inside the core ( $R < R_{max}$ ) and outside the core ( $R > R_{max}$ ). The r.m.s velocities are normalized with time averaged maximum tangential velocity ( $V_{max}$ ) and the Reynolds stresses are normalized with square of the  $V_{max}$  at each swirl ratio.

For  $S = 0.28$ , around  $Z/R_0 = 0.1$  there is a sudden increase in r.m.s velocities and Reynolds stresses inside the core. This is due to the presence of VBD around this height (Note that in Figure 2.17 for  $S = 0.28$ , the highest pressure deficit occurs around  $Z/R_0 = 0.1$  indicating the presence of VBD). Outside the core the r.m.s velocity and Reynolds stresses are negligible along the height. As the swirl ratio increases to  $S = 0.5$ , the height at which the maximum r.m.s velocities and Reynolds stresses occur moves closer to the ground around  $Z/R_0 < 0.04$  inside the core indicating downward movement of VBD.

Figures 2.24 and 2.25 plot the contours of r.m.s velocities and Reynolds stress  $\langle u'v' \rangle$  for  $S = 1.0$  and  $S = 2.0$  respectively and are normalized the same way as in Figures 2.22 and 2.23. As shown in section 2.3.2, multiple vortices exist at swirl ratios  $S = 1.0, 2.0$  and the vortex is not axisymmetric so the profiles are plotted as contours at height  $Z/R_0 = 0.02$  (Figures 2.24c, 2.24d, 2.25c and 2.25d) and in the XZ plane (Figures 2.24a, 2.24b, 2.25a and 2.25b). Unlike the low swirl ratio flows ( $S = 0.28, 0.5$ ) the r.m.s velocities and Reynolds stresses are negligible inside the core. The maximum occurs in an annular region around the core close to where the multiple vortices occur.

\

## 2.4 Conclusions:

Numerical simulations of laboratory scale tornado-like vortices were performed using RSM and LES turbulence models. For swirl ratios  $S < 1.0$ , the RSM model captures all flow features but for  $S \geq 1$  the flow is expected to produce transient multiple vortices but are not captured in the RSM model as it reaches a quasi steady state. So LES simulations were performed and multiple vortices were observed at high swirl ratios. Unlike the past laboratory scale simulations the multiple vortices were observed without adding any external random noise. The observed flow features are in agreement with the past experimental and numerical simulations.

As the swirl ratio increases the expected profiles like one-celled vortex, VBD, two-celled vortex and multiple vortices are observed in the simulated vortex. The tangential velocity increases with increase in swirl ratios. A peak in the mean tangential velocity is observed at both  $S = 0.5$  (VBD touches the surface around this swirl ratio) and  $S = 2.0$ . The peaks occur very close to the surface ( $Z/R_0 \leq 0.04$ ). Also at  $S = 2.0$ , multiple vortices with transient velocities 36% greater than the mean velocities are observed. So the tornado is most destructive during the vortex touch down and multiple vortex stage.

The core radius increases with increase in swirl ratio. The maximum surface pressure deficit occurs during the one-celled vortex configuration around  $S = 0.5$  and at  $S = 2.0$ .

The turbulent flow characteristics show that for low swirl ratios the r.m.s velocities and shear stresses are concentrated within the core near the VBD and follows the VBD as it moves closer to the base surface as the swirl ratio increases. For higher swirl ratios the stresses are concentrated in an annular region around the core. For all swirl ratios the peak r.m.s velocities and shear stresses occur at heights and radial distances close to the height and radius at which the maximum tangential velocity occurs. Since the observed maximum tangential velocities are greater than the theoretic

thermodynamic speed limit, it is very likely that close to the surface the velocities are influenced by the turbulent interaction of the vortex with the surface.

## **2.5 Reference:**

Baker, D. E., 1981. Boundary layers in laminar vortex flows. Ph.D. thesis, Purdue University.

Benjamin, T. B. 1962. Theory of vortex breakdown phenomenon. *Journal of Fluid Mechanics* 14, 593-629.

Bluestein, H. B., Weiss, C. C. and Pazmany, A. L., 2004. The vertical structure of a tornado near happy, Texas, on 5 May 2002: High-Resolution, Mobile, W-band, Doppler Radar Observations. *Monthly Weather Review* 132, 2325-2333.

Church, C.R., Snow, J. T., Baker, G. L., Agee, E. M., 1979. Characteristics of tornado like vortices as a function of swirl ratio: A laboratory investigation. *Journal of the Atmospheric Sciences* 36, 1755-1776.

Church, C. R. and Snow, J. T., 1985. Measurements of Axial Pressures in Tornado-like Vortices. *Journal of the Atmospheric Science* 42, 576–582.

Davies-Jones, R. P., 1973. The dependence of core radius on swirl ratio in a tornado simulator. *Journal of the Atmospheric Sciences* 30, 1427-1430.

Davies-Jones, R.P., 1976. Laboratory simulations of tornadoes. *Proc. Symp. On Tornadoes*, Lubbock, TX, Texas Tech University, 151–174.

Fiedler, B. H., 1994. The thermodynamic speed limit and its violation in axisymmetric numerical simulations of tornado-like vortices. *Atmosphere-Ocean* 32, 335–359.

- Fiedler, B. H., 1995. On modelling tornadoes in isolation from the parent storm. *Atmosphere-Ocean* 33, 501–512.
- Fiedler, B. H., 1997. Compressibility and windspeed limits in tornadoes. *Atmosphere-Ocean* 35, 93-107.
- Fiedler, B. H., 1998. Wind-speed limits in numerically simulated tornadoes with suction vortices. *Quarterly Journal of the Royal Meteorological Society* 124, 2377-2392.
- Fiedler, B. H., and Rotunno, R., 1986. A theory for the maximum wind speeds in tornado-like vortices. *Journal of the Atmospheric Sciences* 43, 2328–2340.
- FLUENT 6.3 User's guide, 2006. Fluent Inc, Lebanon, USA.
- Fujita, T. T., 1981. Tornadoes and downbursts in the context of generalized planetary scales. *Journal of the Atmospheric Sciences* 38, 1511-1534.
- Grasso, L. D., and Cotton, W. R., 1995. Numerical simulation of a tornado vortex. *Journal of the Atmospheric Sciences* 52(8), 1192–1203.
- Haan Jr, F.L., Sarkar, P.P., Gallus, W.A., 2007. Design, construction and performance of a large tornado simulator for wind engineering applications. *Engineering Structures*, doi:10.1016/j.engstruct.2007.07.010
- Hall, M. G., 1967. A new approach to vortex breakdown. *Proc. 1967 Heat Transfer and Fluid Mechanics Institute, Stanford University Press*, 319-340.
- Hall, M. G., 1972. Vortex breakdown. *Annual Reviews of Fluid Mechanics* 4, 195-218
- Hangan, H., and Kim, J., 2008. Swirl ratio effects on tornado vortices in relation to the Fujita scale. *Wind and Structures* 11(4), 291-302.

Harlow, F. H., and Stein, L. R., 1974. Structural analysis of Tornado like vortices. *Journal of the Atmospheric Sciences* 31, 2081-2098.

Hashemi-Tari, P., 2007. Swirl ratio effects on tornado-like vortices. Masters thesis, University of Western Ontario, Canada.

Hashemi-Tari, P., Gurka, R., and Hangan, H., 2010. Experimental investigation of tornado-like vortex dynamics with swirl ratio: The mean and turbulent flow fields. *Journal of Wind Engineering and Industrial Aerodynamics* 98, 936-944.

Jischke, M. C., and Parang, M., 1978. On Tornado Funnels. *Proceedings of the Oklahoma Academy of Science* 58, 81-87.

Klemp, J. B., and Wilhelmson, R. B., 1978, The simulation of three dimensional convective storm dynamics. *Journal of the Atmospheric Sciences* 35, 1070–1096.

Kuai, L., Haan, F. L., Gallus, W. A., and Sarkar, P. P., 2008. CFD simulations of the flow field of a laboratory-simulated tornado for parameter sensitivity studies and comparison with field measurements. *Wind and Structures* 11(2), 75-96.

Kuehnast, E. L., and Haines, D. A., 1971. Unusual Features Observed Within A Series Of Tornado Pictures. *Monthly Weather Review* 99, 545–548.

Lee, W-C., Wurman, J., 2005. Diagnosed three-dimensional axisymmetric structure of the Mulhall tornado on 3 May 1999. *Journal of the Atmospheric Sciences* 62, 2373-2394.

Lewellen, W. S., 1962. A solution for 3 dimensional vortex flows with strong circulation. *The Journal of Fluid Mechanics* 14, 420-432.

Lewellen, W. S., Lewellen, D. C., Sykes, R. I., 1997. Large-eddy simulation of a tornado's interaction with the surface. *Journal of the Atmospheric Sciences* 54, 581–605.

Lewellen, D. C., Lewellen, W. S., and Xia, J., 2000. The influence of a local swirl ratio on tornado intensification near the surface. *Journal of the Atmospheric Sciences* 57, 527–544.

Lugt, H., 1989. Vortex breakdown in atmospheric columnar vortices. *Bulletin of the American Meteorological Society* 70, 1526-1537.

Lund, D. E., and Snow, J. T., 1993. Laser Doppler velocimeter measurements in tornadolike vortices. *The Tornado: Its Structure, Dynamics, Prediction, and Hazards, Geophysical Monograph* 79, American Geophysical Union, 297-306.

Maxworthy, T., 1973. A vorticity source for large-scale dust devils and other comments on naturally occurring columnar vortices. *Journal of the Atmospheric Sciences* 30, 1717–1722.

Nolan, S. D., and Farrell, B. H., 1999. The structure and dynamics of tornado like vortices. *Journal of the Atmospheric Sciences* 56, 2908-2936.

Pauley, R. L., Church, C. R., and Snow, J. T., 1982. Measurements of Maximum Surface Pressure Deficits in Modeled Atmospheric Vortices. *Journal of the Atmospheric Science* 39, 369–377.

Pauley, R. L., 1989. Laboratory Measurements of Axial Pressures in Two-Celled Tornado-like Vortices. *Journal of the Atmospheric Science* 46, 3392–3399.

Rotunno, R., 1977. Numerical simulation of a laboratory vortex. *Journal of the Atmospheric Sciences* 34, 1942-1956, 1977.

Rotunno, R., 1979. A study in tornado like vortex dynamics. *Journal of the Atmospheric Sciences* 36, 140-155.

Rotunno, R., 1984. An investigation of a three dimensional asymmetric vortex. *Journal of the Atmospheric Sciences* 41, 283-298.

Smith, D. R., 1987. Effect of Boundary Conditions on Numerically Simulated Tornado-like Vortices. *Journal of the Atmospheric Science* 44, 648–656.

Snow, J. T., Church, C. R., and Barnhart, B. J., 1980. An Investigation of the Surface Pressure Fields beneath Simulated Tornado Cyclones. *Journal of the Atmospheric Science* 37, 1013–1026.

Snow, J. T., and Lund, D. E., 1988. A second generation tornado vortex chamber at Purdue University. Preprints, 13th Conference on Severe Local Storms, Tulsa, Oklahoma, American Meteorological Society, 323-326.

Xia, J., Lewellen, W. S., and Lewellen, D. C., 2003. Influence of Mach number on tornado corner flow dynamics. *Journal of the Atmospheric Sciences* 60, 2820–2825.

Ward, N. B., 1972. The exploration of certain features of tornado dynamics using a laboratory model. *Journal of the Atmospheric Sciences* 29, 1194-1204.

Wicker, L. J., and Wilhelmson, R. B., 1995. Simulation and analysis of tornado development and decay within a three dimensional supercell thunderstorm. *Journal of the Atmospheric Sciences* 52(15), 2675–2703.

Wilson, T., and Rotunno, R., 1986. Numerical simulation of a laminar end-wall vortex and boundary layer. *Physics of Fluids* 29(12), 3993-4005.

Wurman, J., Straka, J., and Rasmussen, E., 1996. Fine Scale Doppler Radar Observation of Tornadoes. *Science* 272, 1774-1777.



Wurman, J., 2002. The Multiple-Vortex Structure of a Tornado. *Weather and forecasting* 17, 473–505.

(a)

Surface Name	Boundary Conditions
Base	No-slip wall
Side wall	Free-slip wall
Inlet	Velocity inlet
Outlet	Outflow

(b)

Name	Dimensions (m)
$R_0$	0.4
$H_0$	0.41
L	1.66

Table 2.1: (a) Boundary conditions and (b) domain dimensions used in the current simulations

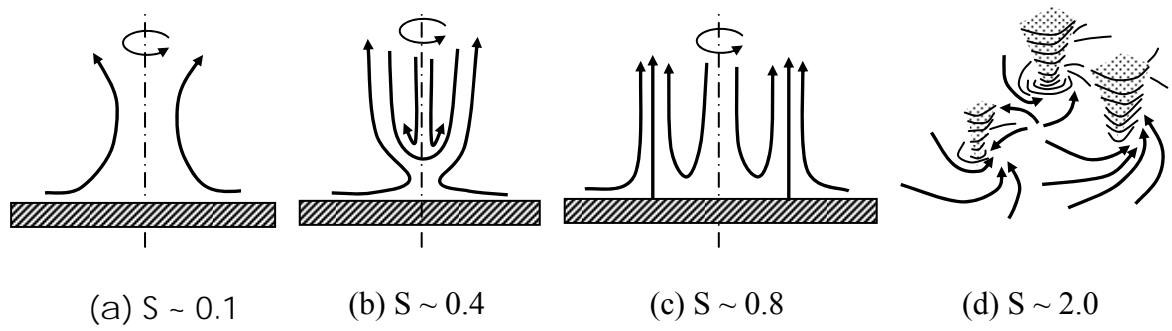


Figure 2.1: Sketch of the pathlines of the flow observed at various swirl ratios. Lugt (1989), Davies-Jones (1986)

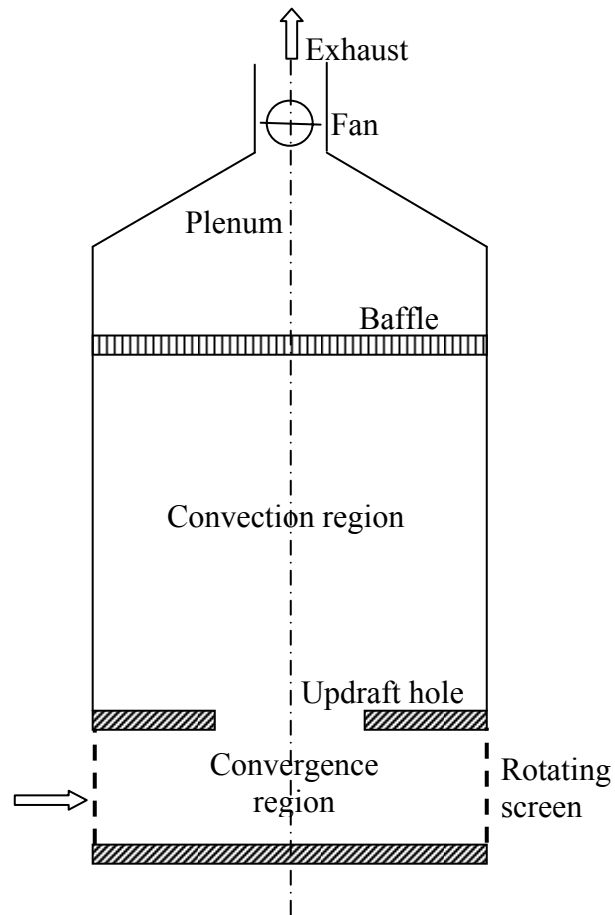


Figure 2.2: Sketch of a Ward-type TVC (Church et.al. 1979)

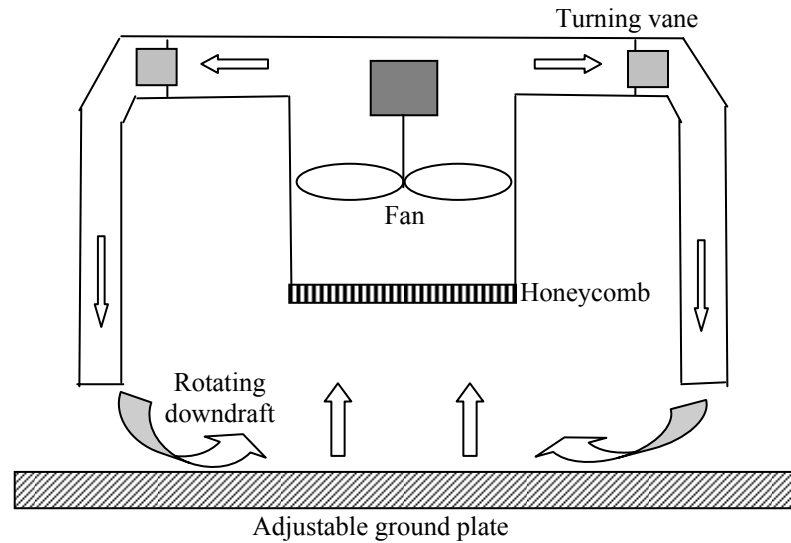


Figure 2.3: Sketch of an Iowa-type TVC (Haan Jr, 2007)

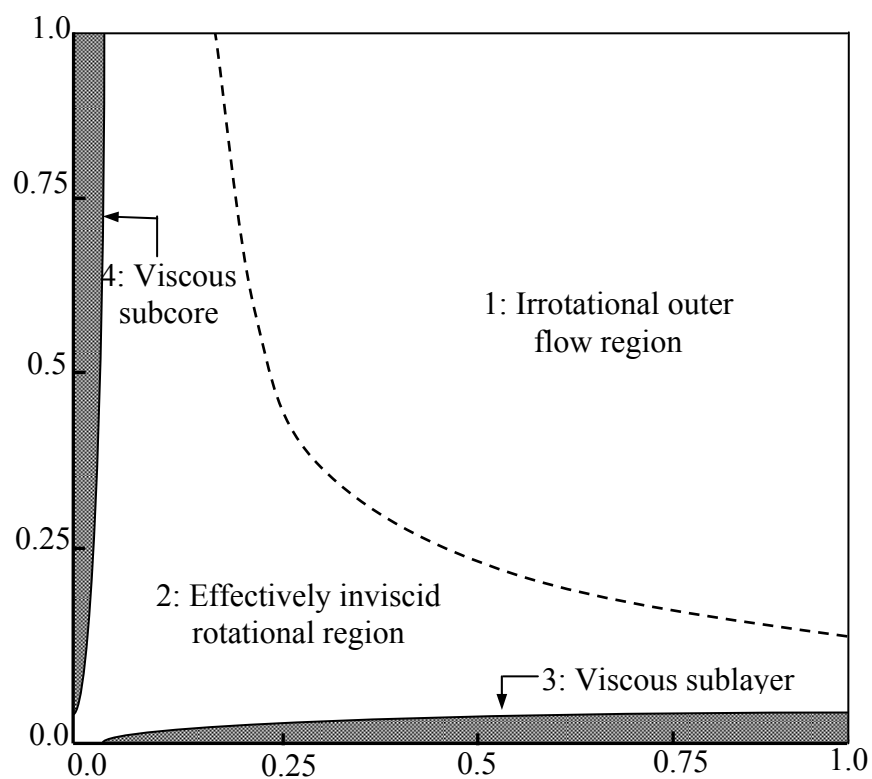


Figure 2.4: Sketch of the four regions of the low swirl vortex flow. (Wilson and Rotunno 1986)

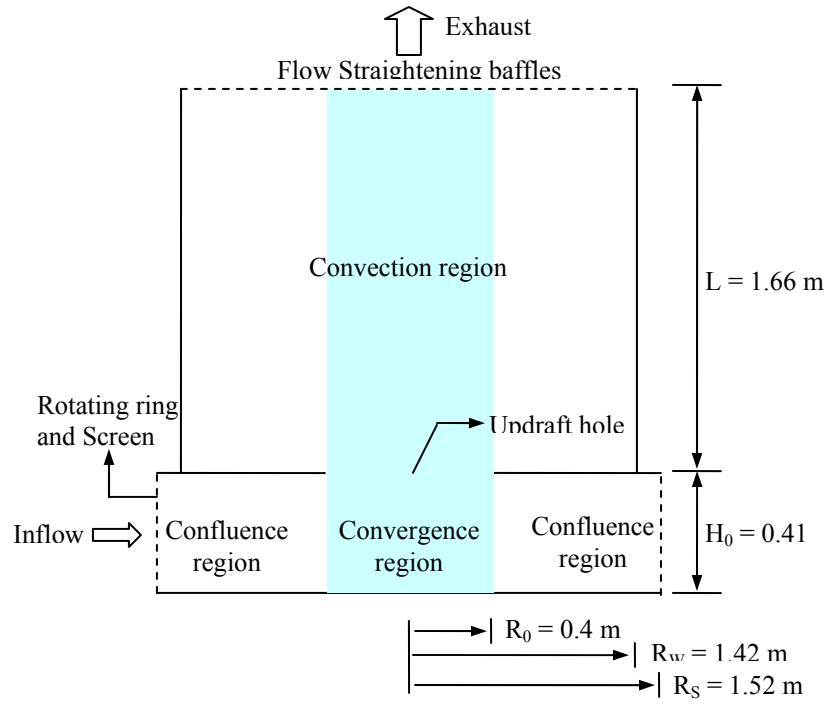


Figure 2.5a: Schematic diagram of the cross section of Ward type Purdue TVC with blue region showing domain modeled in the current simulations. (Adapted from Church et.al. 1979)

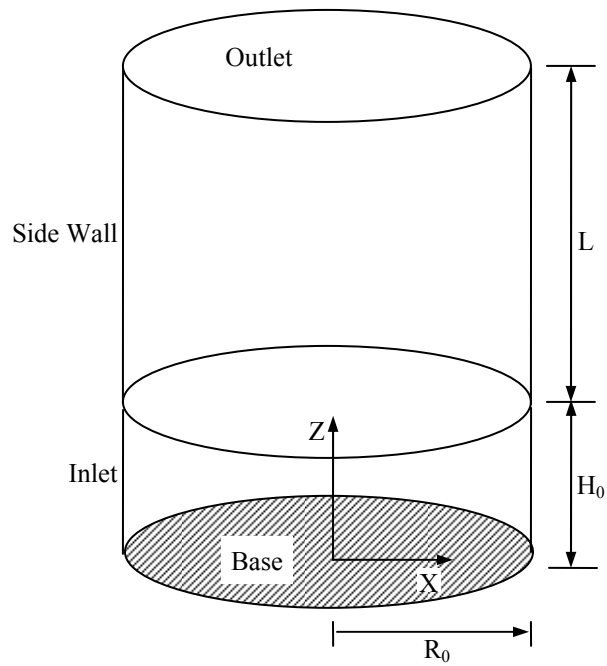


Figure 2.5b: Schematic diagram of the domain modeled in the current simulations.

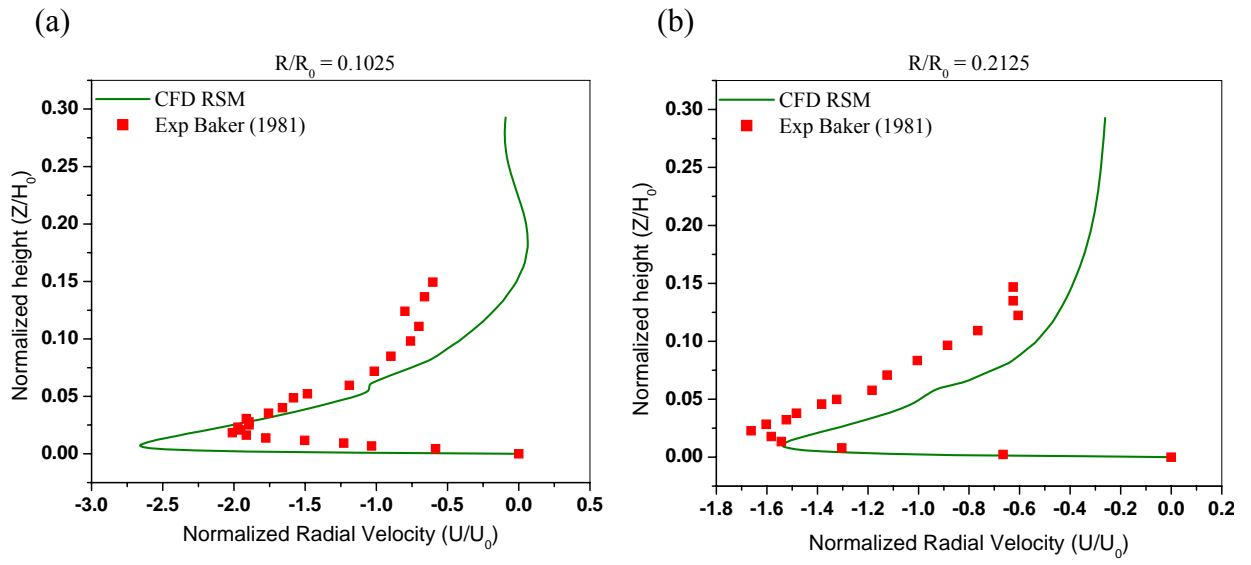


Figure 2.6: Plots comparing the radial velocity of the current CFD simulation and Baker (1981) experimental results. (a)  $S = 0.28$ ,  $R/R_0 = 0.1025$  (b)  $S = 0.28$ ,  $R/R_0 = 0.2125$ .

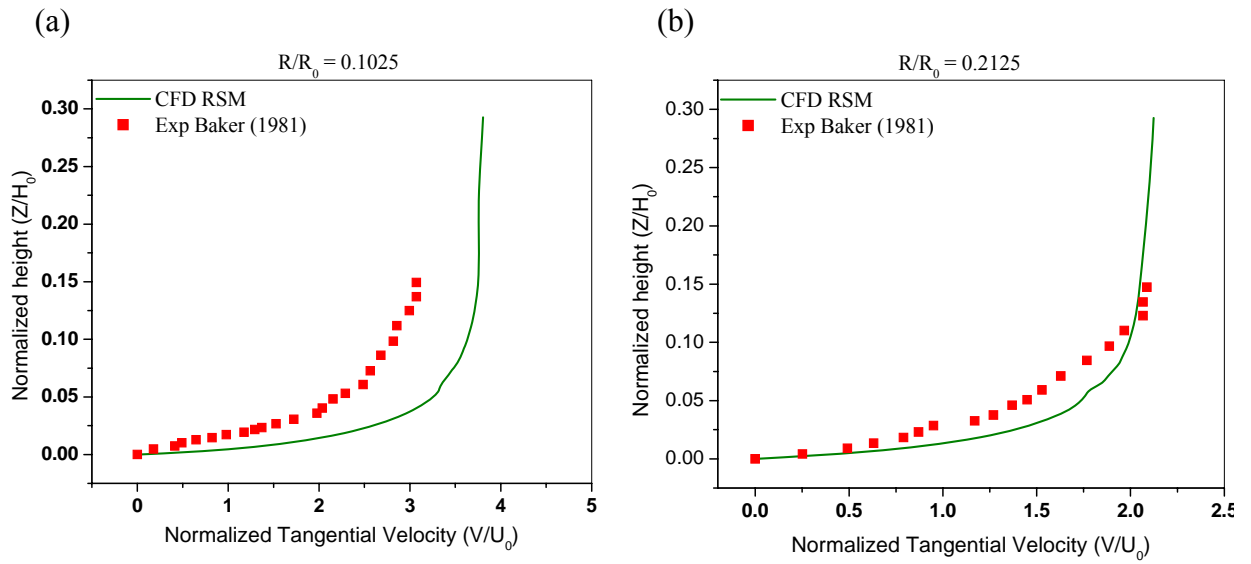


Figure 2.7: Plots comparing the tangential velocity of the current CFD simulation and Baker (1981) experimental results. (a)  $S = 0.28$ ,  $R/R_0 = 0.1025$  (b)  $S = 0.28$ ,  $R/R_0 = 0.2125$ .

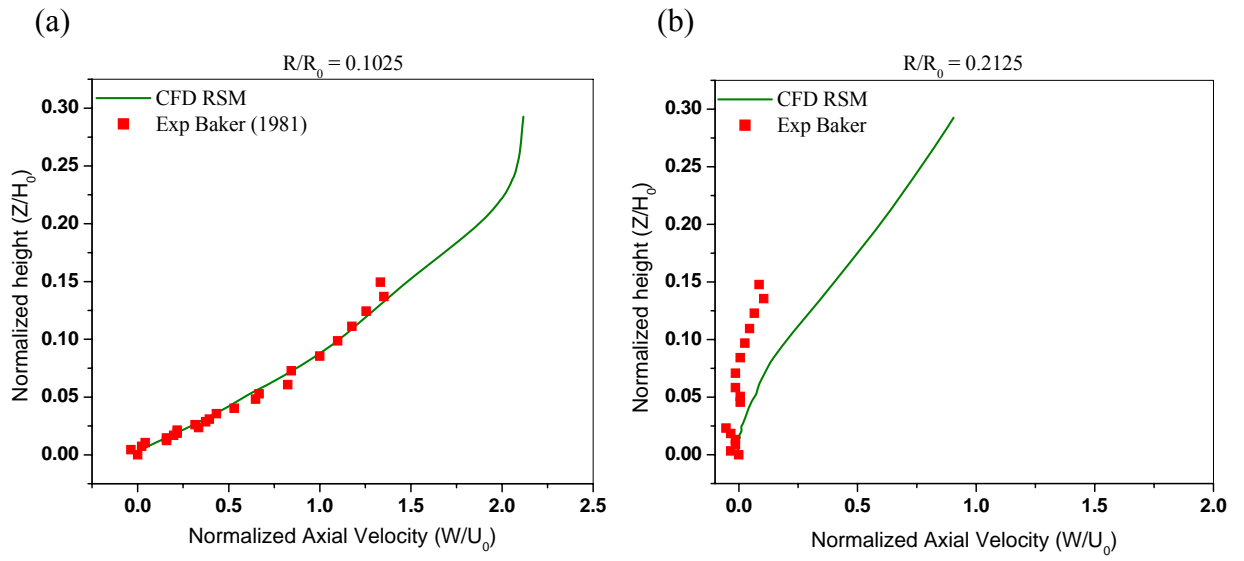


Figure 2.8: Plots comparing the axial velocity of the current CFD simulation and Baker (1981) experimental results. (a)  $S = 0.28$ ,  $R/R_0 = 0.1025$  (b)  $S = 0.28$ ,  $R/R_0 = 0.2125$ .

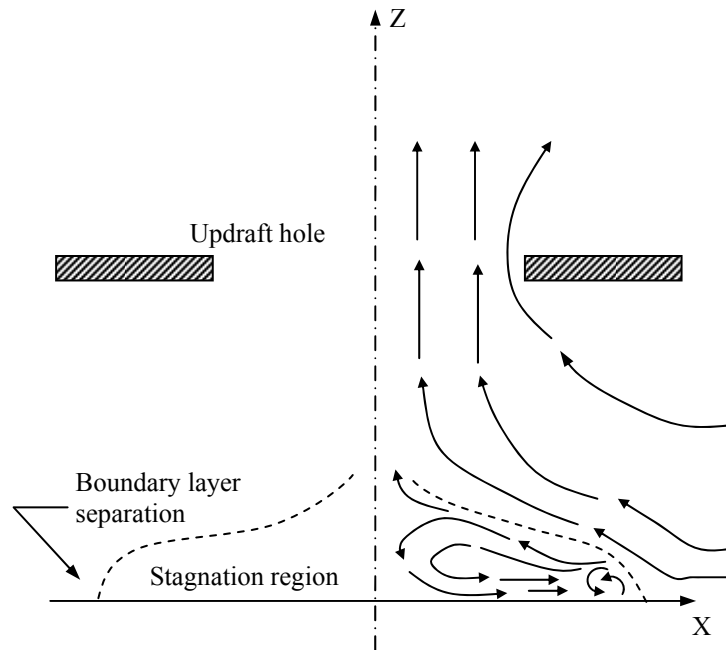


Figure 2.9: Sketch of the flow observed in no-swirl  $S = 0$  case. (Church et.al 1979)

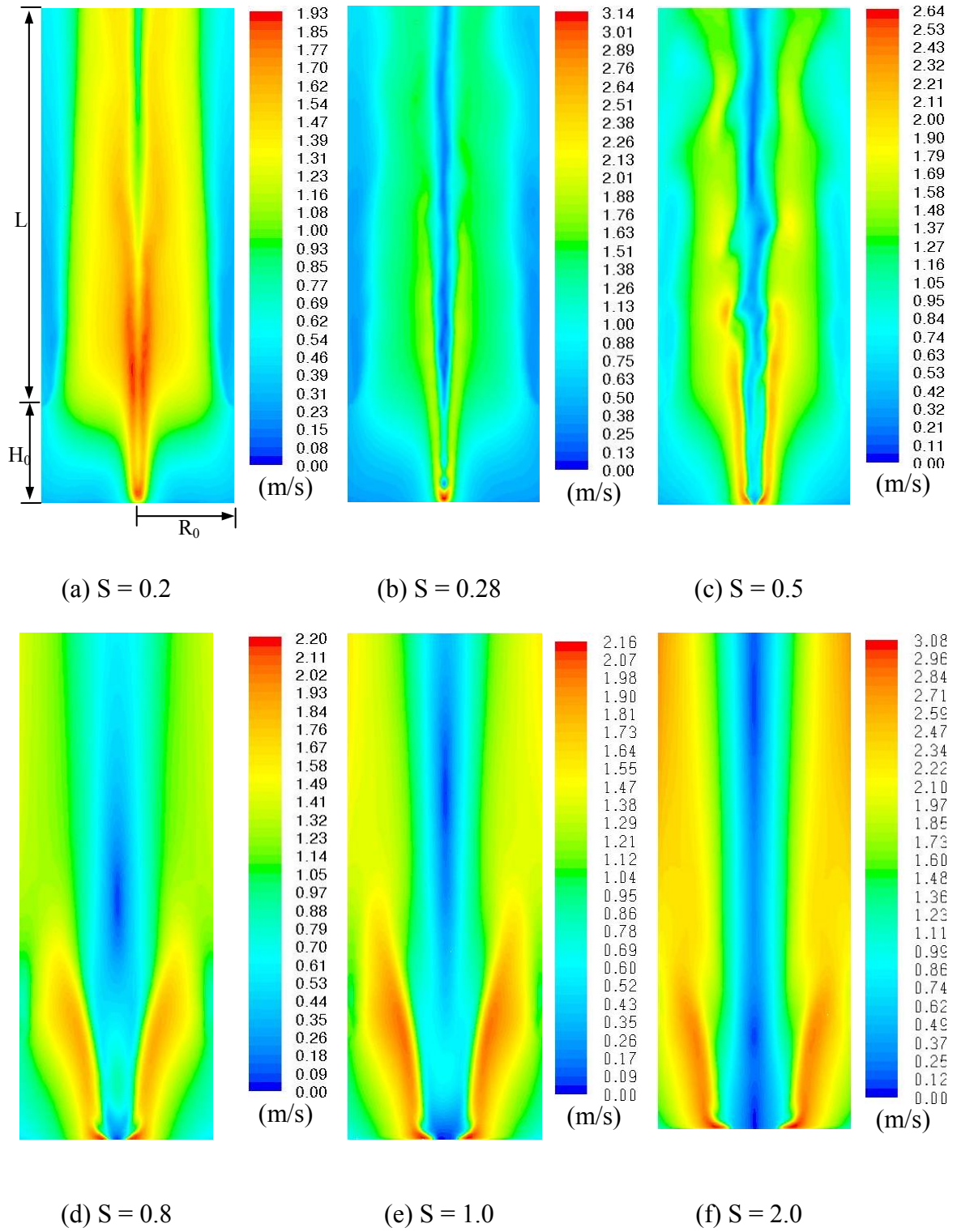


Figure 2.10: Contour plot of the velocity for Swirl ratios  $S = 0.2, 0.28, 0.5, 0.8, 1.0, 2.0$ .



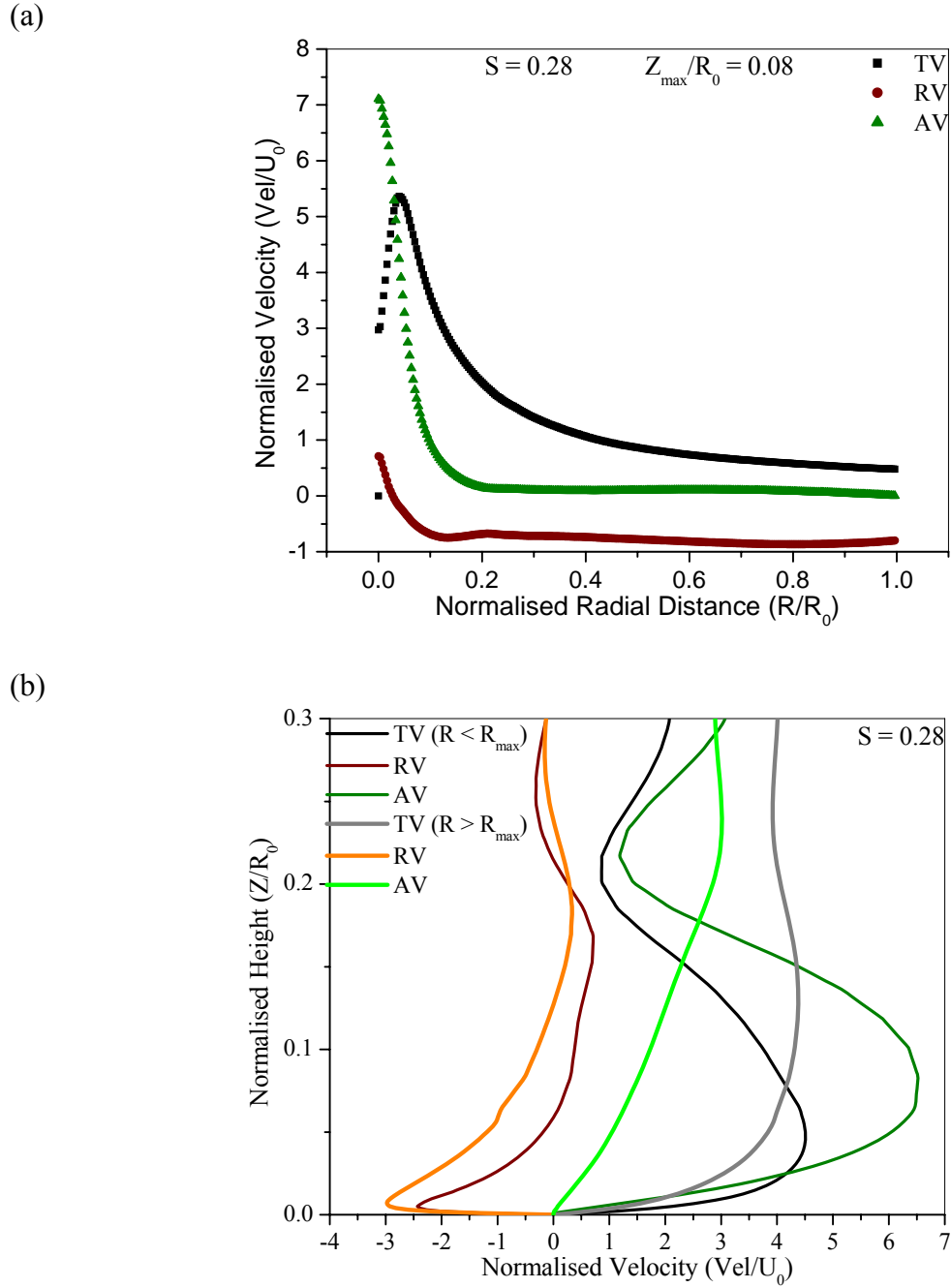


Figure 2.11: Velocity profile for Swirl ratio  $S = 0.28$  (a) Azimuthally averaged axial, radial and tangential velocity along the radial distance at height  $Z_{\max}$  (Height of maximum tangential velocity) (b) Azimuthally averaged axial, radial and tangential velocity along the height at radial locations inside and outside the core of the tornado. The continuous line represents velocities inside the core at  $R/R_0 = 0.016$  and dots represent the velocities outside the core at  $R/R_0 = 0.08$ .

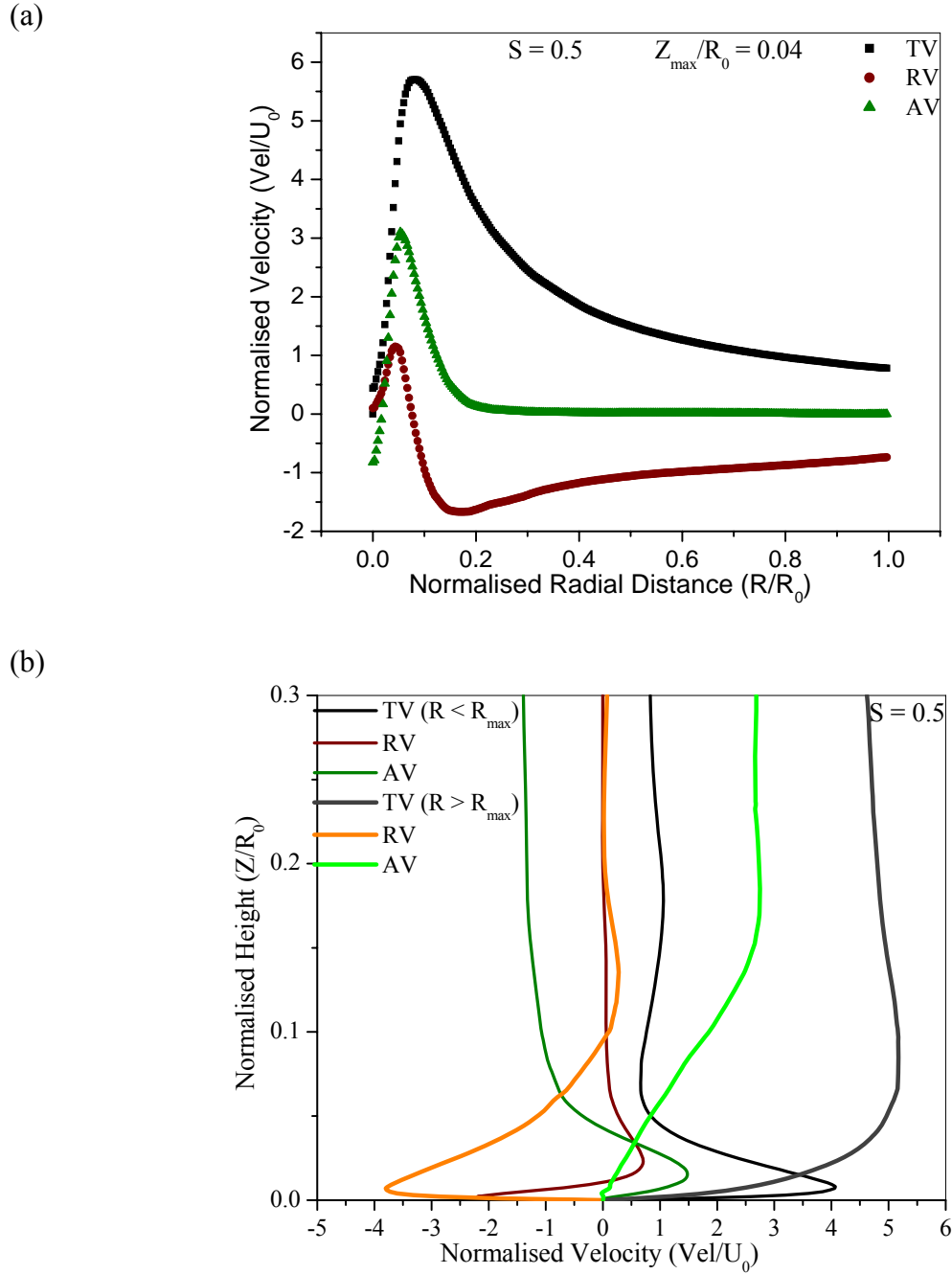


Figure 2.12: Velocity profile for Swirl ratio  $S = 0.5$  (a) Azimuthally averaged axial, radial and tangential velocity along the radial distance at height  $Z_{\max}$  (Height of maximum tangential velocity) (b) Azimuthally averaged axial, radial and tangential velocity along the height at radial locations inside and outside the core of the tornado. The continuous line represents velocities inside the core at  $R/R_0 = 0.02$  and dots represent the velocities outside the core at  $R/R_0 = 0.14$ .

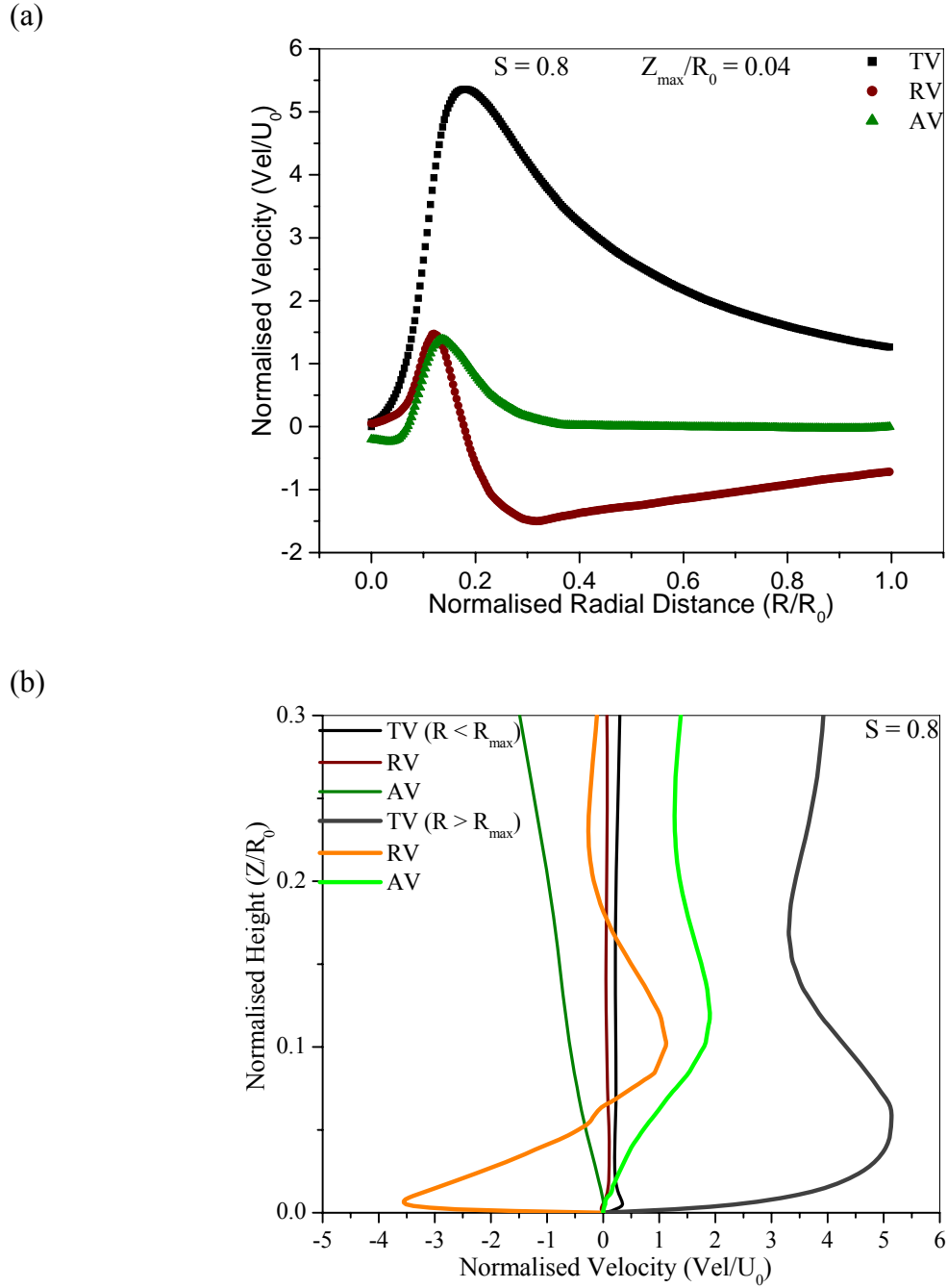


Figure 2.13: Velocity profile for Swirl ratio  $S = 0.8$  (a) Azimuthally averaged axial, radial and tangential velocity along the radial distance at height  $Z_{\max}$  (Height of maximum tangential velocity) (b) Azimuthally averaged axial, radial and tangential velocity along the height at radial locations inside and outside the core of the tornado. The continuous line represents velocities inside the core at  $R/R_0 = 0.025$  and dots represent the velocities outside the core at  $R/R_0 = 0.23$ .

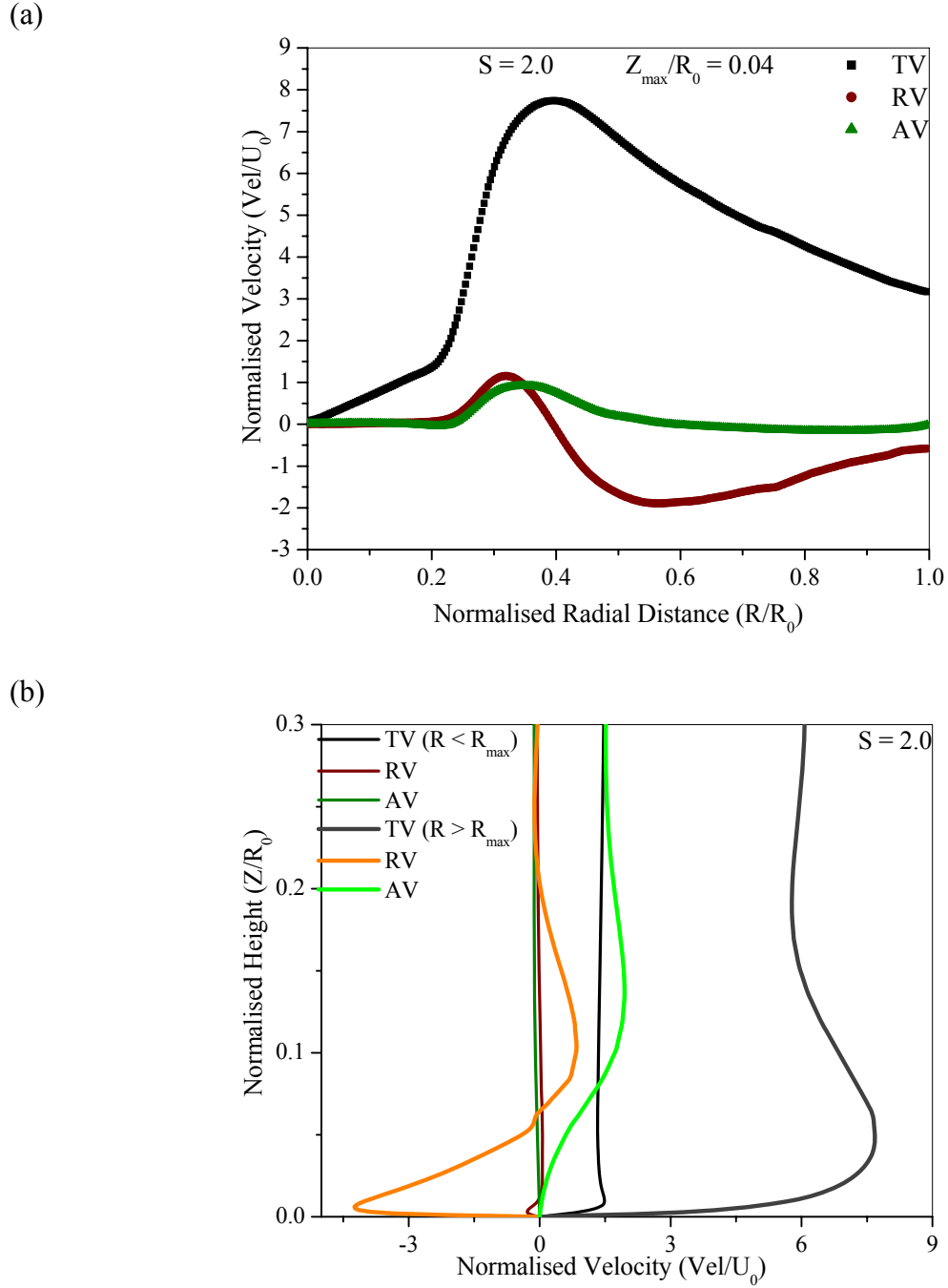
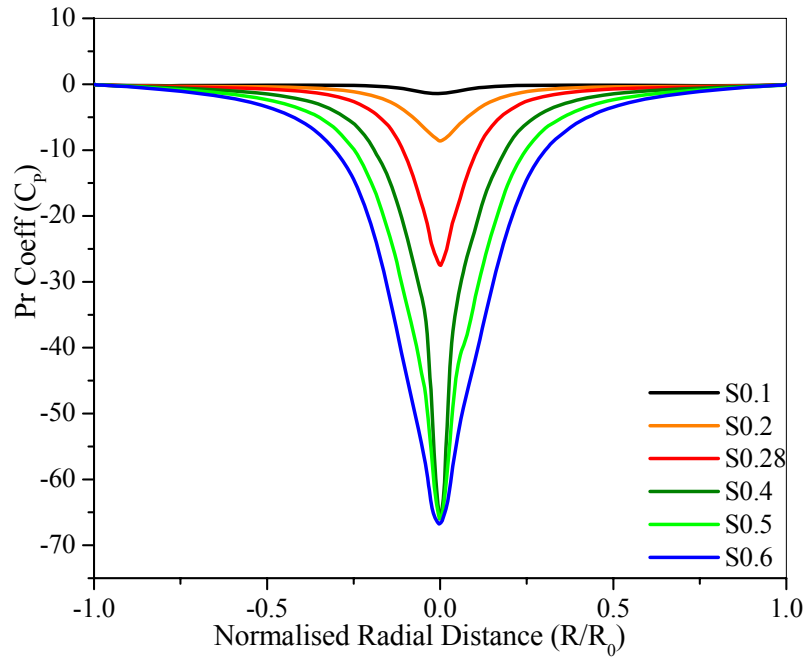


Figure 2.14: Velocity profile for Swirl ratio  $S = 2.0$  (a) Azimuthally averaged axial, radial and tangential velocity along the radial distance at height  $Z_{\max}$  (Height of maximum tangential velocity) (b) Azimuthally averaged axial, radial and tangential velocity along the height at radial locations inside and outside the core of the tornado. The continuous line represents velocities inside the core at  $R/R_0 = 0.2$  and dots represent the velocities outside the core at  $R/R_0 = 0.45$ .

(a)



(b)

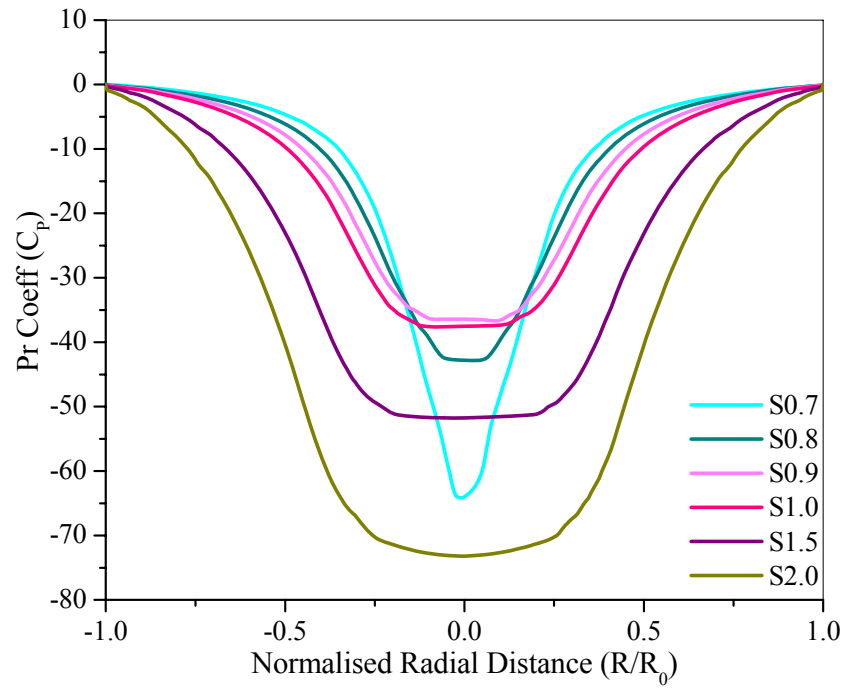


Figure 2.15: Surface pressure deficit along the radial distance for different swirl ratios (a)  $S = 0.1, 0.2, 0.28, 0.4, 0.5$ , and  $0.6$  (b)  $S = 0.7, 0.8, 0.9, 1.0, 1.5$ , and  $2.0$

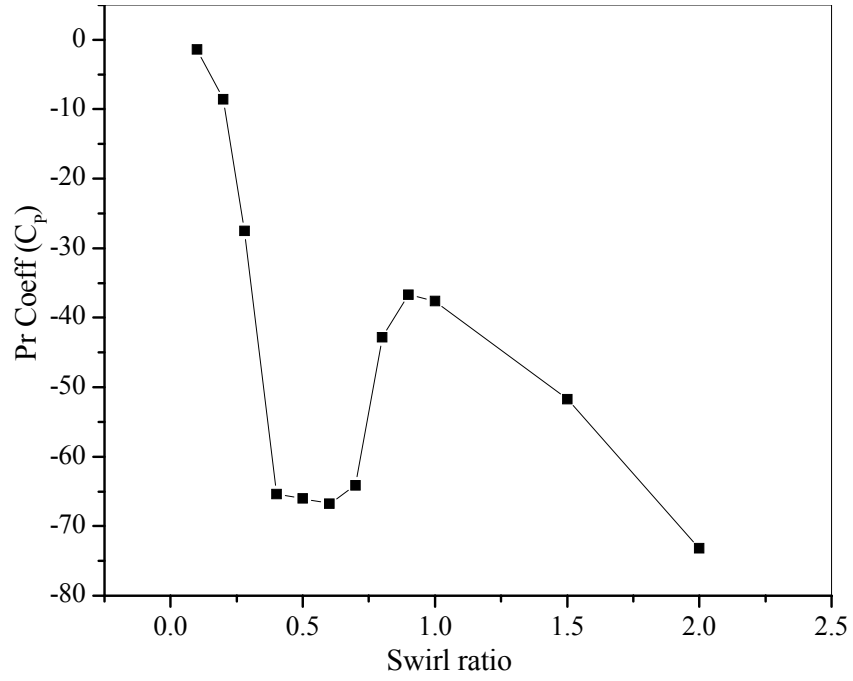


Figure 16: The plot of maximum central pressure deficit vs. swirl ratio

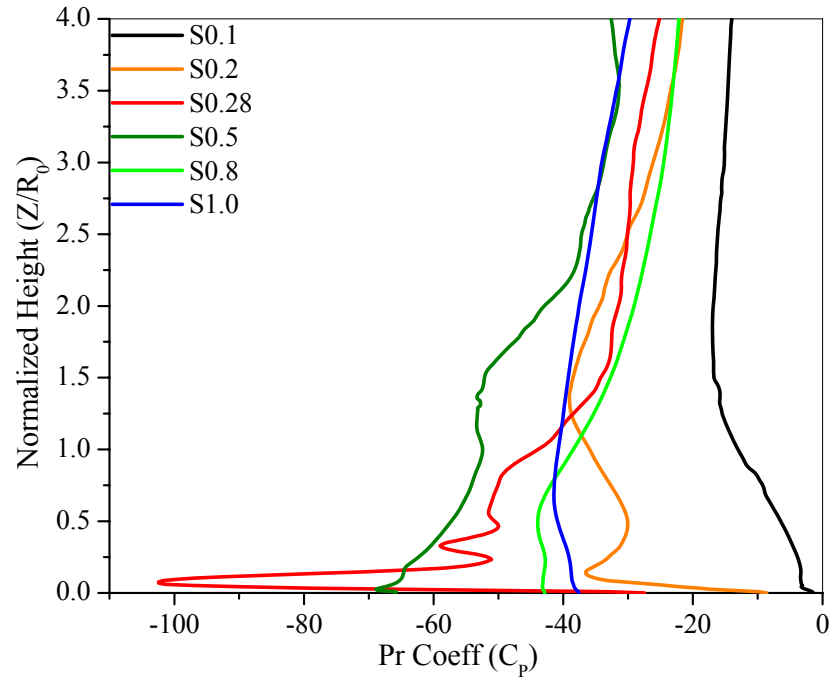


Figure 2.17: The plot of maximum pressure deficit at  $R/R_0 = 0$  along the normalized height for swirl ratios  $S = 0.1, 0.2, 0.28, 0.5, 0.8, 1.0$ .

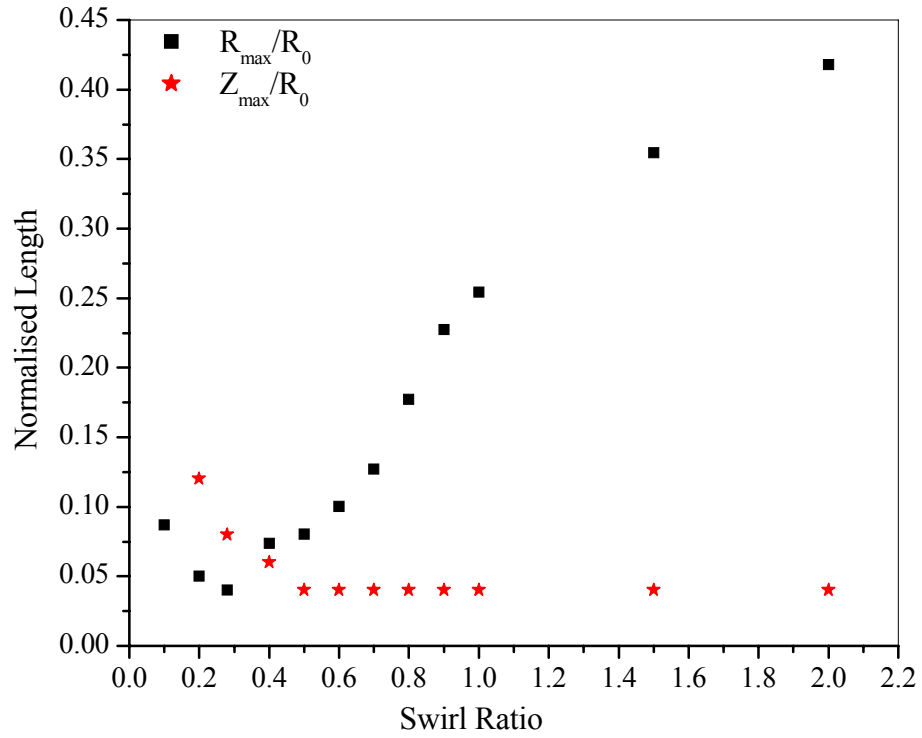


Figure 2.18: The plot of normalized core radius ( $R_{\max}/R_0$ ) and the normalized height from the base at which the radius is measured ( $Z_{\max}/R_0$ ) for various Swirl ratios (0.2-2.0)

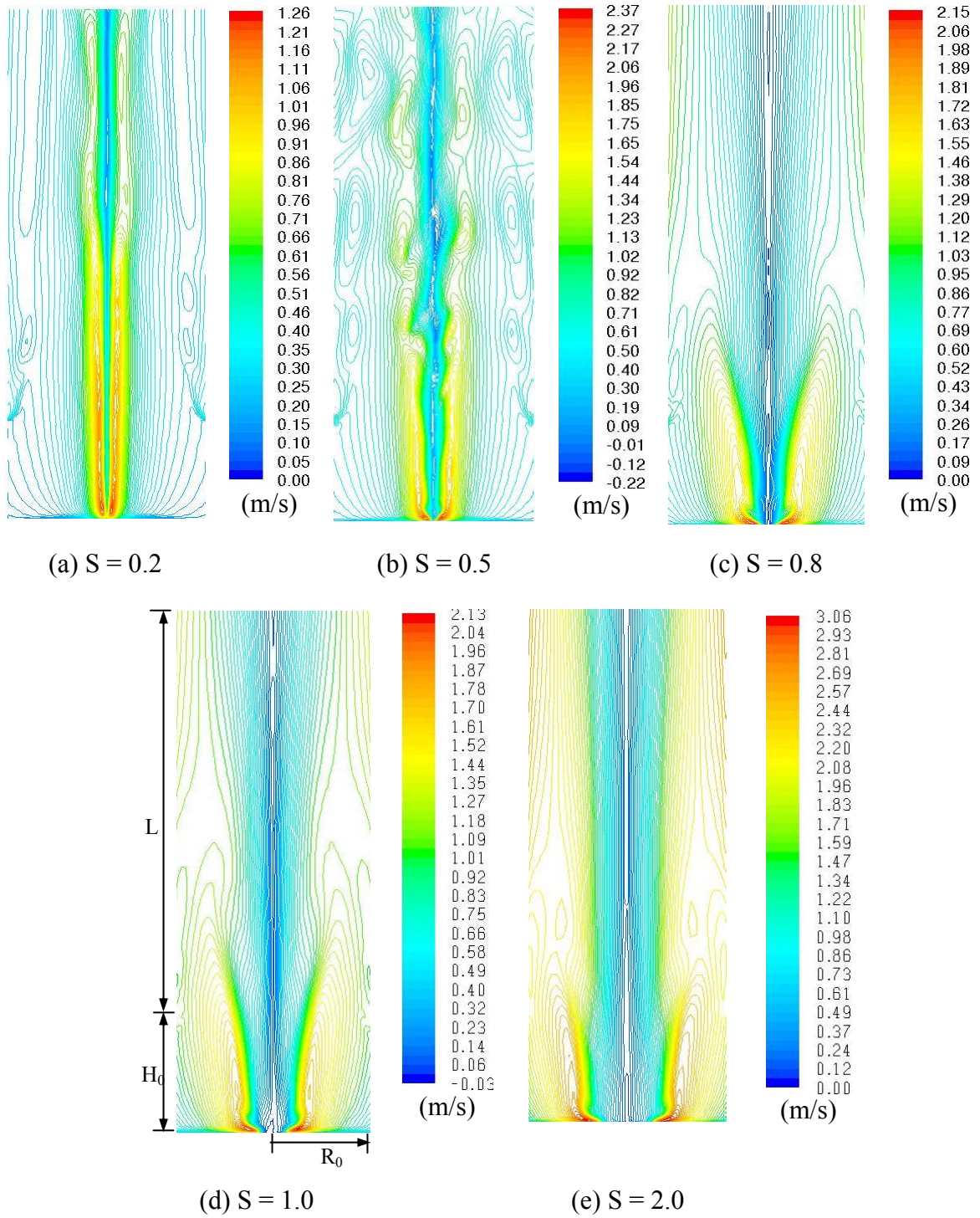


Figure 2.19: Contour plot of tangential velocity for Swirl ratio  $S = 0.2, 0.5, 0.8, 1.0, 2.0$



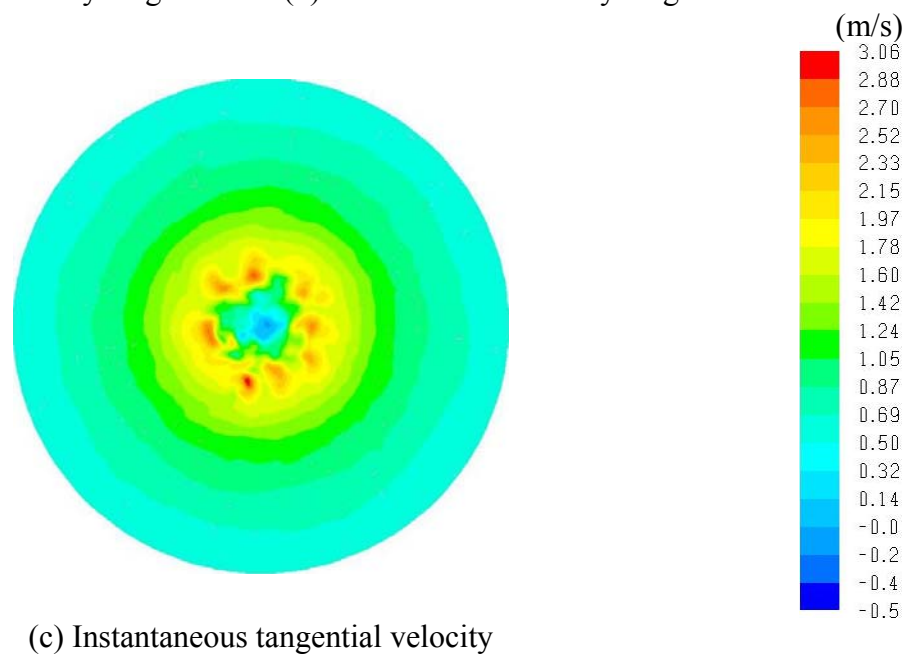
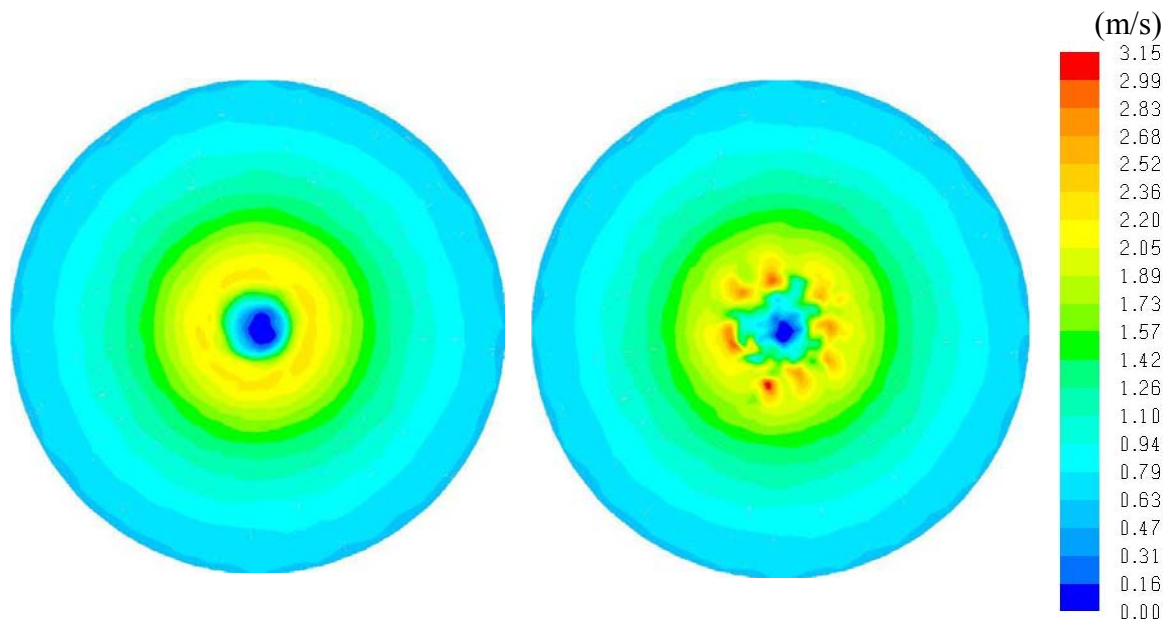


Figure 2.20: LES velocity contours for  $S = 1.0$  at  $Z/R_0 = 0.02$

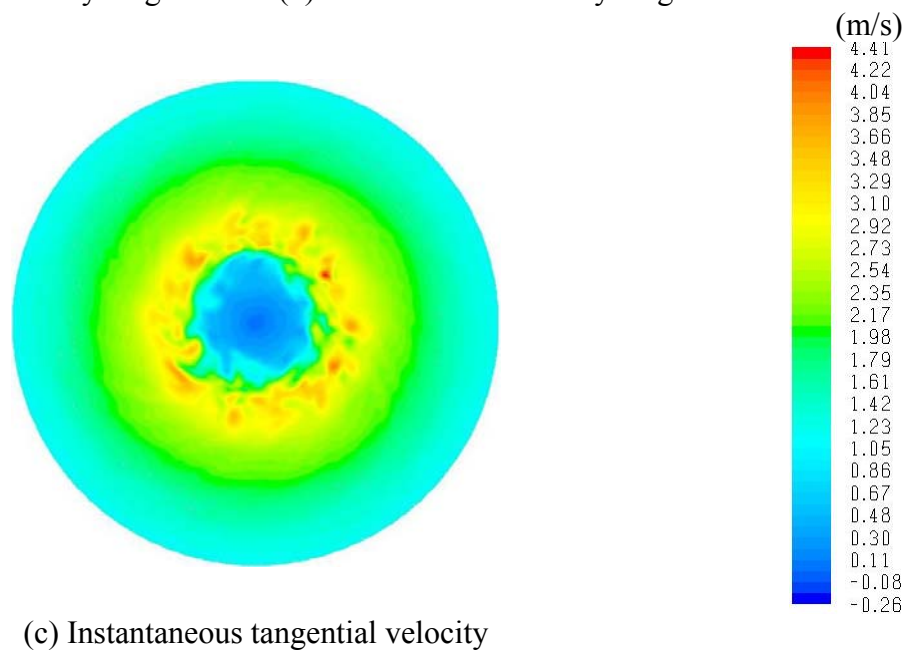
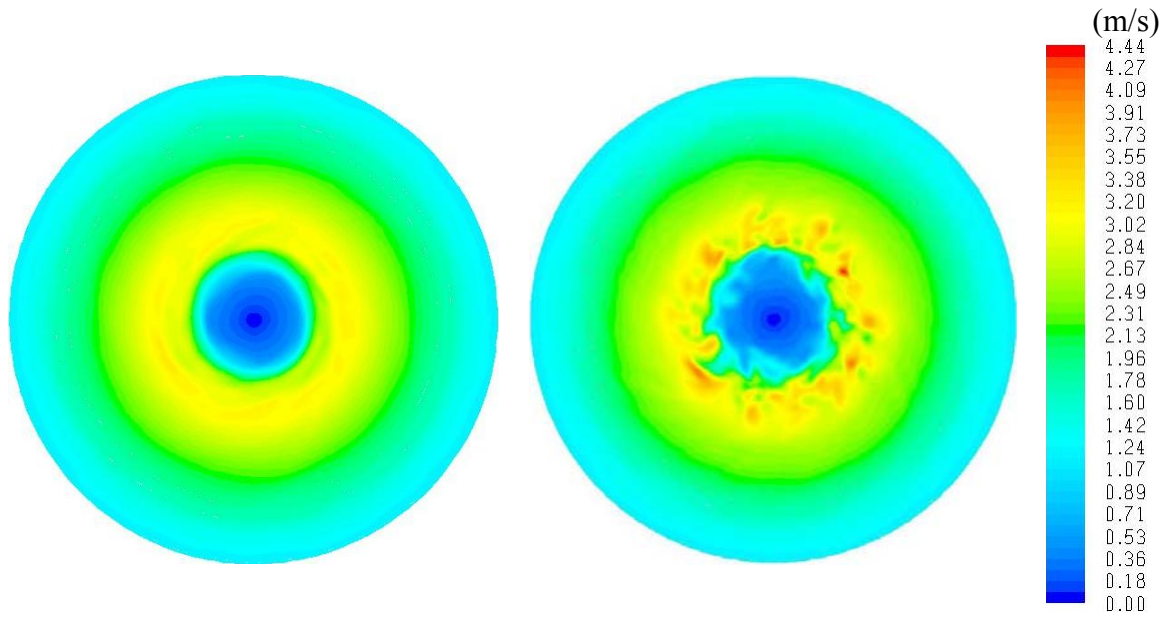


Figure 2.21: LES velocity contours for  $S = 2.0$  at  $Z/R_0 = 0.02$

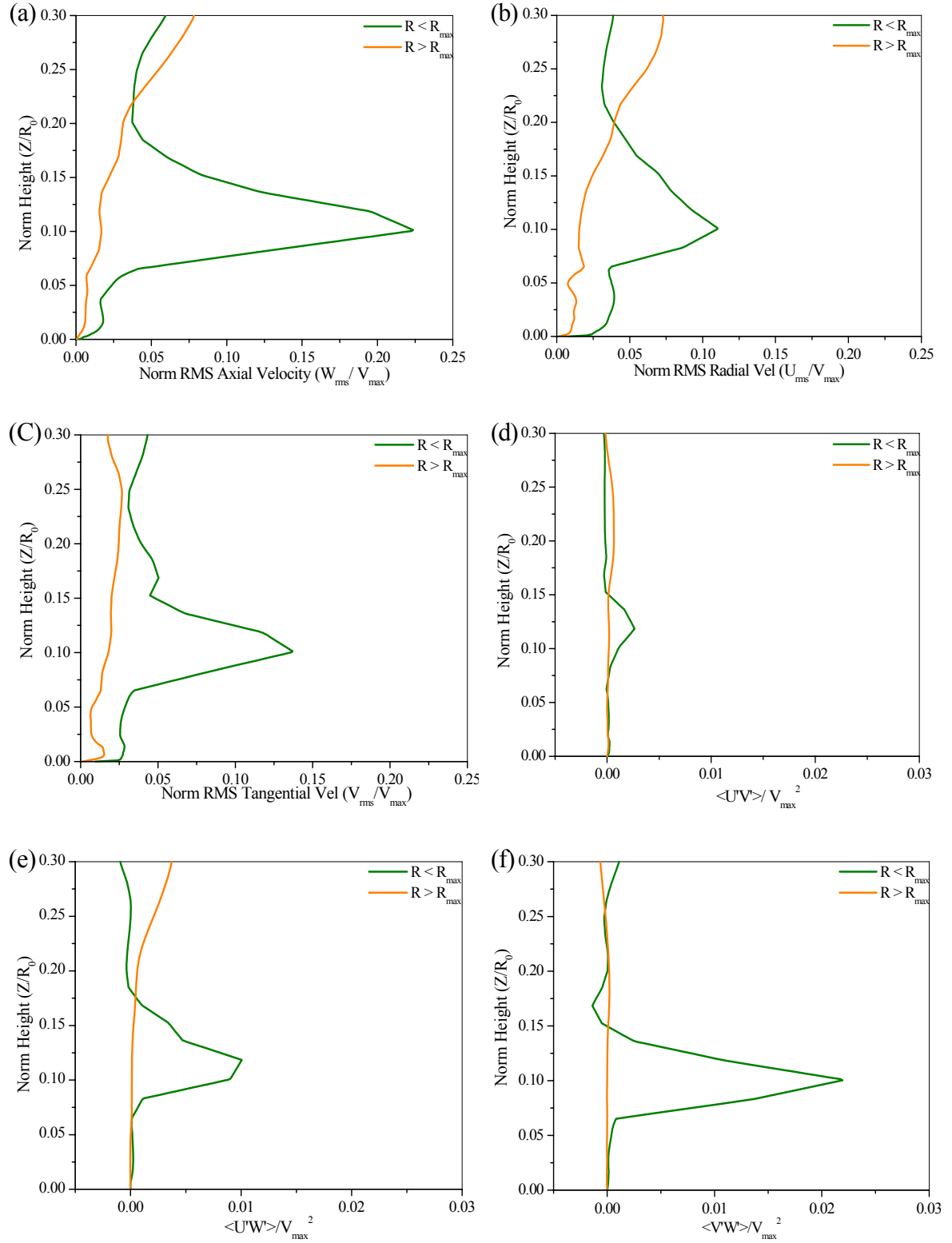


Figure 2.22: The plot of RMS velocities and Reynolds shear stress along the height for Swirl ratio  $S = 0.28$  at radial locations inside the core ( $R < R_{\max}$ ) at  $R/R_0 = 0.016$  and outside the core ( $R > R_{\max}$ ) at  $R/R_0 = 0.08$ .

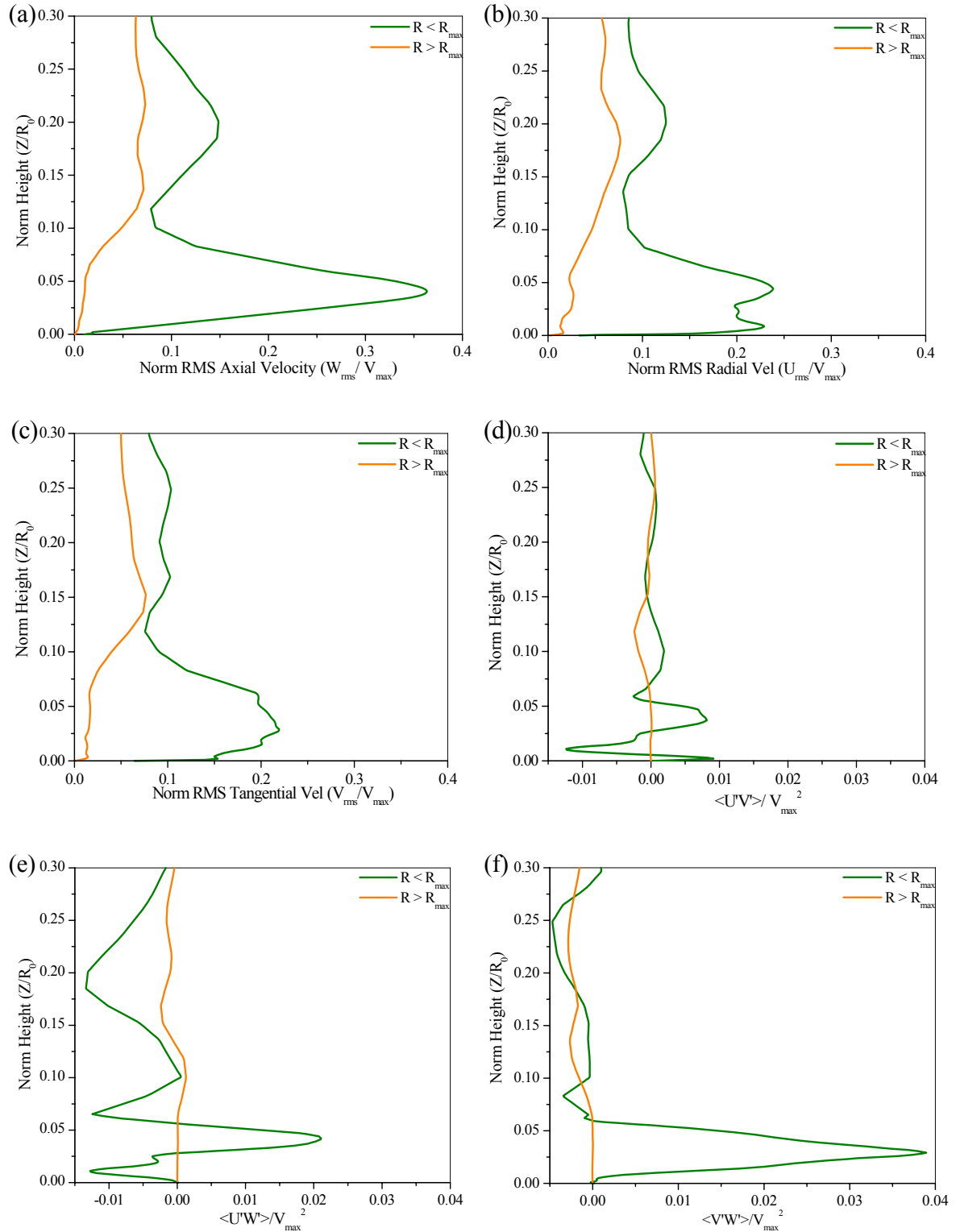


Figure 2.23: The plot of RMS velocities and Reynolds shear stress along the height for Swirl ratio  $S = 0.5$  at radial locations inside the core ( $R < R_{\max}$ ) at  $R/R_0 = 0.02$  and outside the core ( $R > R_{\max}$ ) at  $R/R_0 = 0.14$ .

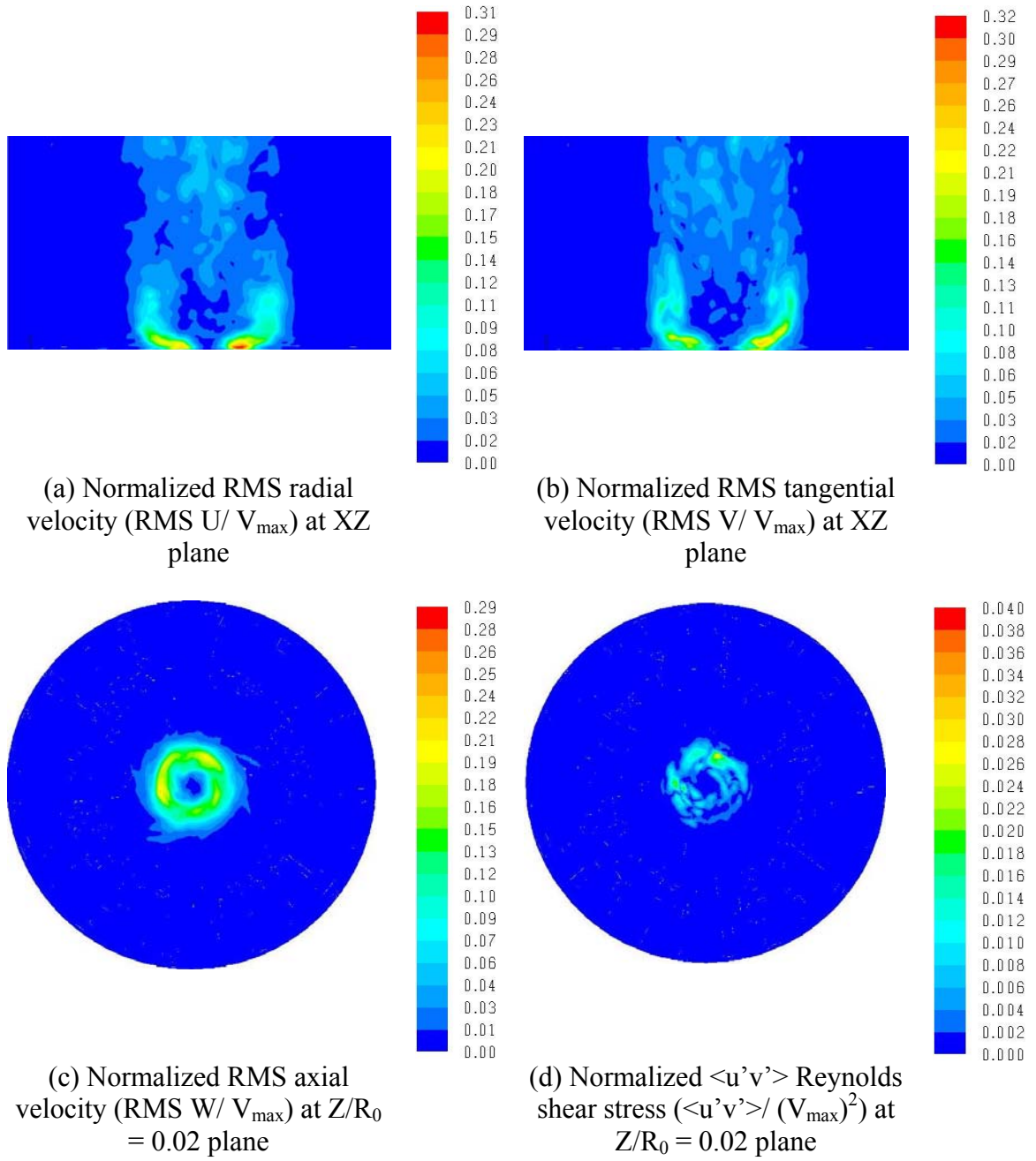


Figure 2.24: Turbulence characteristics for  $S = 1.0$

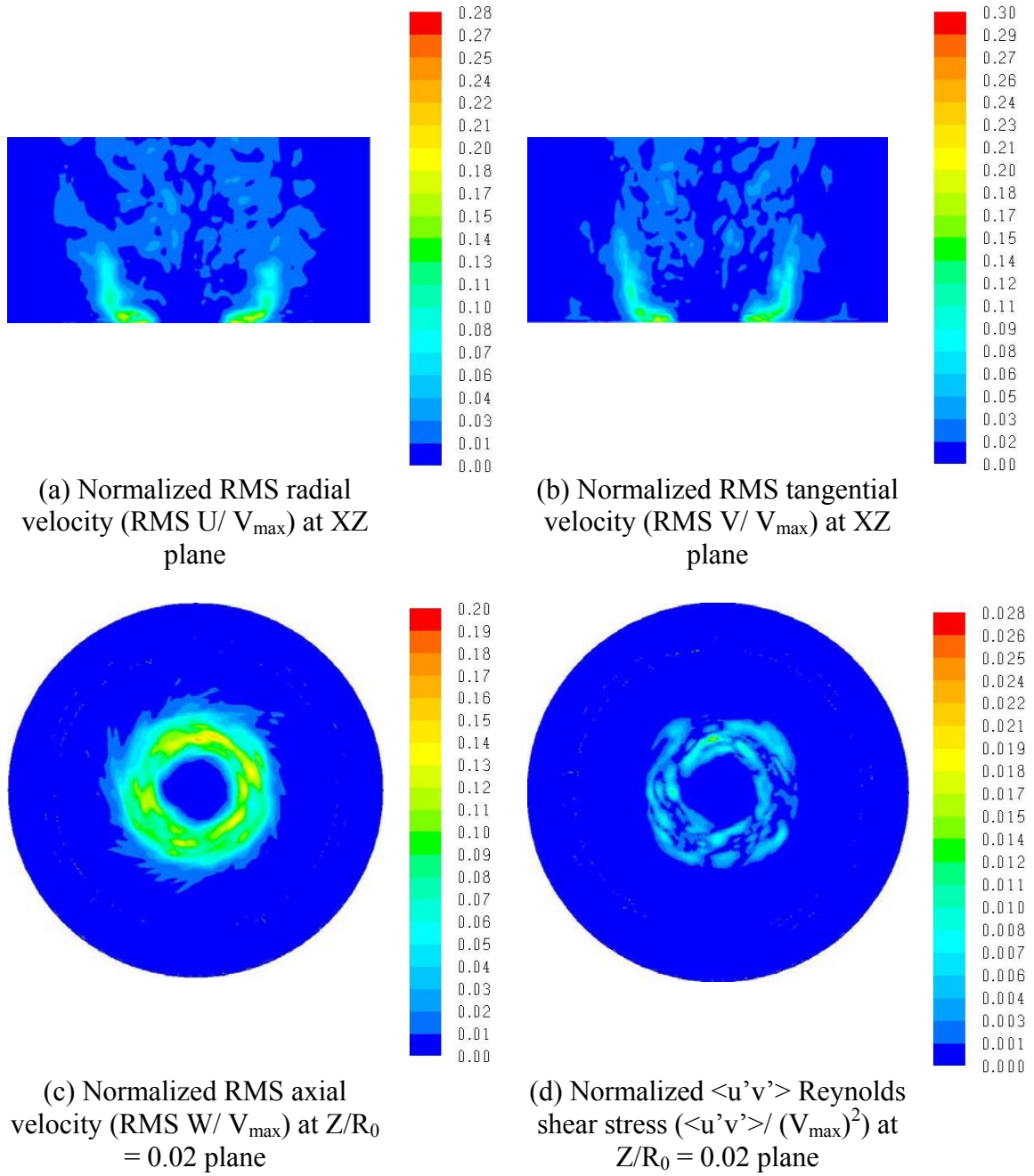


Figure 2.25: Turbulence characteristics for  $S = 2.0$

## **Chapter 3: Effects of translation and surface roughness on tornado-like vortices**

### **3.1 Introduction:**

Chapter 2 has presented the results of numerical simulations of laboratory scale tornado for a comprehensive range of swirl ratios between 0.1 and 2.0. The validity of the results was proven by comparing them with those of past studies for certain select scenarios/conditions. Typically, tornadoes produce very high velocities close to the surface and in this region the flow is sensitive to the interaction of the vortex with the base surface (Lewellen 1993, Lewellen et al. 1997). In this context, it has been recognized that translation of the vortex and surface roughness are two important factors that affect tornadic flow. This chapter investigates how the characteristics of the laboratory scale tornadic flow are modified as a result of translation and surface roughness. Since swirl ratio  $S$  is known to be the dominant governing parameter for tornado-like flows, (Church et. al. 1979, Ward 1972, and Rotunno 1977), it is important that the study is carried out for a range of relevant swirl ratios.

Literature review shows that while past studies have investigated these effects, their scope is usually confined to specific observable or specific values of swirl ratio. Dessens (1972) and Leslie (1977) have studied the effects of surface roughness on tornadic flows in laboratory simulations. Their studies have shown that the increase in surface roughness causes the radial and axial velocities to increase and tangential velocities to decrease. Church and Snow (1993) argued that in these earlier experimental studies, roughness elements used in the simulations were extreme when compared to atmospheric roughness. Consequently, the effect of roughness may have been over stated in some of the results. Rostek and Snow (1985) used properly scaled surface roughness elements in a laboratory simulation, but only studied the roughness effect on radial surface pressure deficit for different swirl ratios.

Lewellen and Sheng (1979) have analyzed the effect of surface roughness numerically and arrived at conclusions similar to that of laboratory simulations. However, their study only addressed two swirl ratios. Recently Kuai et al. (2008) have numerically studied the effect of surface roughness for swirl ratios less than 0.21.

Diamond and Eugene (1984) performed laboratory simulations of translating vortices and observed secondary trailing vortices. Lewellen et al. (1997) numerically simulated a full scale tornado for high swirl ratio ( $S = 0.94$ ) and observed that introducing translation resulted in a slight increase in the maximum mean velocity. The simulations do not discuss the effect of translation on low swirl ratios.

The present work attempts to address the effects of translation and surface roughness on tornado-like flows for a set of swirl ratios ( $S = 0.28, 0.5, 1.0$  and  $2.0$ ) representing the low and high swirl ranges. This set of ratios is chosen because distinct flow features like the initial appearance of vortex-break-down (VBD) ( $S = 0.28$ ), vortex-touch-down (VTD) ( $S = 0.5$ ) and occurrence of multiple vortices ( $S = 1.0$  and  $2.0$ ) take place at these swirl ratios, as discussed in chapter 2. Also maximum tangential velocities are observed during the VTD ( $S = 0.5$ ) and at multiple vortex stage ( $S = 2.0$ ). Sections 3.2 and 3.3 describe the effect of translation and surface roughness, respectively. Conclusions are presented in section 3.4.

## **3.2 Translation Effects:**

### **3.2.1 Numerical Setup:**

The computational software Fluent 6.3 was used for the simulations. The domain is the same as described in section 2.2.1. Large Eddy Simulation (LES) was used with Dynamic Smagorinsky-Lilly subgrid model for all swirl ratios. The segregated implicit solver, SIMPLEC pressure velocity coupling and bounded central difference discretization scheme for momentum equations were used. A time step of  $\Delta t = 0.0001$  was used for all simulation. Grid convergence test (2-3% variation in the maximum velocity near the



base) was performed and a maximum of around 1,500,000 cells were used in the simulations.

In real life situation, translation of a vortex refers to the movement of the vortex relative to the fixed ground surface. To simulate this numerically, it is computationally convenient to keep the vortex stationary and instead move the base surface in a direction opposite to the direction of the vortex translation, thereby generating the equivalent relative motion. In Fluent this can be modeled by employing a moving-wall boundary condition at the base surface. This is implemented by adding a translating velocity to the stationary no-slip wall boundary condition (Fluent 6.3). In the current simulation a translation velocity of  $V_T = 1.07$  m/s is added to the base surface along the positive x-direction (This corresponds to vortex translation in the negative x-direction relative to the ground with a velocity of  $V_T = 1.07$  m/s). Applying the tentative velocity scaling of Hangan and Kim (2008) for Ward-type TVC and real-scale tornado, this corresponds to a real-scale translation velocity of 14 m/s approximately. Tornadoes are generally found to have translation velocities of about 10-20 m/s, so the translation speed considered here is in the appropriate range. Based on a scoping study carried out using k- $\epsilon$  model (details not reported here), the effects seen with this value would be sufficiently representative over the full range of translation velocities of interest. All other boundary conditions are the same as those used in the simulation of stationary vortex given in section 2.2.1 (refer Table 2.1a).

The simulations with translation effects were performed for four swirl ratios  $S = 0.28, 0.5, 1.0, 2.0$ . The results are compared with those of cases corresponding to LES simulations of stationary vortices (i.e.  $V_T = 0$ ).

### **3.2.2 Results and Discussion:**

A key finding from the study is that the introduction of translation to the vortex flow has opposite effects for low swirl ratios ( $S = 0.28$  and  $S = 0.5$ ) and high swirl ratios ( $S = 1.0$  and  $S = 2.0$ ): at low swirl ratios it adversely affects the formation of laminar end wall

vortex and the mean velocities are reduced compared to the stationary vortex. At high swirl ratios the translation causes local vortex intensification and the mean velocities are higher compared to the stationary vortex. More specific details are presented below.

### **3.2.2.1 Low swirl ratio:**

Figures 3.1a and 3.1b show the contour plots of the velocity magnitude in the XZ vertical plane for the translating vortices with swirl ratios  $S = 0.28$  and  $S = 0.5$  respectively. Translation is from the right to left in these figures. The figures show a slight tilt in the vortex near the base. Figures 3.2a and 3.2b, which compare the normalized mean tangential velocity along the radial distance for stationary (T0) and translating (T1.07) vortices, show a substantial reduction in tangential velocities for the translating vortices. The percentage reduction in the tangential velocity is higher for the  $S = 0.28$  case compared to the  $S = 0.5$  case. Also note the shift in the centre of the translating vortex to the right of the stationary vortex. The base surface pressure deficit for the translating vortices (shown in Figures 3.3a and 3.3b) is also less compared to the stationary vortices for these swirl ratios. The prominent tilt towards the right in the base pressure deficit for  $S = 0.5$  is similar to the tilt seen in real tornado pressure deficit measurements (refer Figure 12 of Ward 1972).

The reduction in tangential velocity and surface pressure deficit suggests that at low swirl ratios the translation produces an effect similar to reducing the swirl ratio of the vortex. Fiedler and Rotunno (1986) suggest that at low swirl ratios the supercritical flow in the laminar core (i.e. below VBD height) is responsible for the high velocities observed near the ground for a stationary vortex. Following that suggestion, one may explain the reduction in velocities as being sequel to a disruption of the laminar flow due to translation.

### 3.2.2.2 High swirl ratio:

Figures 3.1c and 3.1d show the contour plots of the velocity magnitude in the XZ vertical plane for the translating vortices with swirl ratios  $S = 1.0$  and  $S = 2.0$  respectively. They show that the tilt in the vortex near the base is less compared to the low swirl ratio vortices. The translation of the vortex has resulted in increased tangential velocity (Figures 3.2c and 3.2d) and base surface pressure deficit (Figures 3.3c and 3.3d).

Multiple vortices are observed at swirl ratios  $S = 1.0$  and  $S = 2.0$ . Unlike the stationary vortex where the multiple vortices occur all around the main vortex (Figures 2.20 and 2.21), for the translating vortex the multiple vortices are concentrated towards the leading side of the vortex. Figures 3.4 and 3.5 show the time averaged velocity magnitude, instantaneous velocity magnitude, instantaneous tangential velocity at height  $Z/R_0 = 0.02$  from the base for translating vortices with swirl ratios  $S = 1.0$  and  $S = 2.0$ , respectively. The instantaneous velocity contours show secondary vortices at the leading side of the translation. The turbulence characteristics for the translating vortex for  $S = 2.0$  (Figure 3.6) show the velocity fluctuation to be again concentrated at the leading side of the vortex. This can be attributed to the more intense shear at the front side of the translating vortex and can be a possible reason for the concentration of multiple vortices on this side.

### 3.3 Surface Roughness Effects:

In Fluent 6.3 surface roughness can be modeled as equivalent sand grain roughness or by physical modeling of roughness element (blocks). Both methods were attempted; in the first model roughness is introduced in the base as an equivalent sand grain roughness as discussed in Blocken et al. (2007) and in the second model blocks are modeled in the base surface based on the experimental work of Rostek and Snow (1985). The detailed discussions of both the simulations are given below.

### 3.3.1 Equivalent sand grain roughness model:

Roughness effects are introduced in CFD codes by modifying the wall function which is otherwise based on the universal near-wall velocity distribution (log law). In Fluent6.3, the modified wall function is given by

$$\frac{U_p u^*}{\tau_w / \rho} = \frac{1}{\kappa} \ln \left( E \frac{u^* y_p}{\nu} \right) - \Delta B \quad (3.1)$$

Where  $U_p$  and  $y_p$  are the velocity and height at the centre point  $P$  of the wall adjacent cell.  $E$  is an empirical constant for the smooth wall with a value 9.793,  $\tau_w$  is the wall shear stress,  $\rho$  is the fluid density and  $u^*$  the wall friction velocity defined as

$$u^* = C_\mu^{1/4} k_p^{1/2} \quad (3.2)$$

In the above equation,  $k_p$  denotes the turbulent kinetic energy in the wall adjacent cell centre point  $P$  and  $C_\mu$  is a constant with default value 0.09.

The basis for the modification of the wall function (Equation 3.1) comes from the experiments of Nikuradse (1933) on roughness effects on flow in pipes roughened with sand grains. He showed that the mean velocity distribution near a rough wall is parallel to the log law distribution, i.e. with the same slope ( $1/\kappa$ ) but different intercept ( $\Delta B$ ). In Fluent 6.3, the roughness function ( $\Delta B$ ) is defined as a function of dimensionless sand grain roughness height  $K_s^+$ .

$$K_s^+ = u^* K_s / \nu \quad (3.3)$$

Where  $K_s$  is the equivalent sand grain roughness height. Depending on the value of  $K_s^+$ , the roughness is classified into three regimes: aerodynamically smooth

( $K_s^+ < 2.25$ ), transitional ( $2.25 \leq K_s^+ < 90$ ) and fully rough ( $K_s^+ > 90$ ). The formula for  $\Delta B$  depends on the roughness regime and is given by Cebeci and Bradshaw (1977). The tornadic flow over rough terrain falls in the fully rough regime, and the formula corresponding to this regime is the following.

$$\Delta B = \frac{1}{\kappa} \ln(1 + C_s K_s^+) \quad (3.4)$$

$C_s$  is the roughness constant with a range of 0-1. In Fluent6.3 the roughness is introduced by specifying the values for the sand grain roughness height  $K_s$  and the roughness constant  $C_s$  in the wall boundary condition.

As Fluent introduces roughness as sand-grain roughness height, a relationship between the aerodynamic roughness lengths  $y_0$  and the equivalent sand-grain roughness heights  $K_s$  is needed to numerically simulate the effect of surface roughness in tornadic flow. Based on the first order continuity fitting of the atmospheric boundary layer (ABL) log law and the modified wall-function log law (Equation 3.1) at height  $y_p$ , Cebeci and Bradshaw (1977) arrived at the relationship:

$$K_s = \frac{9.793}{C_s} y_0 \quad (3.5)$$

For a default value of  $C_s = 0.5$ , the Equation 3.5 simplifies to  $K_s \approx 20y_0$ . This equivalent sand-grain roughness is used in this chapter. However, implementing roughness as equivalent sand-grain roughness creates a limitation that needs to be considered. The height of the centre point P of the wall-adjacent cell to the ground surface  $y_p$  needs to be larger than the physical roughness height  $K_s$  (i.e.  $y_p > K_s$ ). For modeling roughness in a city-centre where the  $y_0$  value is around 2 m, the  $K_s$  is around 40 m and the first cell height has to be greater than twice the  $K_s$  at 80 m. In tornadic flow

where the velocity profile for a height of 100 m is studied, this is not acceptable, so this method can only be applied to study low roughness terrains with smaller  $y_0$ , corresponding to open country, forested and thinly populated suburban terrains.

### 3.3.1.1 Numerical setup:

Hangan and Kim (2008) matched a Doppler radar data for real scale tornado with a CFD simulation of a laboratory scale tornado with a cylindrical domain of radius 0.6m and height 0.6 m. By comparing the highest wind speed (and the height at which the highest wind speed occurs) in the CFD model and full scale data they proposed a length scale of 3700 and velocity scale of 13 between the CFD model and the real scale tornado.

A full scale tornado simulation (CFD model scaled up with the length and velocity scale) is computationally very expensive as the number of grid points required to maintain the non-dimensional wall unit  $y^+$  between 30 and 500 is very high. On the other hand in a laboratory scale tornado, when the aerodynamic roughness lengths  $y_0$  is scaled down using the above length scale and introduced as equivalent sand grain roughness height, the wall roughness falls in the aerodynamically smooth regime. In the current simulations an optimal domain of  $1/20^{\text{th}}$  the scale of full scale tornado was chosen so that the wall roughness falls in the fully rough regime and the non-dimensional wall unit  $y^+$  is maintained between 30 and 500 making it computationally less expensive. The cylindrical domain used in the current simulations is as shown in Figure 3.7 with radius  $R_0$  equal to 112.68 m and height  $H_0$  equal to 112.68 m.

Fluent6.3 software is used for the finite volume analysis and steady state Reynolds Averaged Navier-Stokes (RANS) equations are solved on structured grids. The second order standard KE turbulence model with SIMPLEC pressure-velocity coupling is used.

The boundary conditions are as shown in Figure 3.7. The velocity inlet boundary condition is specified on the cylindrical surface, using the radial and axial velocity

profiles shown in Equations 3.6 and 3.7, along with the turbulent kinetic energy  $k$  and dissipation rate  $\varepsilon$  profiles for ABL modeled by Richards and Hoxey (1993) (Equations 3.8 and 3.9).

$$U(z) = U_h * (z/z_h)^{1/7} \quad (3.6)$$

$$V(z) = 2 * S * U(z) \quad (3.7)$$

$$k(z) = \frac{u_{ABL}^{*2}}{\sqrt{C_\mu}} \quad (3.8)$$

$$\varepsilon(z) = \frac{u_{ABL}^{*3}}{\kappa z} \quad (3.9)$$

Where  $U$  and  $V$  are radial and tangential velocities,  $U_h$  and  $z_h$  are the reference velocity and height (0.192 m/s, 4.695m),  $S$  is the swirl ratio,  $u_{ABL}^*$  is the ABL friction velocity and  $\kappa$  is the von Karman constant ( $\sim 0.41$ ). The bottom surface is defined as wall and standard wall function is used. For the zero roughness case (Y0),  $K_s = 0$  is used, and for the mild roughness case (Y1) with  $y_0 = 0.1\text{m}$ , scaled down with length-scale of  $1/20$  and converted to equivalent sand-grain roughness,  $K_s = 0.1\text{m}$  and  $C_s = 0.5$  is used. The top of the cylinder is defined as outflow boundary condition.

The initial structured grid was developed using the commercial software Gambit and subsequent grid adaptation was done using the ‘Region-adaptation’ feature in Fluent. The flow in the central near surface region is only of interest, so finer grids were adapted in the central near surface region. Following grid convergence, grids comprising upwards of 300,000 were used for simulations. Keeping in mind the limitation stated in the previous section, the wall adjacent cell centre point height is maintained at 0.125m and  $y^+$  is around 300. The numerical simulations were performed for swirl ratios ranging

from 0.1 to 2.0. Results for two select values of  $S$  are highlighted here for the purpose of discussion.

### 3.3.1.2 Results and Discussions:

For all the swirl ratios, the velocity vectors along the  $Z$ -axis (height) were compared for the smooth and rough-wall cases at different radial locations. For a given swirl ratio, the radial location where maximum tangential velocity ( $V_{\max}$ ) was observed in smooth-wall flow is termed  $R_{\max}$  and region between the centre and  $R_{\max}$  called the core. For the smallest swirl ratio  $S = 0.1$  (Figures 3.8 and 3.9), introducing roughness resulted in a mild increase in the radial and axial velocities at radial locations inside the core ( $R/R_0 < R_{\max}/R_0 \sim 0.05$ ), closer to the centre. As the swirl ratio increased, the increasing trend in the radial and axial velocities was more pronounced, as shown in Figures 3.11 and 3.12 for the highest swirl ratio  $S = 2.0$ . Moreover there is increase in radial velocity at radial locations even away from the core ( $R/R_0 > R_{\max}/R_0 \sim 0.23$ ). Also, the increase in axial velocity inside the core is very large. Lewellen and Sheng (1979), Dessens (1972) and Leslie (1977) have reported increase in radial and axial velocities and decrease in maximum tangential velocity. In the current simulations, the variation in tangential velocity does not completely match their results. While the introduction of roughness causes a decrease in tangential velocity at radial locations outside the core, there is an increase at locations inside the core. A possible explanation for this could be vortex stretching due to the increase in axial velocity inside the core. Two cases are illustrated in Figures 3.10 ( $S = 0.1$ ) and 3.13 ( $S = 2.0$ ) in support of this explanation. For swirl ratio 0.1; the increase in axial velocity (Figure 3.8) inside the core is less and a correspondingly small increase in tangential velocity (Figure 3.10) is observed. On the other hand for swirl ratio 2.0; there is a substantial increase in the axial velocity (Figure 3.11) inside the core and therefore greater increase in tangential velocity (Figure 3.13).

However, certain limitations related to numerical damping and the averaging nature of RANS model adopted should be recognized. Also to be noted is the inability of this steady state simulation to simulate multiple vortices at high swirl ratios ( $S \geq 1.0$ ). For



the domain size considered in the current simulation, adopting LES turbulence model would be computationally very expensive. This along with the fact that only low roughness case can be simulated using the current model, points to the need for a more robust model to be used. Hence, the physical modeling of roughness elements was attempted and is discussed in the sequel.

### **3.3.2 Physical modeling of roughness blocks:**

Experimental studies by Rostek and Snow (1985) have shown that for a Ward-Type TVC roughness introduced by mounting cylindrical wooden pegs (0.64 cm diameter and 0.64 cm height) on the base board of the TVC with a peg density of 190 pegs/m<sup>2</sup> produced an equivalent aerodynamic roughness length  $Y_0 = 1.9\text{m}$ . (City centre roughness). This configuration was therefore adapted in the current simulation.

#### **3.3.2.1 Numerical Setup:**

The computational software Fluent 6.3 was used for the simulations. Large Eddy Simulation (LES) was used for modeling turbulence and the details of the numerical schemes used are the same as those describes in section 2.2.1. The grid convergence test (2-3% variation in the maximum velocity near the base) indicated that a maximum of around 2,500,000 cells were sufficient for the simulations.

The domain described in section 2.2.1 is modified at the base surface by modeling conical pegs (1.28 cm diameter and 0.64 cm height) with 190 pegs/m<sup>2</sup> peg density to simulate the effects of high surface roughness of a city centre. Figure 3.14 shows the modified base surface of the domain with the roughness blocks (conical pegs). The boundary conditions are also the same as given in section 2.2.1 (refer Table 2.1a).

The simulations with roughness effects (denoted as Y2) were performed for four swirl ratios  $S = 0.28, 0.5, 1.0, 2.0$ . The results are compared with those of cases corresponding to LES simulations of vortices with smooth surface (denoted as Y0).

### 3.3.2.2 Results and discussion:

Figure 3.15 plots the time averaged maximum base pressure deficit coefficient as a function of swirl ratio for both smooth (Y0) and rough surface (Y2) for all the swirl ratios. A trend can be observed from the graph that the roughness causes an effect similar to reducing the swirl ratio. Figure 3.16 plots the maximum mean tangential velocity as function of swirl ratio for smooth and rough surface and the trend is similar. This is in agreement with past experimental and numerical results (Dessens 1972, Leslie 1977, Lewellen and Sheng 1979, Rostek and Snow 1985, and Church and Snow 1993) where it has been argued that the increase in roughness causes an increased frictional dissipation in the surface layer causing transition to a lower swirl configuration.

Besides the trend discussed above, the present study also leads to other interesting observations. The core radius along the height for the smooth and rough surface cases are compared for all the swirl ratios and shown in Figure 3.17. There is a significant increase in core radius for the lower swirl ratios ( $S = 0.28, 0.5$ ) and none too significant changes for the higher swirl ratios ( $S = 1.0$  and  $2.0$ ). Also the changes in pressure deficit (Figure 3.15) and tangential velocity (Figure 3.16) are more pronounced for low swirl ratios ( $S = 0.28, 0.5$ ) than for the high swirl ratios ( $S = 1.0, 2.0$ ). For low swirl ratios, the introduction of surface roughness disrupts the formation of laminar end wall vortex resulting in increased core radius and significant reduction in pressure deficit and tangential velocity (This reasoning is similar to the one given for explaining the effects of translation at low swirl ratios). At high swirl ratios it can be argued that the intense vortex stretching associated with the formation of multiple vortices counters the effects of surface roughness resulting in less pronounced changes in core radius, pressure deficit and tangential velocity.

### 3.4 Conclusion:

The effects of translation on a laboratory scale vortex using proper scaling for the translation velocity based on Hangan and Kim (2008) velocity-scale for Ward-type and

real-scale tornado were studied using LES simulations. The results show a key finding that the effect of translation is not uniform across the swirl ratios. For lower swirl ratios the translation reduces the maximum mean tangential velocity whereas for high swirl ratios it causes a slight increase in the maximum mean tangential velocity.

A preliminary study on the effects of surface roughness for low roughness case was performed by properly scaling the atmospheric roughness length for Ward-type TVC and using the equivalent sand-grain roughness option in Fluent. Limitations in Fluent software, limits this study to only low roughness case and emphasizes the need for a more robust method. Subsequent studies using physical modeling of roughness elements were done and the results are closely in line with the past experimental studies. The adoption of proper scaling has not led to any significant differences compared to past studies. The introduction of roughness reduces the mean tangential velocity at all swirl ratios in other words the roughness causes an effect similar to reducing the swirl ratio.

### **3.5 Reference:**

Blocken, B., Stathopoulos, T., and Carmeliet, J., 2007. CFD simulation of the atmospheric boundary layer: wall function problems. *Atmospheric Environment* 41, 238-252.

Cebeci, T., and Bradshaw, P., 1997. *Momentum transfer in Boundary layers*. Hemisphere publishing Corporation, New York.

Church, C. R., Snow, J. T., Baker, G. L., and Agee, E. M., 1979. Characteristics of tornado like vortices as a function of swirl ratio: A laboratory investigation. *Journal of the Atmospheric Sciences* 36, 1755-1776.

Church, C. R., and Snow, J. T., 1993. Laboratory models of tornadoes, *The Tornado: Its Structure, Dynamics, Prediction, and Hazards*, C., Church et al., Eds., American Geophysics Union, 277-295.

- Dessens, Jr., J., 1972. Influence of ground roughness on tornadoes: A laboratory simulation. *Journal of Applied Meteorology* 11, 72-75.
- Diamond, C. J., and Wilkins, E. M., 1984. Translation effects on simulated tornadoes. *Journal of the Atmospheric Sciences* 41, 2574-2580.
- Fiedler, B. H., and Rotunno, R., 1986. A theory for the maximum wind speeds in tornado-like vortices. *Journal of the Atmospheric Sciences* 43, 2328-2340.
- Hangan, H., and Kim, J. D., 2008. Swirl ratio effects on tornado vortices in relation to the Fujita Scale. *Wind and Structures* 11(4), 291-302.
- Kuai, L., Haan, F. L., Gallus, W. A., and Sarkar, P. P., 2008. CFD simulations of the flow field of a laboratory simulated tornado for parameter sensitivity studies and comparison with field measurements. *Wind and Structures* 11(2), 75-96.
- Leslie, F. W., 1977. Surface roughness effects on suction vortex formation: A laboratory simulation. *Journal of the Atmospheric Sciences* 34, 1022-1027.
- Lewellen, W. S., and Sheng, Y. P., 1979. Influence of surface conditions on tornado wind distribution. Preprints, 11th Conf. on Sev. Loc. Storms (Kansas City, MO), AMS, Boston, MA, 375-378.
- Lewellen, W. S., 1993. Tornado vortex theory. *The Tornado: Its Structure, Dynamics, Prediction, and Hazards*, C. Church et al., Eds., American Geophysics Union, 19-40.
- Lewellen, W. S., Lewellen, D. C., Sykes, R. I., 1997. Large-eddy simulation of a tornado's interaction with the surface. *Journal of the Atmospheric Sciences* 54, 581-605.

Nikuradse, J., 1933. Stromungsgesetze in rauhen Rohren, Forschung Arb. Ing.-Wes. No. 361.

Richards, P. J., and Hoxey, R. P., 1993. Appropriate boundary conditions for computational wind engineering models using the  $k\varepsilon$  turbulence model. Journal of wind engineering and industrial aerodynamics 46-47, 145-153.

Rostek, W. F., and Snow, J. T., 1985. Surface roughness effects on tornado like vortices, in preprints, 14th Conference on Severe Local Storms, AMS, Boston, MA, 252-255.

Rotunno, R., 1977. Numerical simulation of a laboratory vortex. Journal of the Atmospheric Sciences 34, 1942-1956, 1977.

Ward, N. B., 1972. The exploration of certain features of tornado dynamics using a laboratory model. Journal of the Atmospheric Sciences 29, 1194-1204.

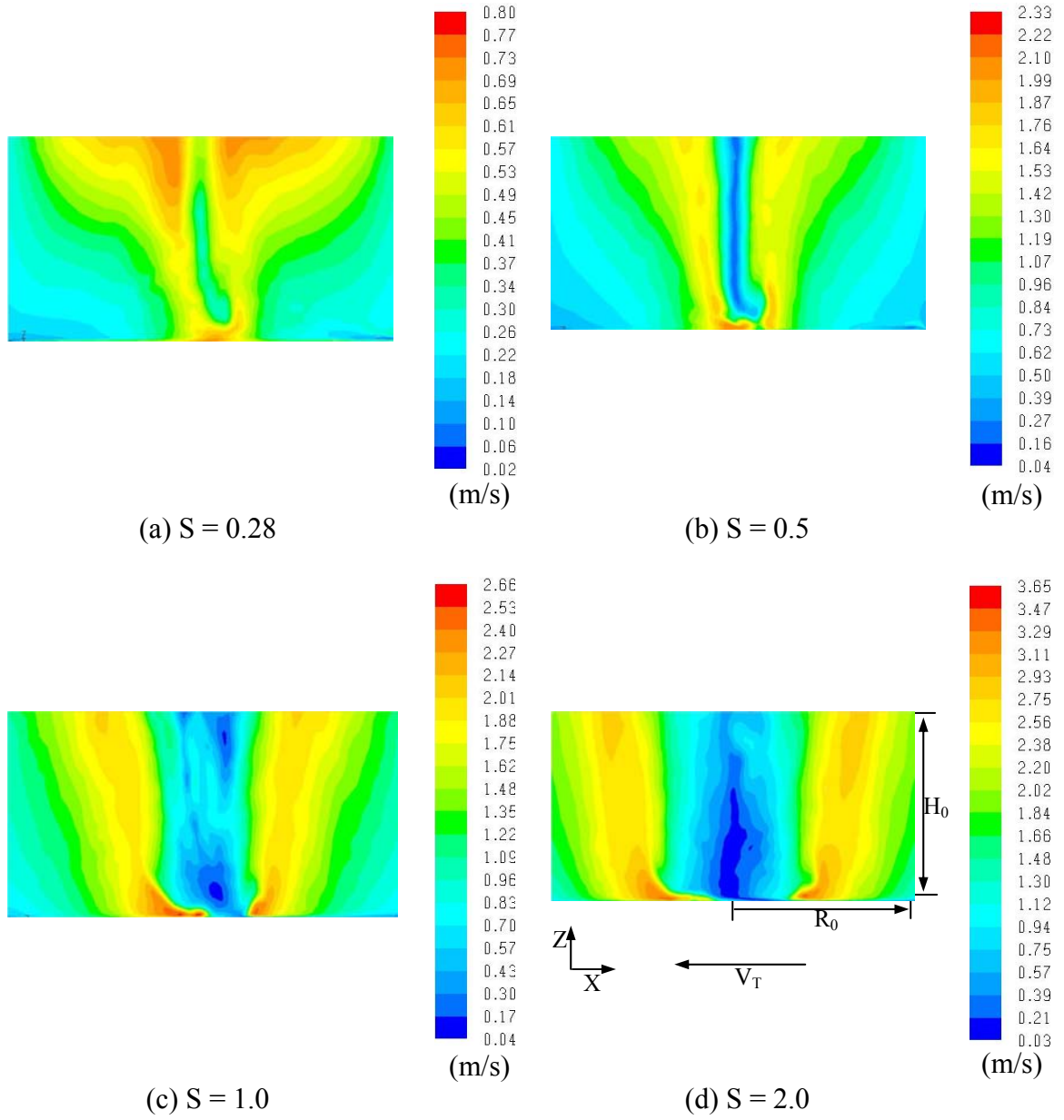


Figure 3.1: Contour plots of velocity magnitude in the XZ plane for tornadic flow with translation. ( $V_T = 1.07$  m/s)

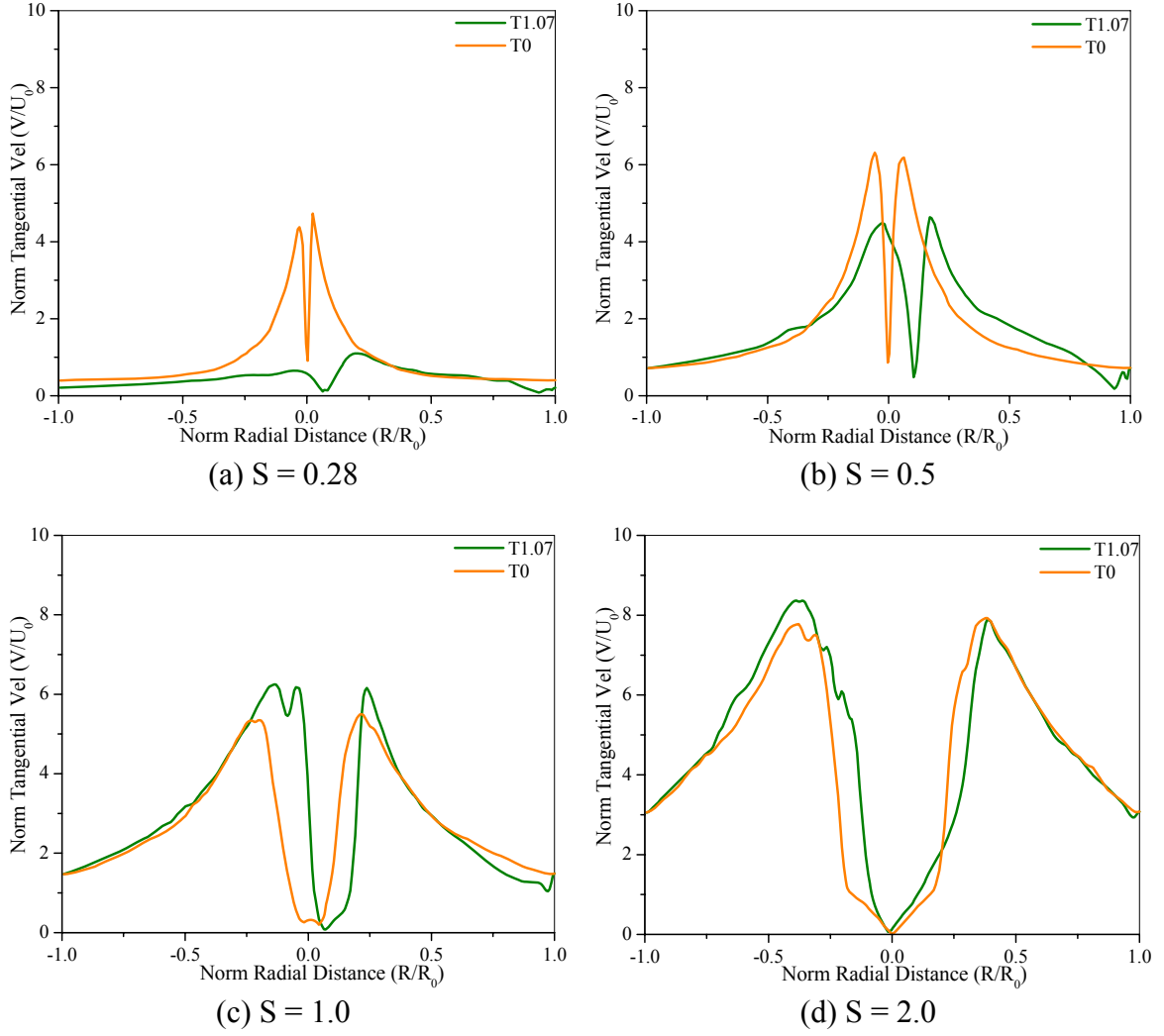


Figure 3.2: Normalized tangential velocity along the normalized radial distance for various swirl ratios of stationary (T0) and translating (T2) tornado-like vortices at height  $Z/R_0 = 0.02$ .

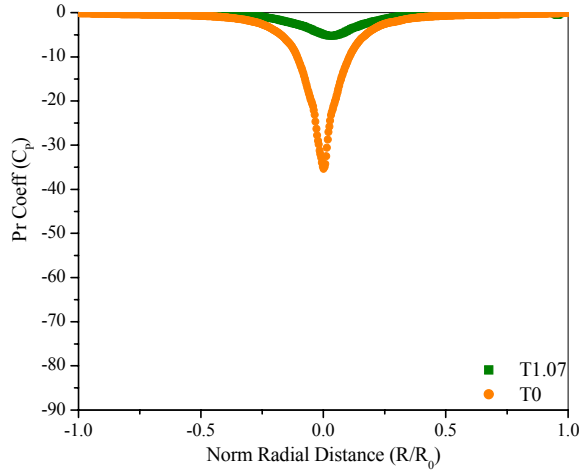
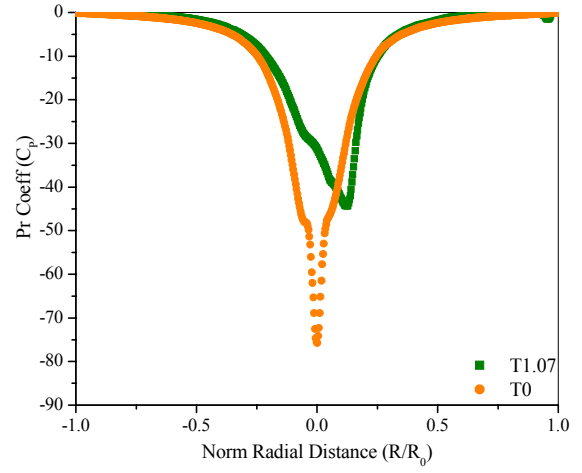
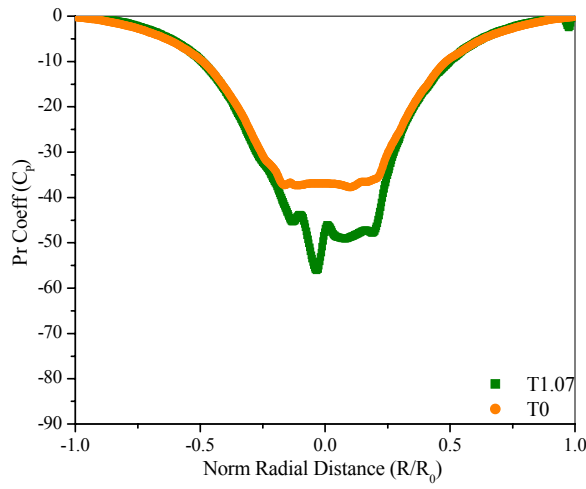
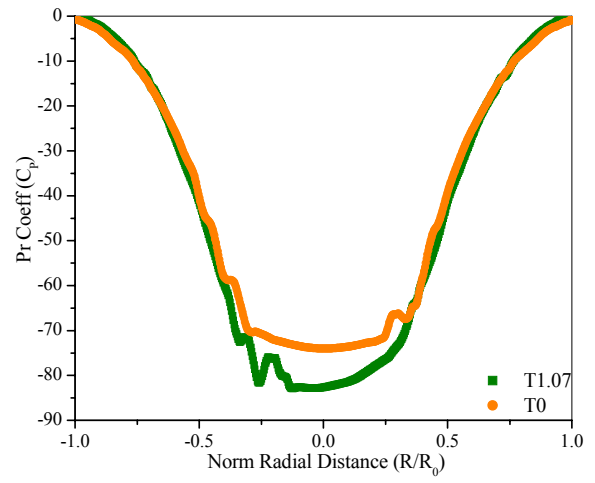
(a)  $S = 0.28$ (b)  $S = 0.5$ (c)  $S = 1.0$ (d)  $S = 2.0$ 

Figure 3.3: Base surface pressure coefficients for various swirl ratios of stationary (T0) and translating (T2) tornado-like vortices.



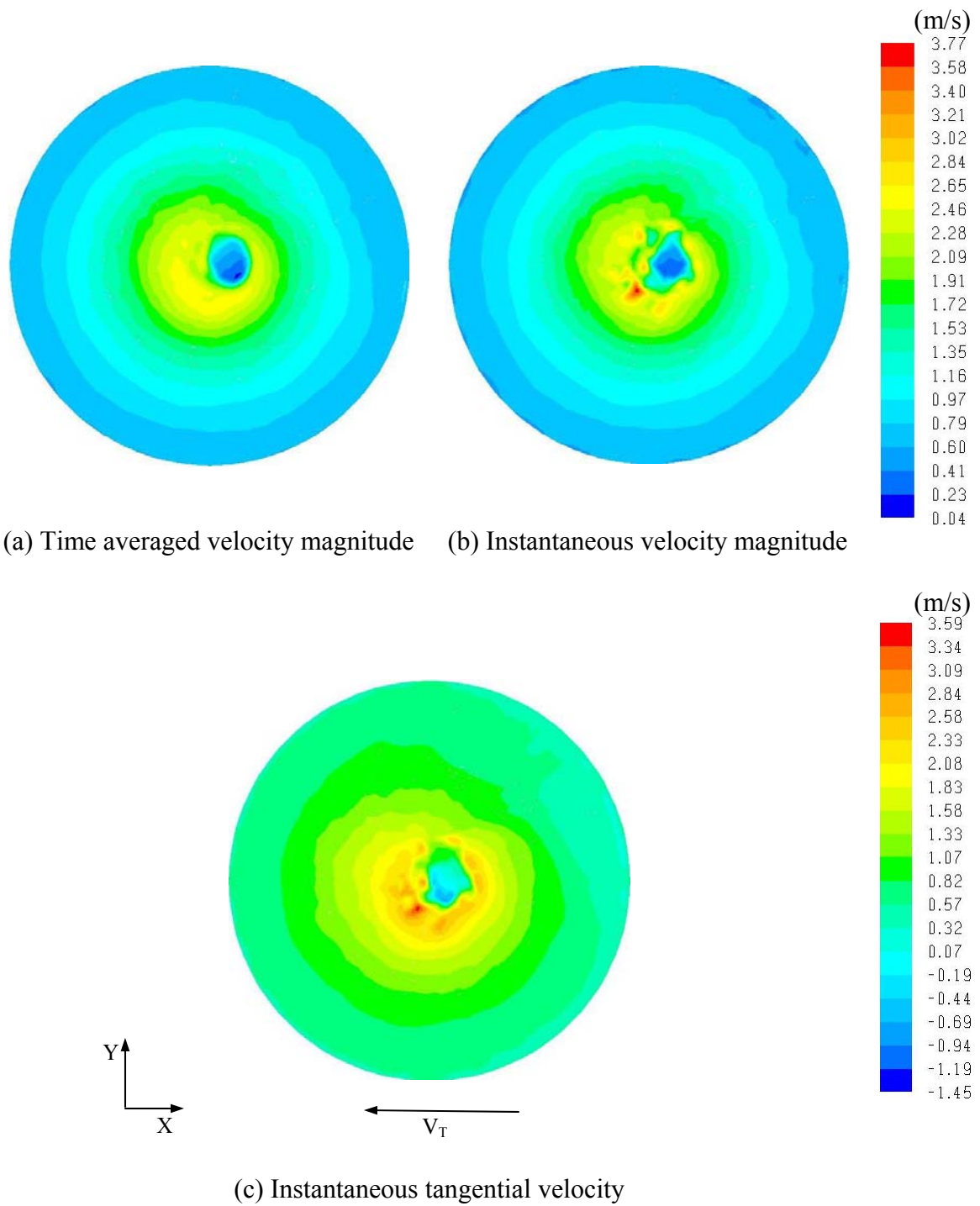


Figure 3.4: LES velocity contours for  $S = 1.0$  with translation velocity  $V_T = 1.07$  m/s, at height  $Z/R_0 = 0.02$

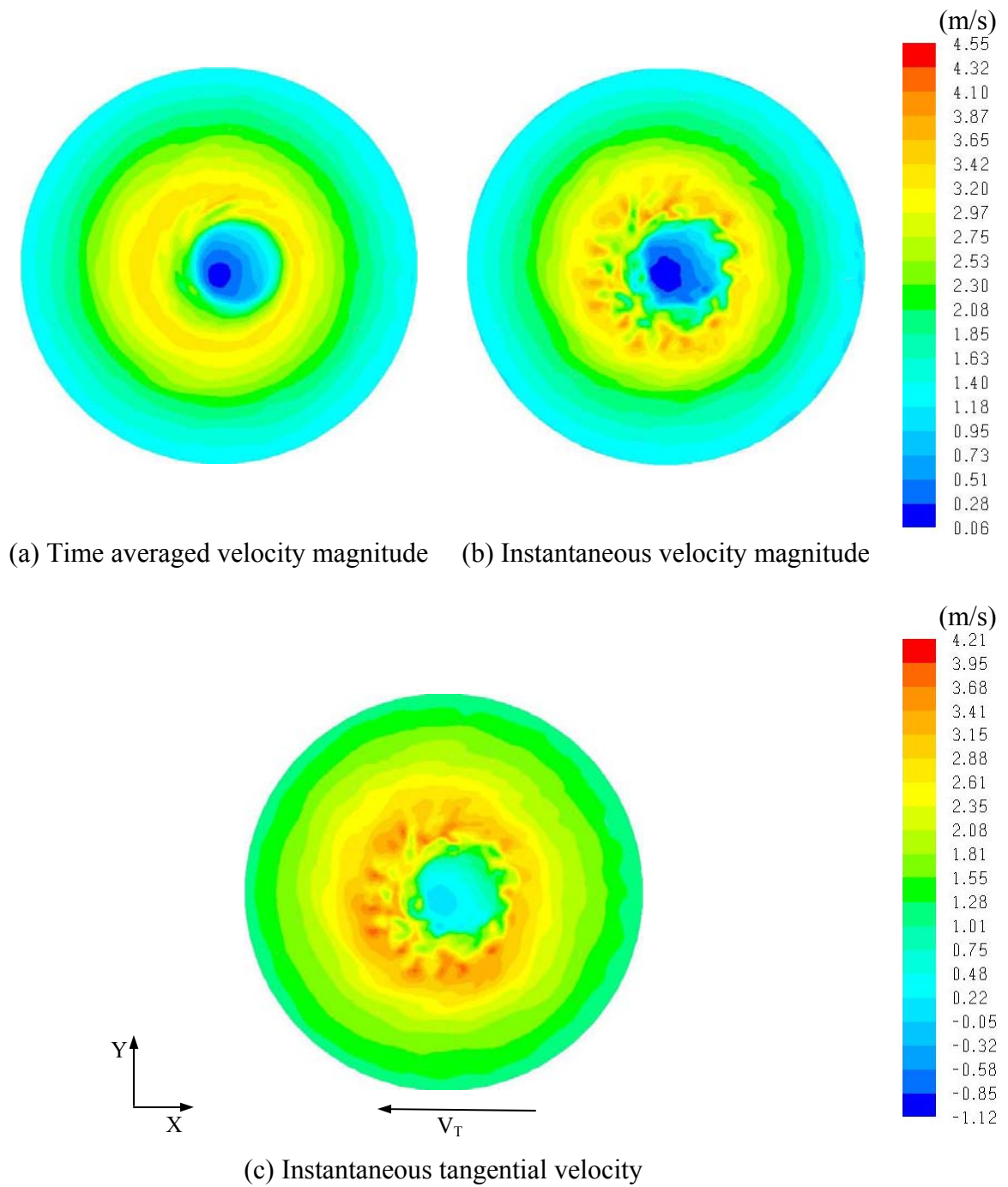


Figure 3.5: LES velocity contours for  $S = 2.0$  with translation velocity  $V_T = 1.07$  m/s, at height  $Z/R_0 = 0.02$

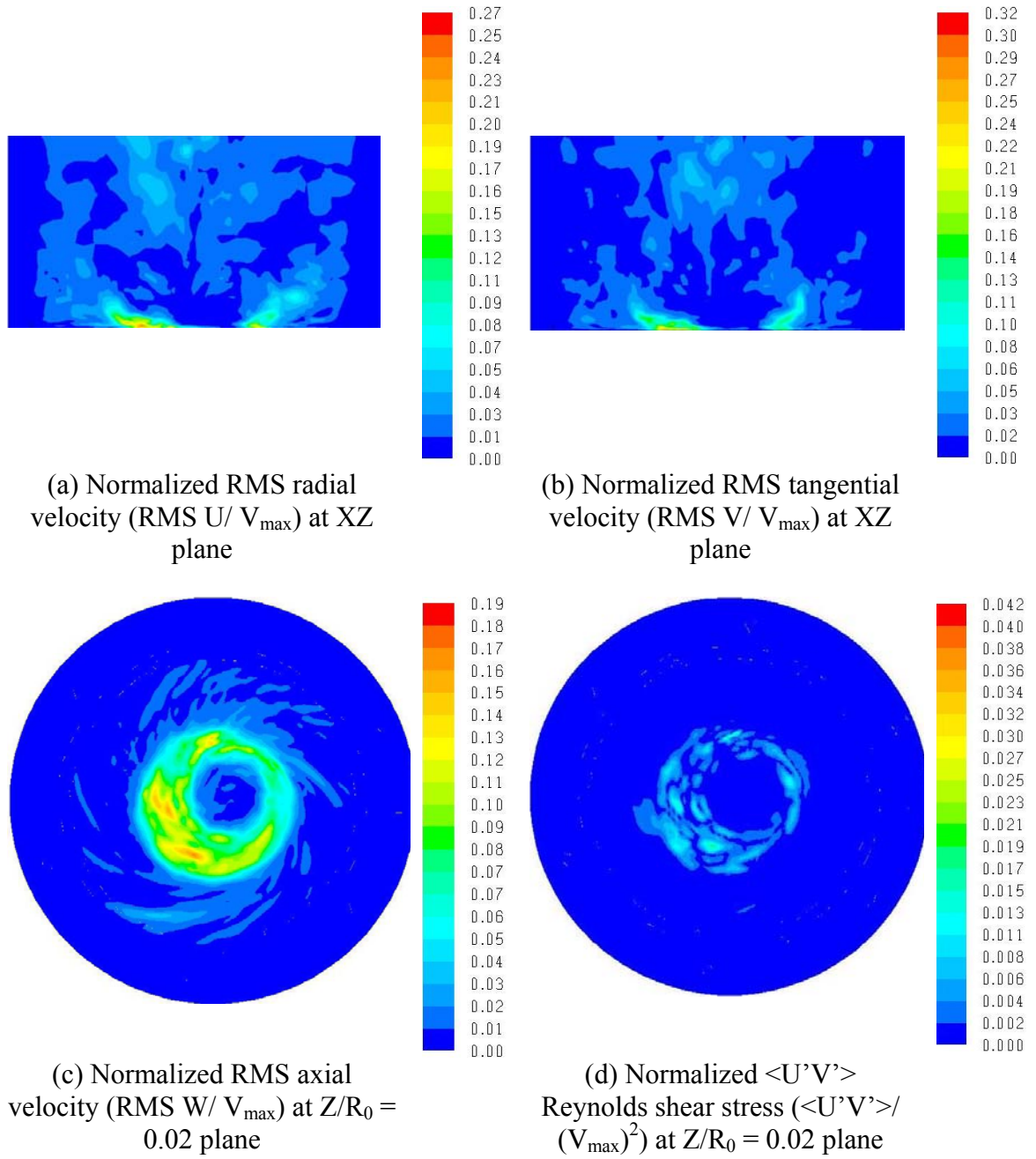


Figure 3.6: Turbulence characteristics for  $S = 2.0$  with translation  $V_T = 1.07$  m/s

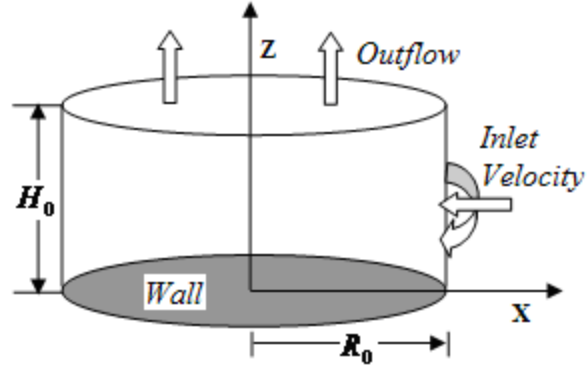


Figure 3.7: Computational domain for simulating the effects of surface roughness using equivalent sand grain roughness model.

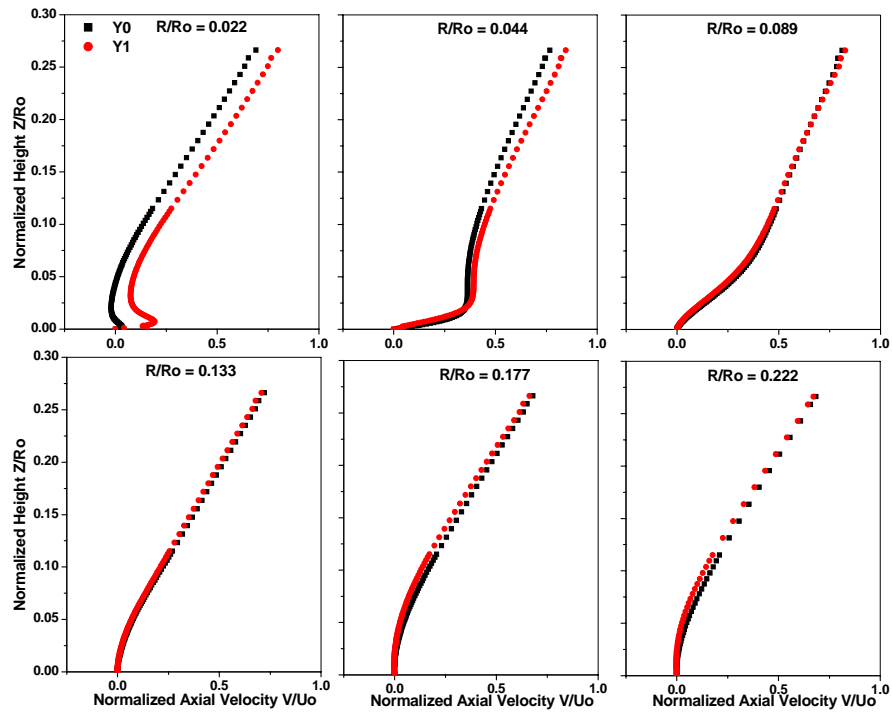


Figure 3.8: Normalized axial velocity along the normalized height for different radial location for swirl ratio 0.1

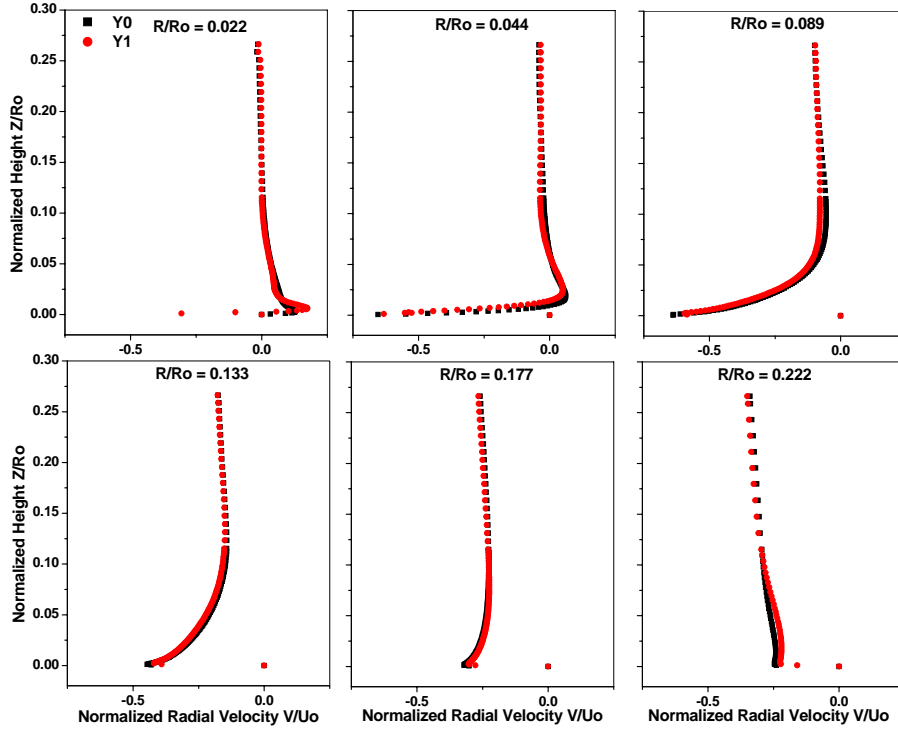


Figure 3.9: Normalized radial velocity along the normalized height for different radial location for swirl ratio 0.1

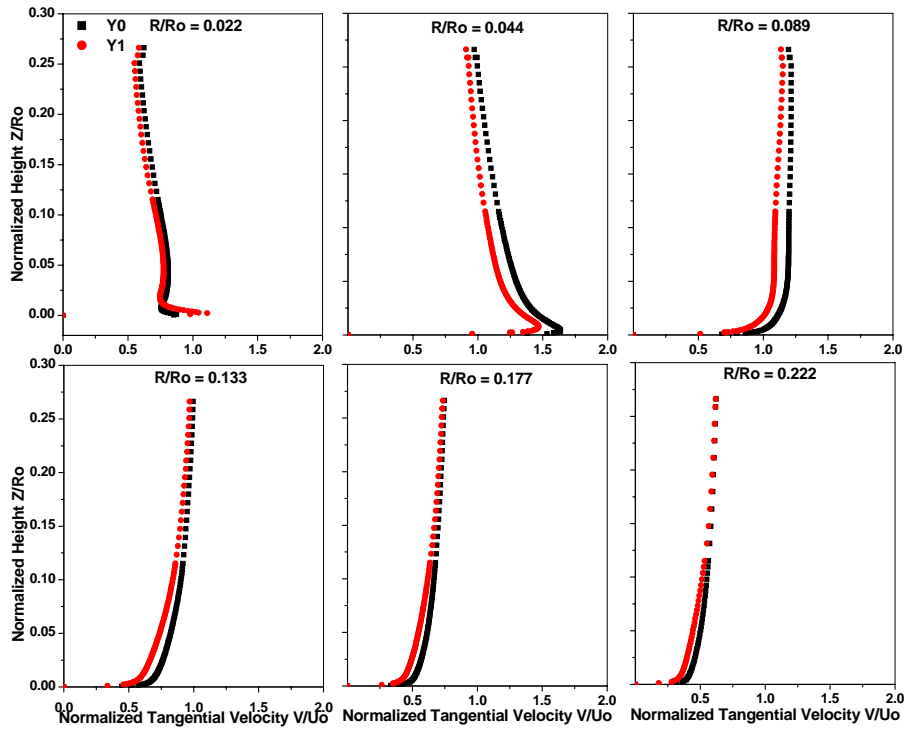


Figure 3.10: Normalized tangential velocity along the normalized height for different radial location for swirl ratio 0.1

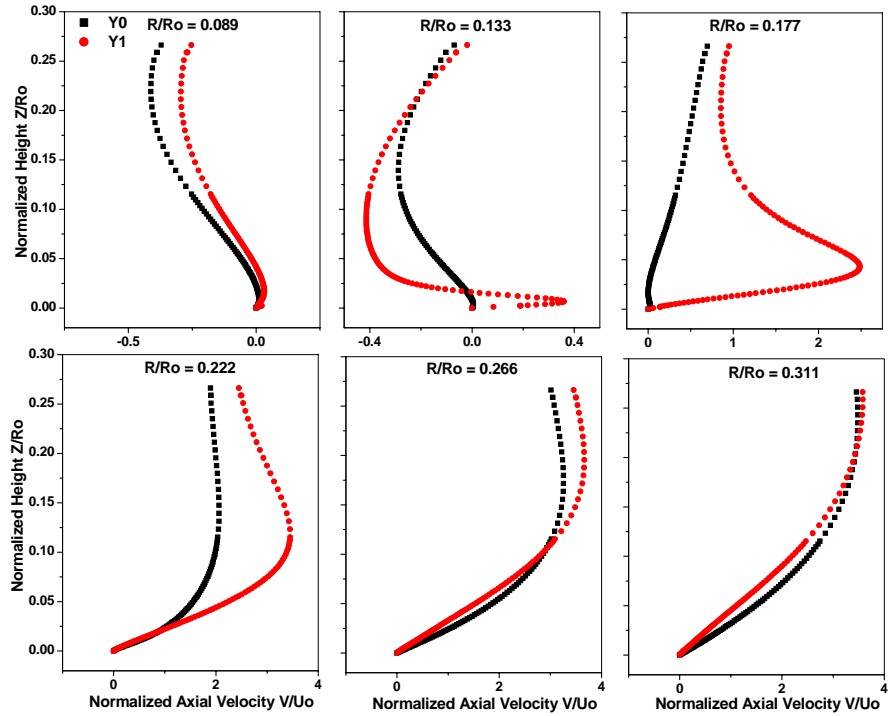


Figure 3.11: Normalized axial velocity along the normalized height for different radial location for swirl ratio 2.0

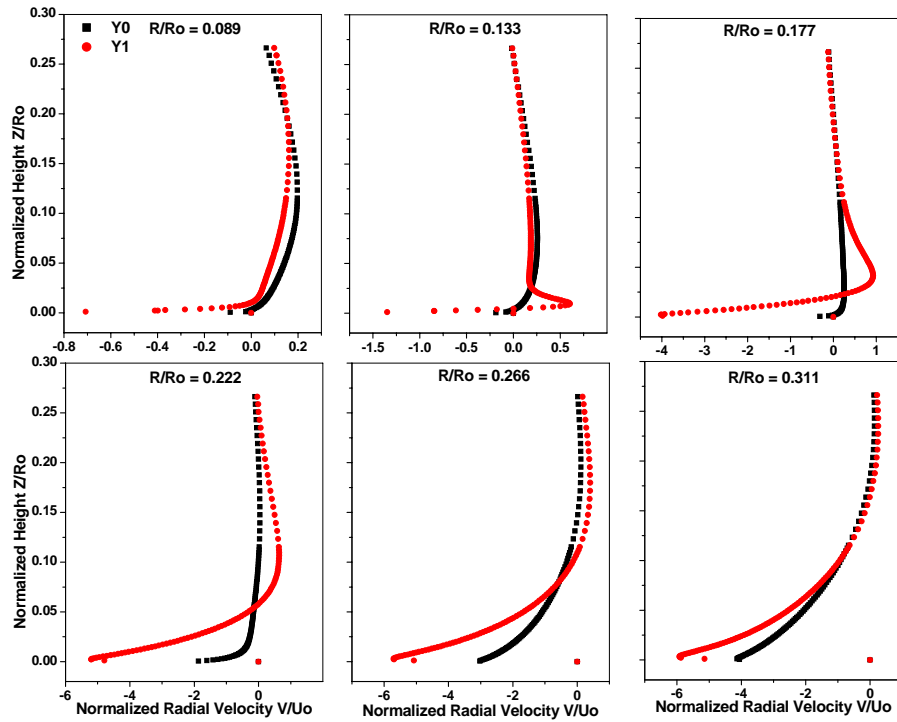


Figure 3.12: Normalized radial velocity along the normalized height for different radial location for swirl ratio 2.0

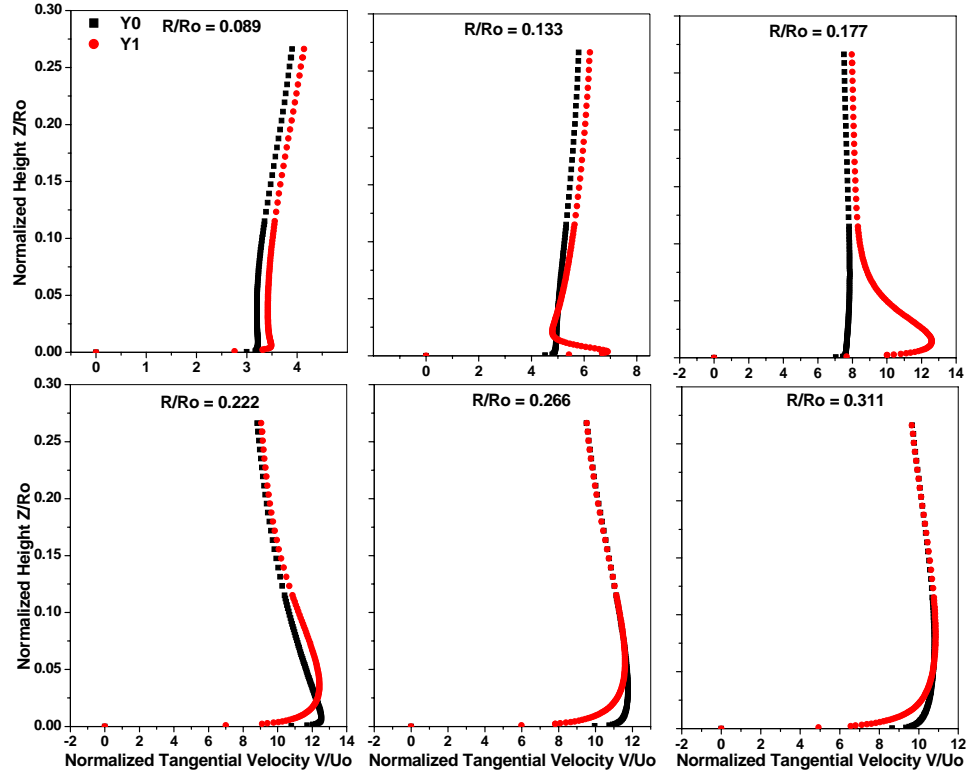


Figure 3.13: Normalized tangential velocity along the normalized height for different radial location for swirl ratio 2.0

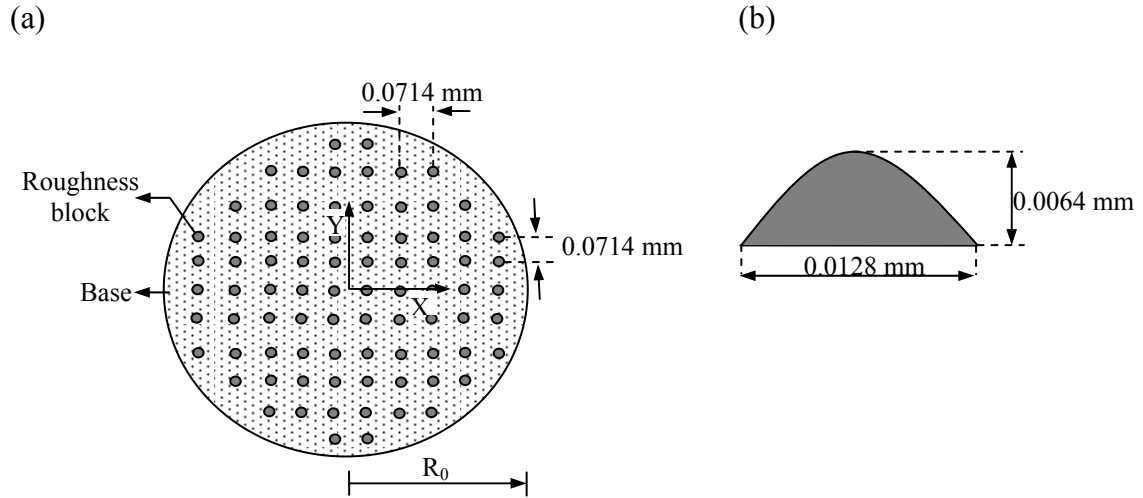


Figure 3.14: Sketch showing the physically modeled rough surface. (a) The base wall of the domain with the roughness blocks. (b) The roughness block.

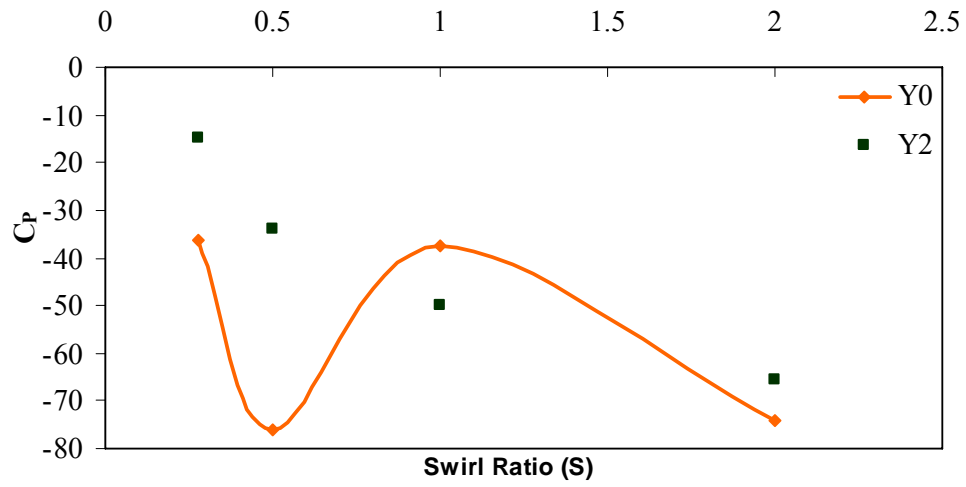


Figure 3.15: Maximum time-averaged central base pressure deficit vs. swirl ratio smooth (Y0) and rough surface (Y2).

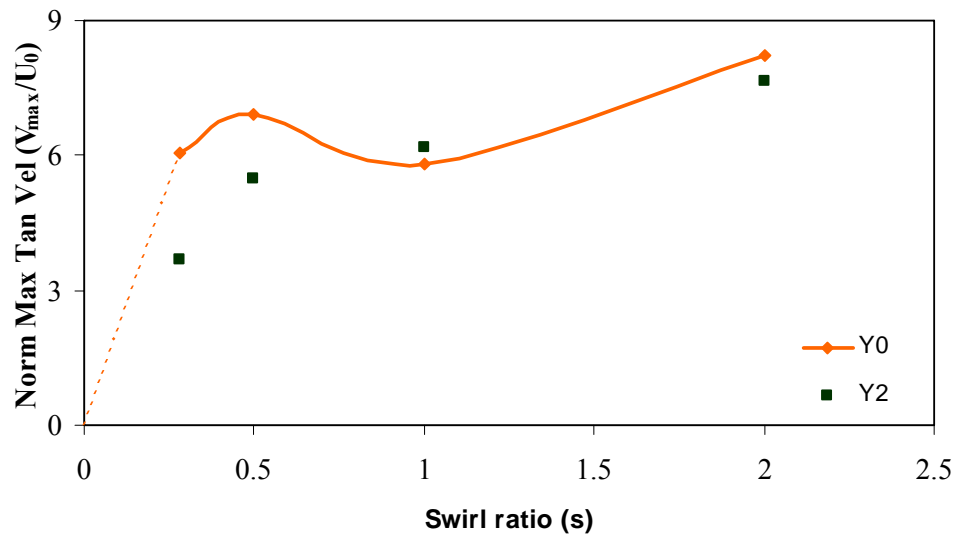


Figure 3.16: Maximum time-averaged tangential velocity vs. swirl ratio for smooth (Y0) and rough surface (Y2).



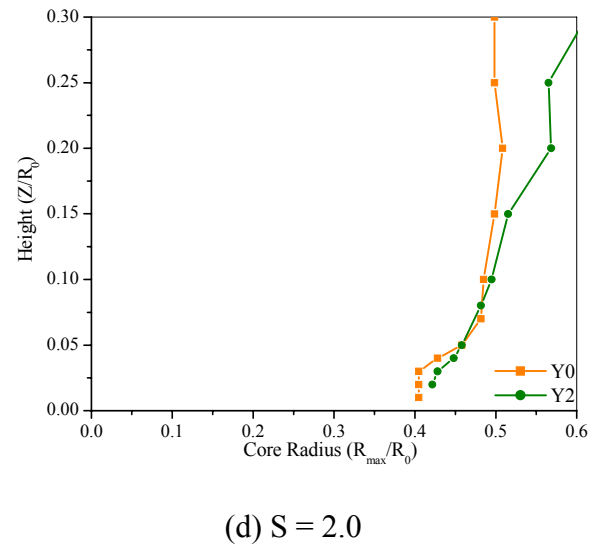
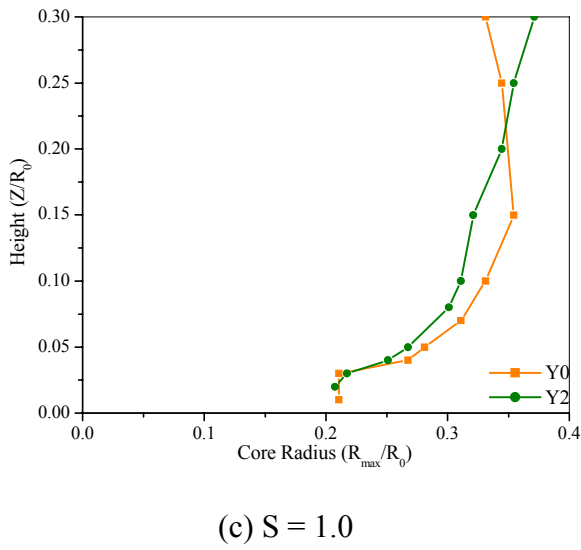
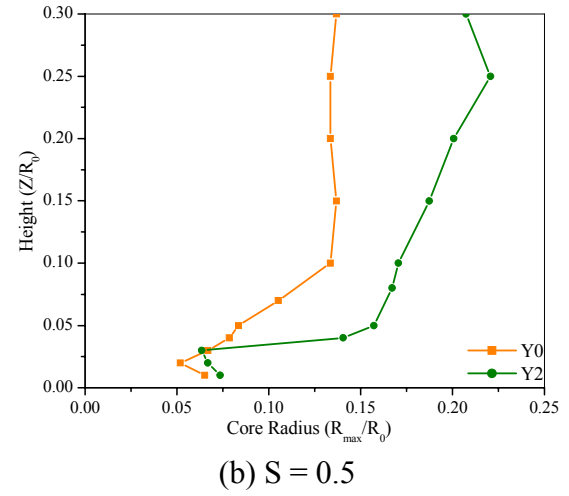
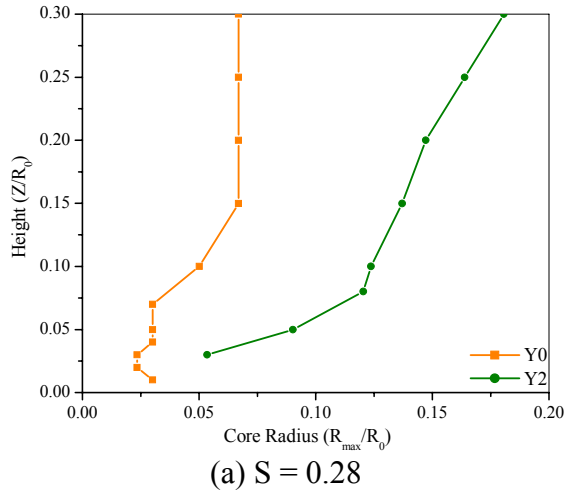


Figure 3.17: Core radius along the height for various swirl ratios of smooth (Y0) and rough (Y2) surface tornadoes.

## Chapter 4: Numerical Simulation of WinDEEE Dome Facility

### 4.1 Introduction:

The Wind Engineering, Energy and Environment (WinDEEE) Dome is a novel wind research facility planned to be built at the University of Western Ontario, funded by the Canadian Foundation for Innovation (CFI) and the Ontario Research Fund (ORF). The WinDEEE concept was developed by Dr Horia Hangan and forms the basis of the funded CFI proposal. During the conceptual phase both in-house (UWO) and consultant (AIOLOS) CFD simulations were employed to optimize and solidify the implied concept. This chapter shows a combination of CFD simulations developed both in house (UWO) through this thesis and collaboration with the AIOLOS consultant. WinDEEE is meant for wind testing of large scale models of buildings and structures in complex terrain under sheared/straight and axi-symmetric flows (tornado and downburst-like winds). It also allows for testing of complete wind or solar farms at large scales and high resolution.

The Downburst and Tornado mean velocity profiles vary significantly with synoptic wind mean velocity profiles, with the peak velocity occurring less than 50 m from the surface for the former flows (Kim and Hangan, 2007, Lewellen et al., 1997). Conventional straight flow wind tunnels cannot produce those wind profiles, only specialized wind tunnels like Tornado Vortex Chambers (Ward, 1972, Haan et al., 2007) and Downburst simulators (Chay and Letchford, 2002, Wood et al., 2001) can simulate their flow pattern. The proposed WinDEEE Dome can produce tornado-like, downburst-like and synoptic wind profile in a single chamber by modifying the inlet and outlet boundary conditions.

This chapter presents the numerical simulations conducted to assess the dome's capacity to generate the various wind profiles. In section 2, for a preliminary dome design it is demonstrated that tornado-like and downburst-like flows can be generated in the WinDEEE dome. Further design optimizations are presented in section 3 to improve the dome design and enable the straight-flow mode wind field. The primary objective of the

study is to assess the number, dimension and distribution of fans as well as their inlet wind speeds and vector angles to produce various flow patterns. Also, the wind fields simulated in the WindEEE dome are compared with available real scale and laboratory scale tornadoes and downbursts.

## **4.2 Preliminary Design:**

The preliminary WindEEE dome configuration consists of a hexagonal inner chamber with arrays of fans on all six walls and the ceiling surrounded by an outer, return air flow dome. The inner hexagonal test chamber has a diameter of  $D_{\text{Hex}} = 25$  m and a maximum base to roof height of  $H = 7$  m. All the side walls of the chamber have an uniformly spaced array of 8 columns by 2 rows of fans (0.5 m in diameter) and the roof has a closely packed hexagonal array of 19 fans (1m diameter). During the downburst mode of operation the roof fans acts as air inlet and the array on the side walls act as outlets. This is reversed for tornado simulation where the array on the side walls act as inlets and the roof fans act as outlets.

### **4.2.1 Numerical Setup:**

In the current simulations, the computational domain is limited to the inner chamber as shown in Figure 4.1. The array of fans in the roof is replaced by a  $D = 5$  m diameter circular opening (Roof opening) and the fans on the side walls are replaced by  $d = 0.5$  m diameter circular opening (Side wall opening). The preliminary boundary conditions for tornado and downburst simulations are detailed in Table 4.1.

The Computational Fluid Dynamics software, Fluent 6.3 was used for solving the steady-state Reynolds Averaged Navier-Stokes (RANS) equations. As this was a preliminary study, the shear-stress transport (SST) K-W model was used for modeling turbulence. The model effectively blends the robust and accurate formulation of the K-W model in the near wall region with the free-stream independence of the K-E model in the far field (Fluent 6.3, 2006). A brief description of the (SST) K-W model is presented in

Appendix A. An initial unstructured grid was developed using the software ‘Pointwise’. Grid convergence was performed and an unstructured grid of close to 2 million cells was deemed to provide grid convergence for both the tornado and downburst simulations. The wall  $Y^+$  was maintained in the range 30 to 300, corresponding to a standard wall function modeling (i.e. viscous sub-layer and buffer layers are not resolved) in the near-wall region based on the proposal of Launder and Spalding (1972). The segregated implicit solver, SIMPLEC pressure velocity coupling and second order discretization for pressure, momentum, turbulent kinetic energy and specific dissipation rate were used.

#### 4.2.2 Downburst:

Kim and Hangan (2007) show that laboratory simulations of downburst-like flow need to consider the following: (1) The maximum mean velocities for downburst occur at heights of less than 5% of the initial jet diameter  $D$ . In order to obtain at least a couple of measurement points in this region the jet diameter has to be 0.2 m or larger. (2) The height at which the maximum mean velocity is encountered decreases with increasing Reynolds number ( $Re$ ) and this dependency is more pronounced for  $Re < 200,000$ , so Reynolds numbers greater than 200,000 are preferred. (3) The distance between the jet and base surface  $H$  is not a critical parameter as long as it allows for the formation of the main vortex rings, which based on convective velocity argument, corresponds to  $H \geq D$ .

The following cases are considered in the current simulations.  $D = 1.75$  m,  $D = 3.5$  m (based on the availability of benchmarking data) and  $D = 5$  m (the maximum possible diameter). For all the cases, the inlet jet velocity  $V_{jet}$  is 20m/s and height  $H$  is 7m. The Reynolds number ( $Re$ ) is defined in Equation 4.1 below.

$$Re = V_{jet} D / \nu \quad (4.1)$$

Table 4.2 lists the  $H/D$  ratios and Reynolds numbers for the three cases. The selected parameter values are such that they meet the above requirements.

The current numerical results are compared with numerical result of Kim and Hangan (2007) for impinging jets corresponding to  $Re = 2,000,000$ ,  $H/D = 4$  and  $R/D = 1$  shown in Figure 4.2. The mean radial velocity profiles match well, the maximum mean velocity occurs within  $0.05D$  from the base and Reynolds number dependency is negligible as the  $Re > 200,000$ . Figure 4.3 compares the mean radial velocities at  $R/D$  between 1 and 2.5 for the current simulation with  $H/D = 4$ ,  $Re = 2,317,881$  and experimental results of Hangan and Xu (2005) for impinging jets with  $H/D = 4$  and  $Re = 27000$ . The matching with experiments is encouraging considering the fact that this is a preliminary K-W (SST) model simulation and the Reynolds numbers are different.

#### 4.2.3 Tornado:

Past studies show that the flow pattern of a tornado is chiefly influenced by the non-dimensional parameter swirl ratio (Davies-Jones, 1973, Church et al., 1979). For a Ward type laboratory Tornado Vortex Chamber (TVC), this ratio is defined as in Equation 4.2.

$$S = V_0 / 2AU_0 \quad (4.2)$$

Where  $U_0$  and  $V_0$  are the radial and tangential velocities at  $R_0$  and  $A$  is the aspect ratio which is equal to  $H_0/R_0$  (where  $R_0$  is the radius of updraft and  $H_0$  is the depth of inflow).

The classification of real scale tornadoes is done using the forensic Fujita scale based on the observed maximum wind speed. Hangan and Kim (2008) have tentatively related the swirl ratio with the Fujita scale by matching Doppler radar data for real scale tornado with CFD simulations of Ward-type laboratory scale tornado and inferred that F4 Fujita scale tornado approximately corresponds to a swirl ratio of  $S = 2.0$ . Whenever lab scale tornadoes are compared with real scale ones, this inferred equivalence serves as a useful basis.

In the current simulations attempts have been made to simulate an  $S = 2.0$  (F4 equivalent) tornado in the preliminary WindEEE dome configuration. Tornadoes can be

generated in the WindEEE dome by two methods namely; guide louver method and horizontal shear method as illustrated conceptually in Figure 4.4. In the first method, guide louvers are provided at the inlet fans in the side walls such that air enters at a constant speed ( $U_{Fan}$ ) at a select angle  $\theta$  with respect to the normal to the side wall. This helps achieve a constant normal and tangential velocity ( $U_{in}$ ,  $V_{in}$ ) at the inlet. In this method the swirl ratio is controlled by varying the speed of the fan ( $U_{Fan}$ ) and the angle  $\theta$ . In the horizontal shear method, the air entry is always normal to the side wall but the speed is varied uniformly from one end of the row of fans to the other end (say from  $V_{in-min}$  –  $V_{in-max}$ ) on each of the six side walls. Different swirl ratios are obtained by varying the fan velocity and the velocity gradient across the row of fans on each side wall.

Inlet configurations corresponding to both the guide louver method and the horizontal shear method are considered in the current simulations. Several inlet conditions (i.e.  $U_{in}$ ,  $V_{in}$  for guide louver method and  $V_{in-min}$  –  $V_{in-max}$  for horizontal shear method) of both methods were simulated and the conditions which produced a tornado with swirl ratio close to 2 by both methods were selected and the results of those corresponding cases are presented here.

In case 1, which corresponds to the guide louver type inlet, the constant normal and tangential velocities of the inlet air are  $U_{in} = 9.66$  m/s and  $V_{in} = 2.59$  m/s at all the side wall openings. This is equivalent to a fan velocity of  $U_{Fan} = 10$  m/s with guide louver angle  $\theta = 15^\circ$ . In case 2, which corresponds to the horizontal shear type inlet, the normal velocity of inlet air is varied from 0 – 20 m/s at each of the six sides. The swirl ratio as defined in Equation 4.2 for a Ward type TVC cannot be directly applied with WindEEE dome simulations. However, an appropriate swirl ratio can be obtained by choosing a cylindrical region within the WindEEE dome inner chamber that is similar to the convergence region of the Ward type TVC. This cylindrical domain is chosen such that at its boundary the tangential velocity is uniform along the height and the axial velocity is negligible along the height. The size of the cylindrical domain that meets this requirement for case 1 is  $R_0 = 7$  m and  $H_0 = 3.5$  m and for case 2 is  $R_0 = 8$  m and  $H_0 = 4$  m. The average radial and tangential velocity at  $R_0$  is used to calculate the swirl ratio and

an approximate swirl ratio of 2 was obtained for both cases. For such a swirl ratio, a two-celled tornado with multiple vortices is expected (Church et al., 1979) i.e. the tornado has an inner core with downdraft and an outer core with updraft surrounded by secondary vortices. Since the current preliminary simulation is based on K-W (SST) model it does not capture the multiple vortices, but generates a two-celled tornado as shown in Figure 4.5.

Figures 4.6 and 4.7 compare the plot of normalized tangential velocity as a function of normalized radial distance for cases 1 and 2 respectively with the normalized full scale tangential velocity data from a F4 Spencer, South Dakota tornado of May 30, 1998 (Sarkar, et al. 2005). Here, the tangential velocity is normalized with the maximum tangential velocity and radial distances are normalized with the radius at which the maximum tangential velocity occurs. The velocities are compared at various heights normalized with the height at which the maximum tangential velocity occurs. The plot shows that the tangential velocity along the radial direction varies as a in a Rankine vortex, which was also observed in section 2.2.3 for Ward-type TVC tornado-like flow simulations. The comparison shows an encouraging match and establishes that the current WindEEE dome configuration is able to generate an equivalent F4 tornado.

#### **4.3 Design optimization:**

The numerical simulations discussed above for the preliminary WindEEE dome configuration established the feasibility for generating tornado-like and downburst-like wind profiles in the facility. An array of 8 by 2 fans in the side walls combined with an array of roof fans of an equivalent diameter of 5 m were found to be adequate to produce satisfactory results. However, certain design modifications in the preliminary configuration are required to incorporate an additional feature in the WindEEE dome facility, namely, generating straight/sheared wind flow as in a conventional straight flow wind tunnel. Moreover, modifications in the configuration are called for to improve the characteristics of the downburst-like wind profiles. The preliminary design uses fans in the roof to produce a continuous impinging jet of air to simulate the downburst wind

profiles. In typical real life downbursts, a mass of cold and moist air descends suddenly from the thunderstorm cloud base, impinges on the ground surface and afterwards is convected radially, thus producing high wind speeds near the ground for a short period of time (Fujita, 1985). In order to closely imitate the natural phenomena, it is proposed to release a stored mass of air suddenly from the roof instead of a continuous jet of air. In the simulations carried out so far, both the horizontal shear method and guide louver method were considered for producing tornado-like flows. It may be noted that far more elaborate controls (i.e. the velocity of each fan needs to be controlled individually) are required to operate the horizontal shear method as against the simpler control (the fan speed and guide louver angle is same for all the fans) of the guided louver method. So the latter method alone was adopted for the modified design.

The design of the WindEEE dome was modified to meet the above requirements. While doing so, practical engineering considerations were kept in mind. Figure 4.8 shows this modified domain of the inner dome of the WindEEE dome. Four specific aspects have undergone changes and all other aspects remain the same. (1) One pair of parallel walls (2 sides) with a uniformly spaced array of 15 columns by 4 row of fans (diameter  $d_1 = 0.8$  m) has been introduced to facilitate the straight flow mode of operation. (2) On the remaining side walls of the dome, 8 columns by 1 row of fans (diameter  $d_1 = 0.8$  m) was introduced in place of 8 columns by 2 rows of fans (0.5 m diameter). (3) The vaulted roof was replaced with a flat roof in order to allow translation and the modified base to roof height  $H = 4$  m. ( Also simulations with vaulted roof for straight flow showed that large re-circulating flows were produced in the vaulted region of the roof and caused non-uniform straight flow. To avoid this flat roof was used.) (4) The roof has a circular opening of diameter  $D = 4$  m with an automated open-close shutter. Above the roof opening there is a hexagonal top plenum with 3 fans each (diameter  $d_2 = 1$  m) on all the six sides. The hexagonal top plenum has a diameter  $D_p = 12$  m and height  $h = 7$  m and also has six rectangular air outlets with shutters. This was introduced to improve the downburst flow.



To operate the WinDEE dome in the straight-flow mode, the roof opening is closed. Out of the pair of opposite side walls with 15 X 4 arrays of openings, one side is used as air inlet by connecting the fans and the other side is used as outlet. This creates a straight flow between them in the test chamber. The tornado mode of operation is enabled by using 8 X 1 arrays of fans on all the 6 side walls as air inlet and the shutter in the roof and on the rectangular air outlets in the plenum are opened to provide exit. While operating the dome in the downburst mode, the roof shutter and shutters on the rectangular air outlets in the plenum are closed initially, the fans in the plenum are used for pumping air into the plenum till a sufficient high pressure is built and then the air is suddenly released into the bottom test chamber by rapid opening of the automated roof shutter. The air flows down and exits through the 8 X 1 array of fan openings in all the six side walls.

Numerical simulations were again performed on the modified design configuration to confirm that the changed configuration still produces the desired flow fields of straight, tornado-like and downburst-like flows.

#### **4.3.1 Numerical setup:**

The computational domain of the WinDEE dome used in the downburst-like flow, tornado-like flow and straight flow simulations are shown in Figures 4.9, 4.10 and 4.11, respectively. Like the simulations for the preliminary design described in section 4.2, in the following simulations also the fans and the roof shutter are not modeled and are replaced by flat circular openings. The boundary conditions used in the simulations are given in Table 4.3.

The commercial CFD software CFX was used for analyzing the numerical solution. For the straight flow simulation shear-stress transport (SST) K-W model was used for modeling turbulence. Previous numerical studies on tornado and downburst (Kim and Hangan, 2007, Hangan and Kim, 2008) have indicated that out of all the RANS models the Reynolds stress model (RSM) is better in predicting the characteristics of such flows, so the current simulations use RSM for modeling turbulence in the tornado

and downburst simulations. Steady state simulations were performed for straight flow and tornado-like flow and unsteady simulations were performed for downburst-like flow.

Grid convergence was done on an unstructured grid showing that a grid close to 5 million cells was necessary for straight flow simulation and close to 4 million cells for both tornado and downburst simulations. The segregated implicit solver, SIMPLEC pressure velocity coupling and second order discretization for pressure, momentum, turbulent kinetic energy, specific dissipation rate and Reynolds stresses were used.

#### 4.3.2 Downburst:

During the downburst mode of operation in the WindEEE dome, a mass of air at high pressure is released suddenly from the roof opening for a short period of time. This boundary condition is replaced in the current simulation by using a constant velocity inlet boundary condition at the roof opening and analyzing the time varying flow pattern using an unsteady simulation. This can be regarded as equivalent to a sudden-burst situation when considered over a time frame needed for the initial touch down of the jet and a few intervals immediately there after. The unsteady simulation for the modified inner domain (detailed description given in section 4.3.1) was performed for a roof shutter opening of diameter  $D = 4$  m and an inlet jet velocity ( $V_{\text{Jet}}$ ) of 30 m/s. As the base to roof height  $H$  is 4m, the  $H/D$  ratio for the current simulation is 1. The Reynolds number ( $Re$ ) as defined in equation 1 is calculated to be 8,000,000. The  $D$ ,  $H/D$  ratio and  $Re$  satisfy the requirements mentioned in section 4.2.2 for downburst simulations.

Figure 4.12 shows the velocity vector in the vertical plane for different non-dimensional time steps ( $T = (t * V_{\text{Jet}})/D$ ). These plots show the ring-vortices formed due to the Kelvin-Helmholtz instability caused by the shear between the jet flow and the ambient still air. The ring-vortex touches the surface at time  $T = 2.7$  and is advected along the radial direction. Past simulations (Kim and Hangan, 2007) have shown that the vortex touch-down causes local accelerations near the wall which produce velocities of the same order of magnitude as the inlet jet velocity close to the surface. It can be seen

from the plots that in the current simulation also velocities near the ground following the vortex touch-down are nearly of the same order of magnitude as the inlet jet velocity. It was observed from the simulation that maximum radial velocity occurs around radial distance  $R/D = 1$  and height  $Z/D = 0.02$ , the maximum radial velocity  $V_{\text{rad-max}} = 1.5V_{\text{jet}}$  and mean radial velocity  $V_{\text{rad-mean}} = V_{\text{jet}}$ . Kim and Hangan (2007) have also shown the formation of multiple vortices around the principal vortex after touch down. However, the current simulation does not capture the formation of multiple vortices. A possible reason for this is the fact that the opening in the peripheral wall for the WindEEE configuration tends to streamline the flow and therefore might impede the formation of consequent vortices.

A comparison is also made between the semi-empirical model proposed by Holmes and Oliver (2000) and the current simulation shown in Figure 4.13. The figure compares the horizontal radial wind speed along the radial distance at time steps  $T = 1.8, 2.7, 3.6$  (Note: ring vortex touches the surface at  $T = 2.7$ ). The results show a good match especially with the radial velocity profile after the touch down ( $T = 3.6$ ) where the ring-vortex has advected to  $r/D = 1$  and the maximum radial velocities are observed. These results show that the WindEEE dome configuration is able generate the flow features observed in downburst flows.

#### 4.3.3 Tornado:

The current simulation is performed for the modified inner domain as described in section 4.3.1. The objective of the current simulation is to demonstrate that the modified configuration of WindEEE dome (more specifically the 8 X 1 array of fans (dia 0.8m) instead of the 8 X 2 array of fans (0.5m) on the side walls) would also produce an  $S = 2.0$  (F4) tornado. It was observed that normal and tangential velocities of  $U_{\text{in}} = 15.182$  m/s and  $V_{\text{in}} = 5.05$  m/s at the inlet (Equivalent fan velocity  $U_{\text{Fan}} = 16$  m/s and guide louver angle  $\theta = 18.4^\circ$ ) produce a tornado around  $S = 2$ .

The simulation results were again compared with the full scale data from the F4 Spencer, South Dakota tornado in the same manner as was done for the simulation of the preliminary design described in section 4.2.3 and the comparison is shown in Figure 4.14. The plot shows an encouraging match outside the core radius. Following the method of Hangan and Kim (2008) a velocity-scale can be obtained by comparing the maximum tangential velocity  $V_{\max}$  between the WindEEE model scale tornado simulation and the Doppler data for the real scale tornado. Similarly, by comparing the radius  $R_{\max}$  and height  $Z_{\max}$  at which the  $V_{\max}$  occurs in the WindEEE with respective real scale values, a length-scale can be arrived at. The length scale obtained by comparing  $R_{\max}$  and that obtained by comparing  $Z_{\max}$  need to be of the same order. Based on these criteria the velocity-scale was found to be approximately 2 and the length-scale to be 130.

The results of the current simulation are further compared with the CFD simulation of an  $S = 2$  tornado generated in a Ward-type TVC. (The Ward type TVC simulations were performed using Fluent 6.3 software. Similar to the current CFD simulation of the tornado-like flow in WindEEE dome, the RSM turbulence model, SIMPLEC pressure velocity coupling and second order discretization for pressure, momentum, turbulent kinetic energy, specific dissipation rate and Reynolds stresses were used.) Figure 4.15 compares the plot of the vertical profiles of the normalized tangential, radial and axial velocity at the core radius  $R_{\max}$  (i.e. the radius at which the maximum tangential velocity  $V_{\max}$  occurs). The velocities are normalized with maximum tangential velocity and height is normalized with core radius. In tornadic flows the convergence (radial velocity) is limited to the region close to the base surface and the tangential velocity increases from zero at the base to a maximum value along the height and remains nearly constant thereafter. This characteristic feature is observed in the plot. It shows that overall the tornado produced in the WindEEE has similar flow characteristics with the tornado produced in a Ward type TVC. Differences seen may be attributed to the difference in the geometry and inlet conditions of the two systems.

#### 4.3.4 Straight flow:

To serve as a conventional straight flow wind tunnel, the WindEEE dome should be capable of generating a wind field inside the test chamber meeting the following stipulations. 1) A maximum wind speed of around 15m/s should be realized in the middle of the chamber. 2) The velocity profile over a span-wise distance of approximately 10m and height 3.5m should be uniform with variation, if any, not more than  $\pm 5\%$ .

The CFD simulation was performed for inlet fan speeds of 27 m/s. Though the maximum wind speed of around 15 m/s was achieved at the middle of the test chamber, the velocity profile did not remain flat over the full span distance of 14 m due to large regions of re-circulating flow on either side of the primary straight flow region. To set right this aspect, slotted removable walls were introduced along the length of the chamber on either side of the inlet and outlet wall. These walls have 33% open area with 360mm wide flat strips and 210 mm opening between strips. The simulations were again performed for the same inlet fan speed of 27 m/s. The domain used in the simulation is shown in Figure 4.16.

Figure 4.17 shows the plot of velocity across the span at a height of 2m above the ground (i.e. at half the height of the inner chamber) at different locations along the direction of the flow ( $X = 2.5$  m, 7.5 m, and 12.5 m measured from the inlet wall). The figure shows that a uniform velocity profile with a velocity of 16 m/s is achieved across the span over a distance of close to 10m. Figure 4.18 shows the plot of velocity across the span at the middle of the chamber for different heights from the ground ( $X = 1$  m, 2 m, and 3 m). It can be seen that uniform velocity profile are achieved at every height up to 3.5 m over a transverse extent of approximately  $\pm 4.5$ m. The variation in flow is in the  $\pm 5\%$  limits and this is considered satisfactory. There are clear acceleration of the flow towards the sidewalls probably due to the formation of Ekman vortices and lateral boundary layers. These accelerations can be further corrected by an adequate deceleration of the fans near the lateral walls.

#### 4.4 Conclusions:

Numerical simulations for the WinDEEE dome axi-symmetric flow fields were conducted and the results show feasibility for generating tornado-like and downburst-like wind profiles using the preliminary design. Subsequently, design optimizations were introduced to enhance the capability of the dome with respect to straight flow and downburst modes of operations. Analysis shows that an array of 8 by 1 fans in 4 side walls combined with an array of 15 by 4 fans on the remaining pair of opposite walls, a pair of removable slotted partition, and a top plenum fitted with automated shutter opening offer adequate choices of inlet and outlet boundary conditions to realize all the three desired flow fields.

In the downburst simulations the maximum radial velocity is obtained at heights within 5% of the initial jet diameter, as desired. Also the simulations show the production of ring-vortices generally observed in downburst-like flows due to Kelvin-Helmholtz instability. In the tornado simulation, a tornado with swirl ratio of approximately  $S = 2$  was simulated and results compare well with observed data from a real tornado and numerically simulated results from a Ward type TVC. The straight flow simulations also produce a uniform velocity profile along the span-wise direction with variations within  $\pm 5\%$ .

The WinDEEE dome design would evolve further following engineering design implementations. Future plans include the construction of a laboratory scale model of the complete WinDEEE dome and experimental analysis of its flow fields. This model will be used to validate (benchmark) the present CFD simulations and to further address issues related to the translation of both tornadoes and downbursts.

#### 4.5 References:

Chay, M.T., Letchford, C.W., 2002. Pressure distributions on a cube in a simulated thunderstorm downburst—Part A: stationary downburst observations. *Journal of Wind Engineering and Industrial Aerodynamics* 90(7), 711-732.

Church, C.R., Snow, J. T., Baker, G. L., Agee, E. M., 1979. Characteristics of tornado like vortices as a function of swirl ratio: A laboratory investigation. *Journal of the Atmospheric Sciences* 36, 1755-1776.

Davies-Jones, R. P., 1973. The dependence of core radius on swirl ratio in a tornado simulator. *Journal of the Atmospheric Sciences* 30, 1427-1430.

FLUENT 6.3 User's guide, 2006. Fluent Inc, Lebanon, USA.

Fujita, T. T., 1985. The downburst: microburst and macroburst. SMRP Research Paper 210. University of Chicago.

Haan Jr, F.L., Sarkar, P.P., Gallus, W.A., 2007. Design, construction and performance of a large tornado simulator for wind engineering applications. *Engineering Structures*, doi:10.1016/j.engstruct.2007.07.010

Hangan, H., Xu, Z., 2005. Scale, roughness and initial conditions effects in impinging jets with application to downburst simulations, in: *Proceedings of the 10th Americas Conference on Wind Engineering (10 ACWE)*, Baton Rouge, LA, USA.

Hangan, H., Kim, J., 2008. Swirl ratio effects on tornado vortices in relation to the Fujita scale. *Wind and Structures* 11(4), 291-302.

Holmes, J. D., Oliver, S. E, 2000. An empirical model of a downburst. *Engineering Structures* 22, 1167-1172.

Kim, J., Hangan, H., 2007. Numerical simulations of impinging jets with application to downbursts. *Journal of Wind Engineering and Industrial Aerodynamics* 95, 279-298.

Launder, B. E., Spalding, D. B., 1972. *Lectures in mathematical models of turbulence*. Academic Press, London, England.

Lewellen, W. S., Lewellen, D. C., Sykes, R. I., 1997. Large-eddy simulation of a tornado's interaction with the surface. *Journal of the Atmospheric Sciences* 54, 581–605.

Sarkar, P., Haan, F., Gallus, Jr., W., Le, K. and Wurman, J., 2005. Velocity measurements in a laboratory tornado simulator and their comparison with numerical and full-scale data. 37th Joint Meeting Panel on Wind and Seismic Effects, Tsukuba, Japan.

Ward, N. B., 1972. The exploration of certain features of tornado dynamics using a laboratory model. *Journal of the Atmospheric Sciences* 29, 1194-1204.

Wood, G.S., Kwok, K.C.S., Motteram, N.A, Fletcher, D.F, 2001. Physical and numerical modelling of thunderstorm downbursts. *Journal of Wind Engineering and Industrial Aerodynamics* 89(6), 535–552.



Boundary name	BC for tornado-like flow	BC for downburst-like flow
Roof opening (Diameter D)	Outflow	Velocity inlet
8 X 2 Side wall openings (Diameter d)	Velocity inlet	Outflow
6 Side walls	Free-slip wall	Free-slip wall
Roof	Free slip wall	Free slip wall
Base	No-slip wall	No-slip wall

Table 4.1: Boundary conditions for the preliminary WinDEE dome domain for the simulations of tornado-like and downburst-like flows

Case Num	Inlet jet Dia D (m)	H/D	Reynolds Number
1	1.75	4	2,251,656
2	3.5	2	4,635,762
3	5	1.4	6,622,517

Table 4.2: The H/D ratio and Reynolds number for the three downburst cases simulated using the preliminary WinDEE dome domain.

Tornado-like flow		Downburst-like flow		Straight flow	
Boundary name	Boundary condition	Boundary name	Boundary condition	Boundary name	Boundary condition
8 X 1 Inlet opening	Velocity inlet	8 X 1 Outlet opening	Outflow	15 X 4 Inlet opening	Velocity inlet
Roof opening	Interior	Roof opening	Velocity inlet	15 X 4 Outlet opening	Outflow
6 Side walls	Free-slip wall	6 Side walls	Free-slip wall	6 Side walls	Free-slip wall
Flat roof	Free slip wall	Flat roof	Free-slip wall	Flat roof	Free-slip wall
Base	No-slip wall	Base	No-slip wall	Base	No-slip wall
6 Plenum outlets	Outflow				
Plenum	Free slip wall				

Table 4.3: Boundary conditions for the tornado, downburst and straight flow simulations in the modified WinDEE dome domain

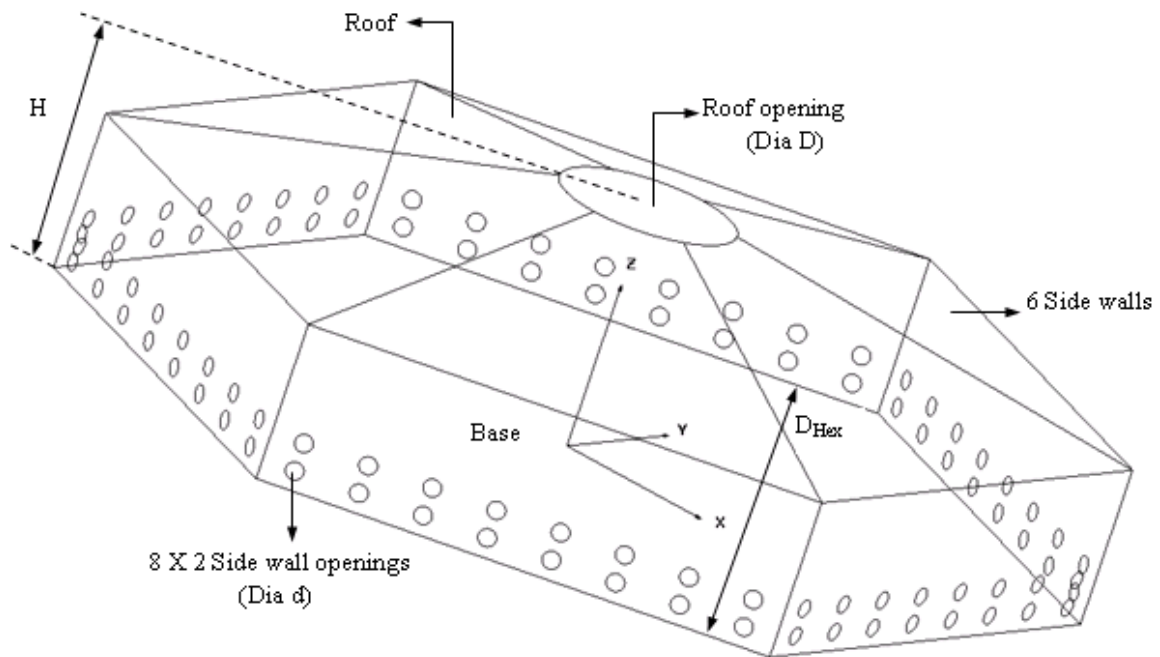


Figure 4.1: The computational domain: the inner chamber of WindEEE dome.

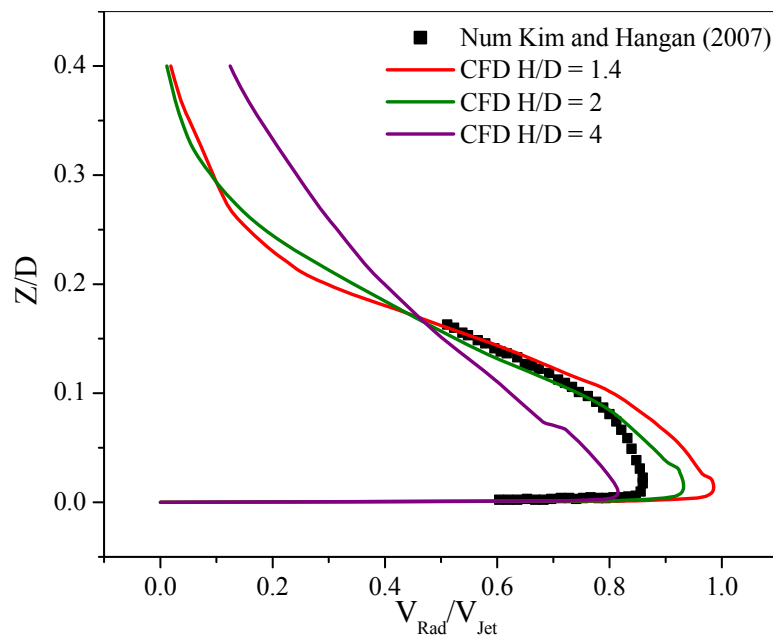


Figure 4.2: The plot of normalized radial velocity vs. normalized height at  $R/D = 1$ , the numerical result of Kim and Hangan (2007) was for a  $Re = 2,000,000$ ,  $H/D = 4$ .

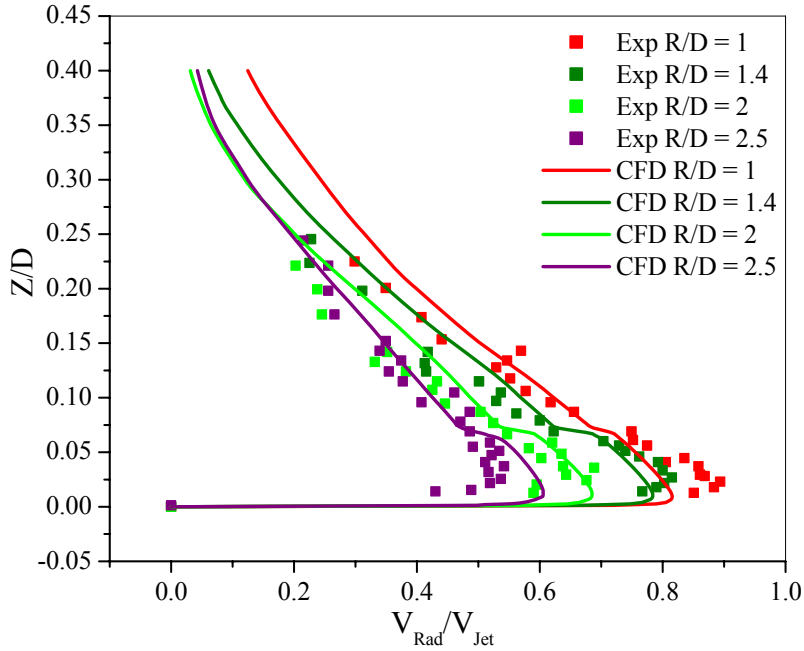


Figure 4.3: The plot of normalized radial velocity vs. normalized height at various  $R/D$  ratios, the experimental results of Hangan and Xu (2005) were for a  $Re = 27,000$ ,  $H/D = 4$  and the current CFD results were for  $Re = 2,251,656$ ,  $H/D = 4$ .

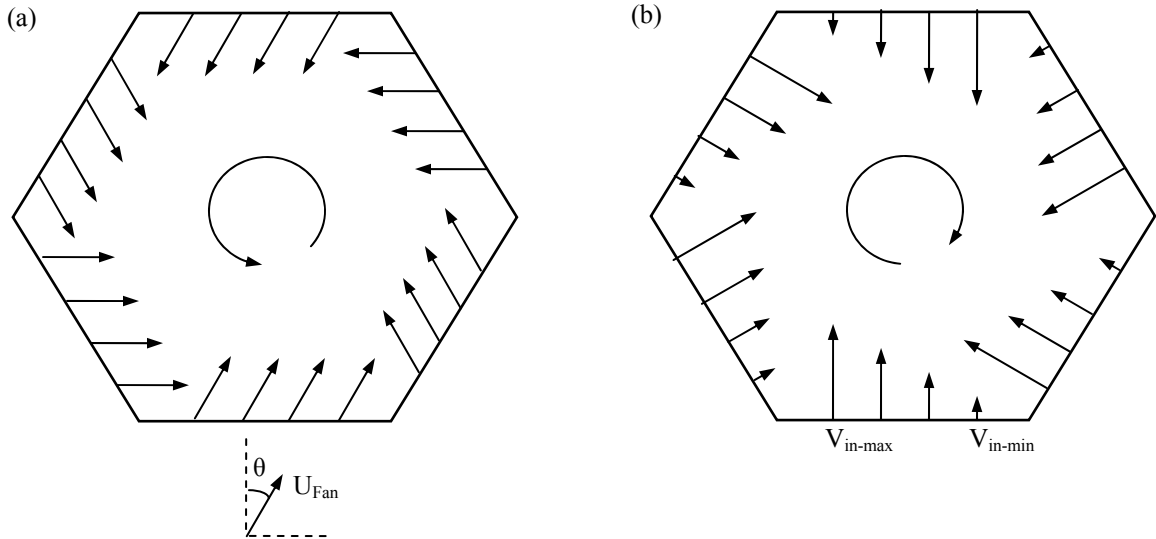


Figure 4.4: Conceptual schematic of inlet condition for tornado-like flows (a) Guide louver method: (b) Horizontal shear method

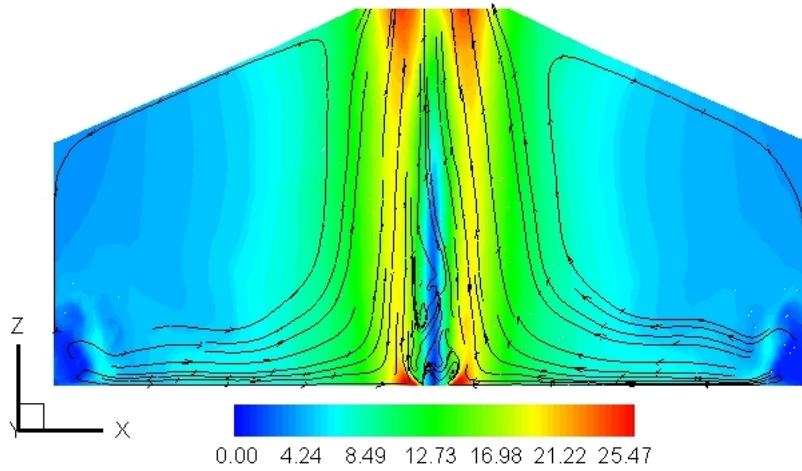


Figure 4.5: The contour plot of the velocity magnitude (m/s) of the current CFD simulation of tornado in the WindEEE dome showing the two-celled tornado.

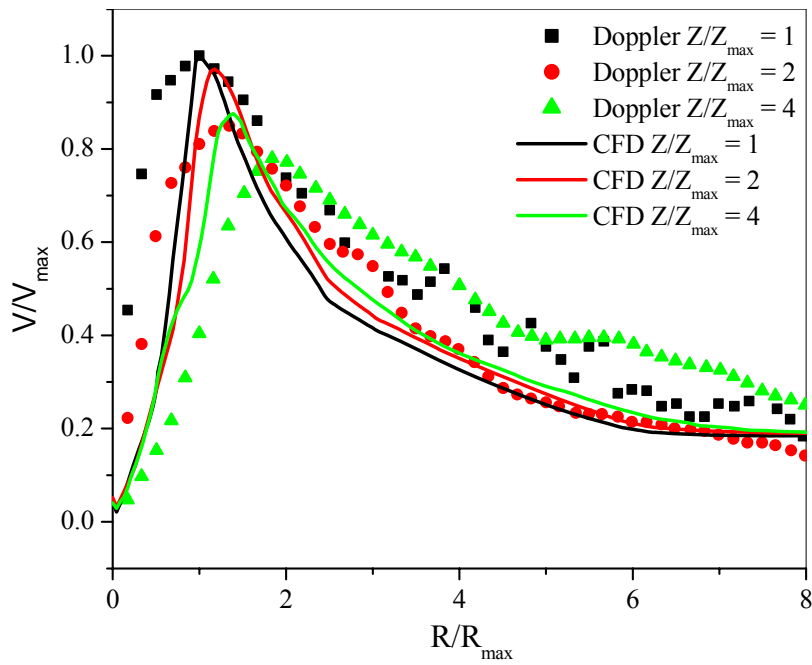


Figure 4.6: The plot of normalized tangential velocity vs. the normalized radial distance, comparing the current CFD simulation of tornado for the preliminary dome design (Case1: guide louver type input) and the real scale tornado velocities measured with Doppler radar.

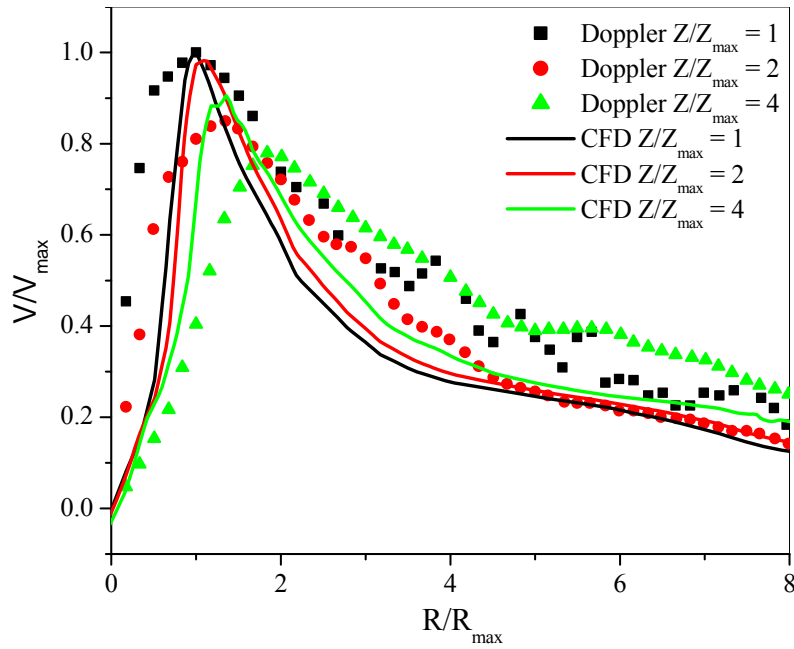


Figure 4.7: The plot of normalized tangential velocity vs. the normalized radial distance, comparing the current CFD simulation of tornado for the preliminary dome design (Case2: horizontal shear type input) and the real scale tornado velocities measured with Doppler radar.

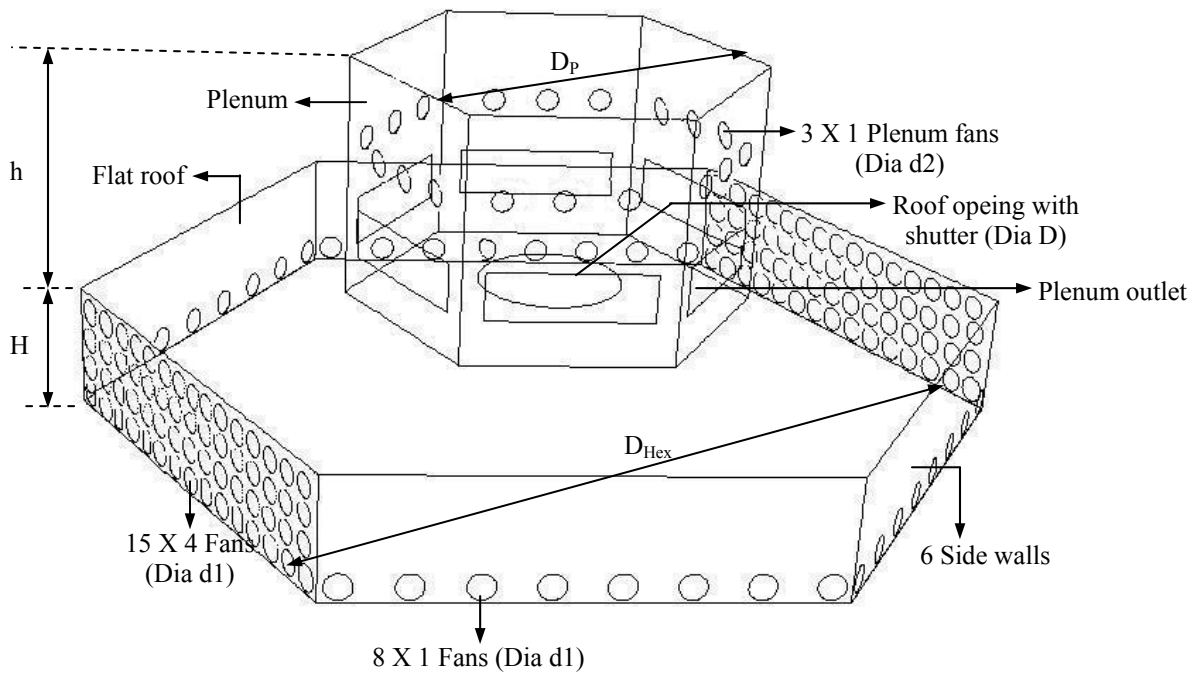


Figure 4.8: The modified inner chamber of WindEEE dome.

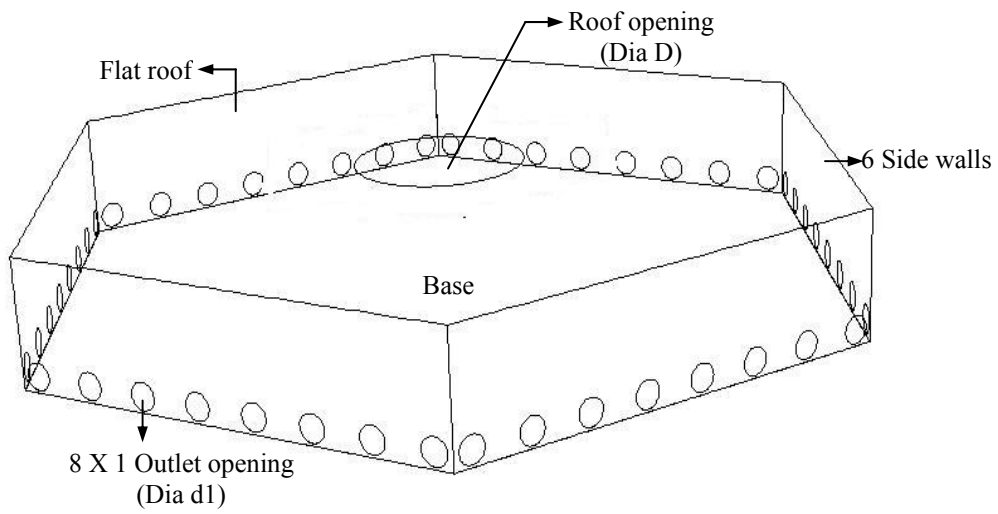


Figure 4.9: The computational domain: Downburst-like flow simulation.

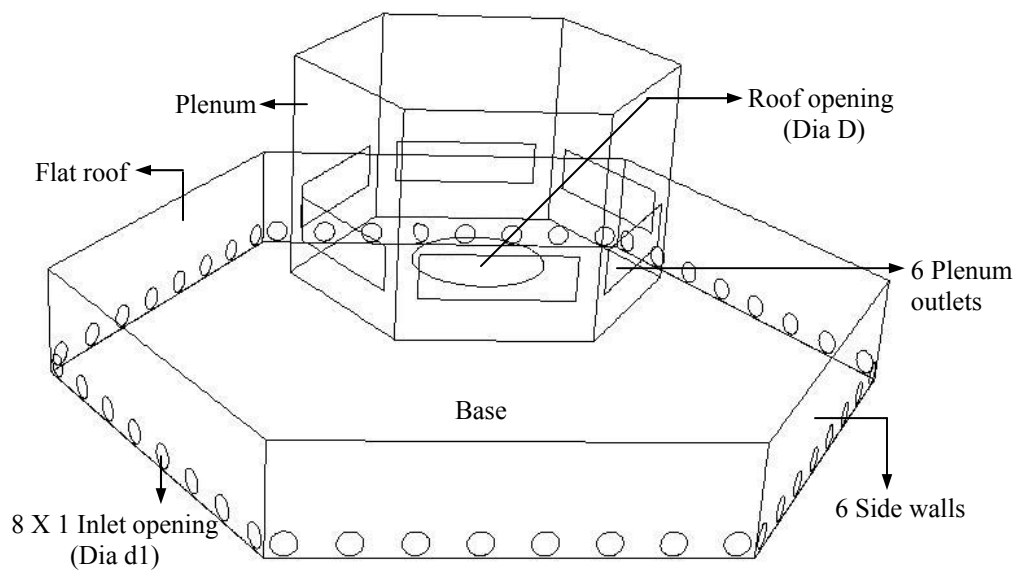


Figure 4.10: The computational domain: Tornado-like flow simulation.

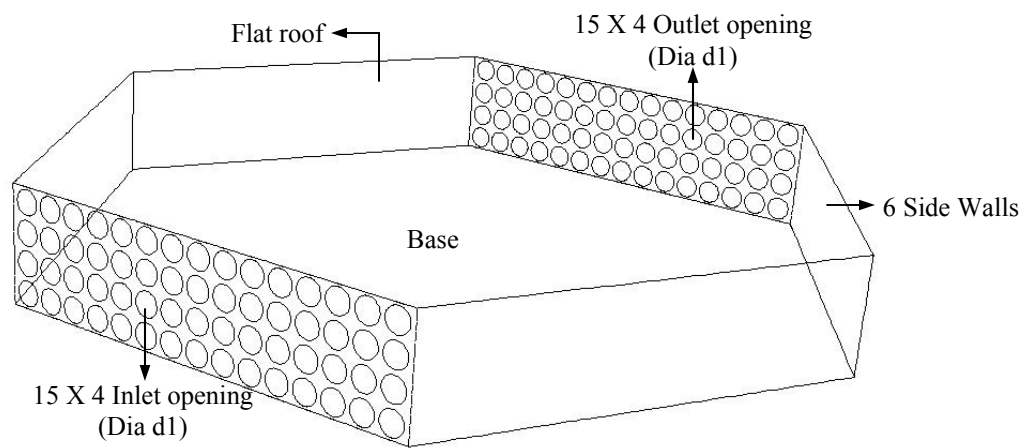


Figure 4.11: The computational domain: Straight flow simulation.

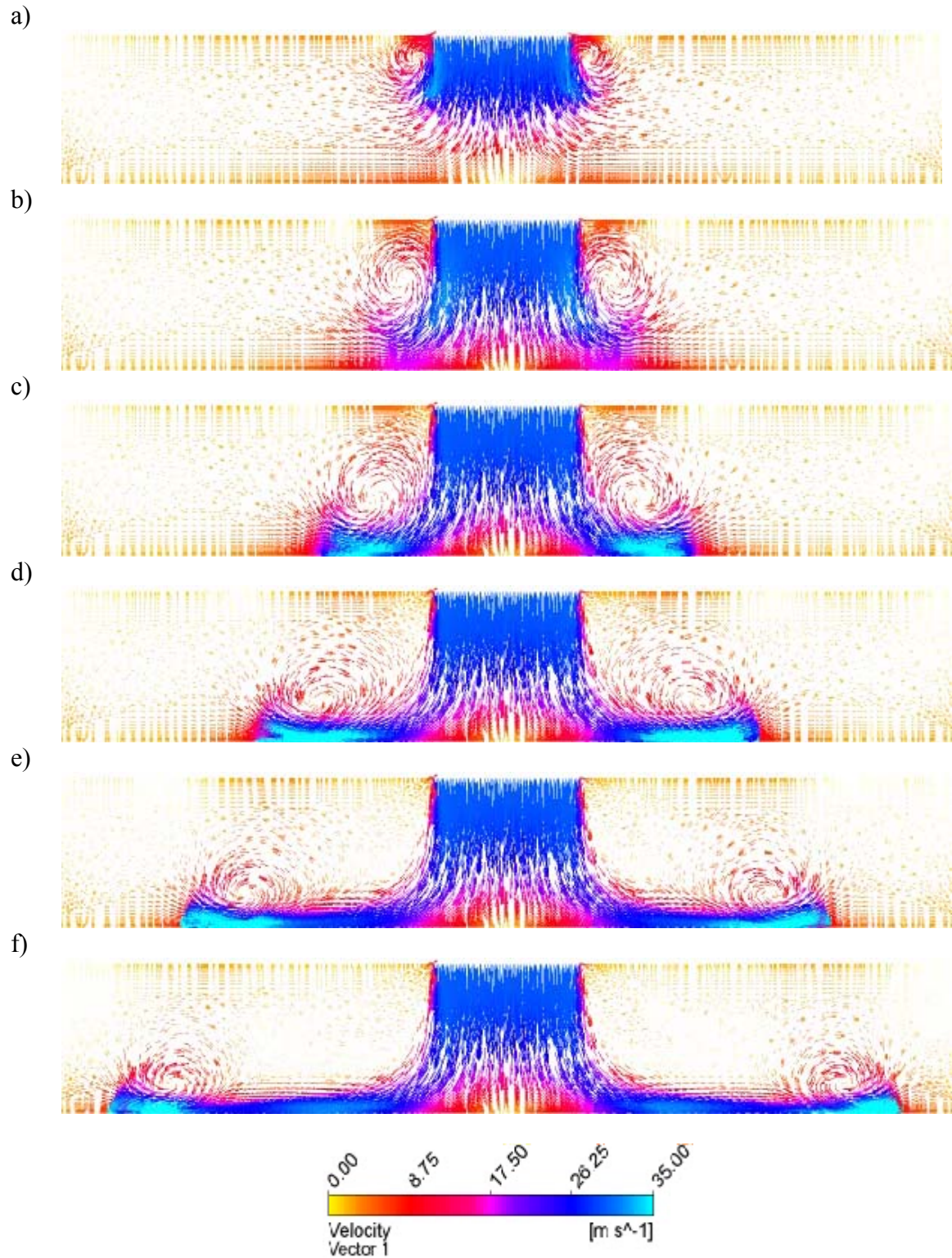


Figure 4.12: The velocity vectors in the vertical plane showing the ring vortex evolution in the downburst flow at different non-dimensional time frames  $T = (t * V_{jet})/D$  a)  $T = 0.9$ , b)  $T = 1.8$ , c)  $T = 2.7$ , d)  $T = 3.6$ , e)  $T = 4.5$ , f)  $T = 5.4$



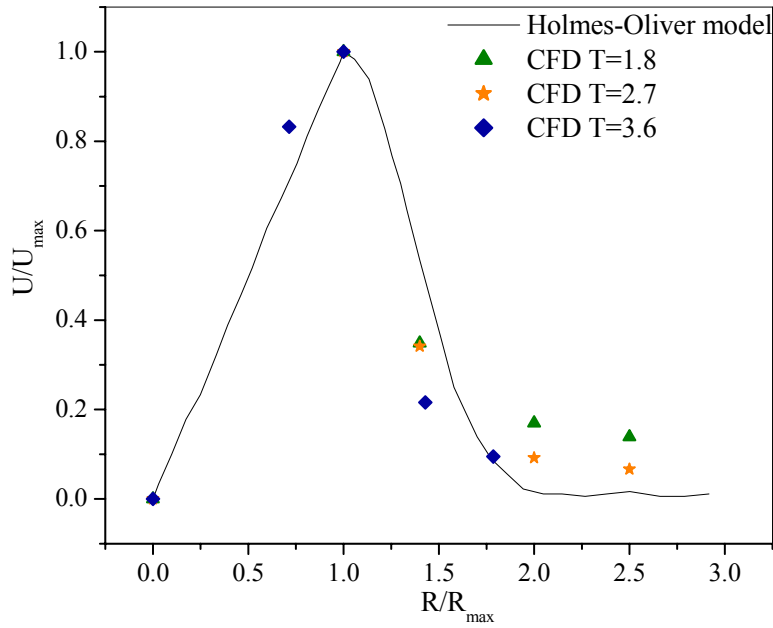


Figure 4.13: The plot of normalized radial velocity vs. the normalized radial distance, comparing the current CFD simulation of downburst flow for the modified domain and the semi-empirical model for downburst flow by Holmes and Oliver (2000).

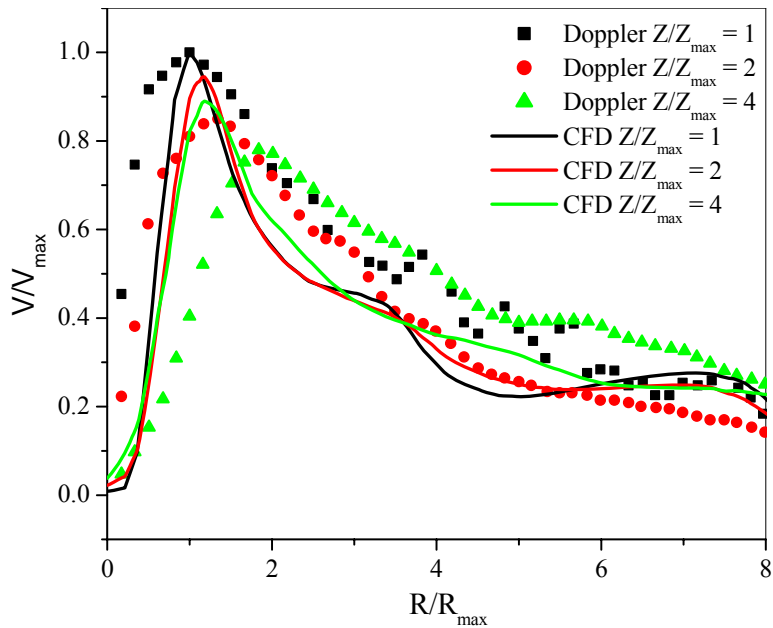


Figure 4.14: The plot of normalized tangential velocity vs. the normalized radial distance, comparing the current CFD simulation of tornado for the modified domain and the real scale tornado velocities measured with Doppler radar.

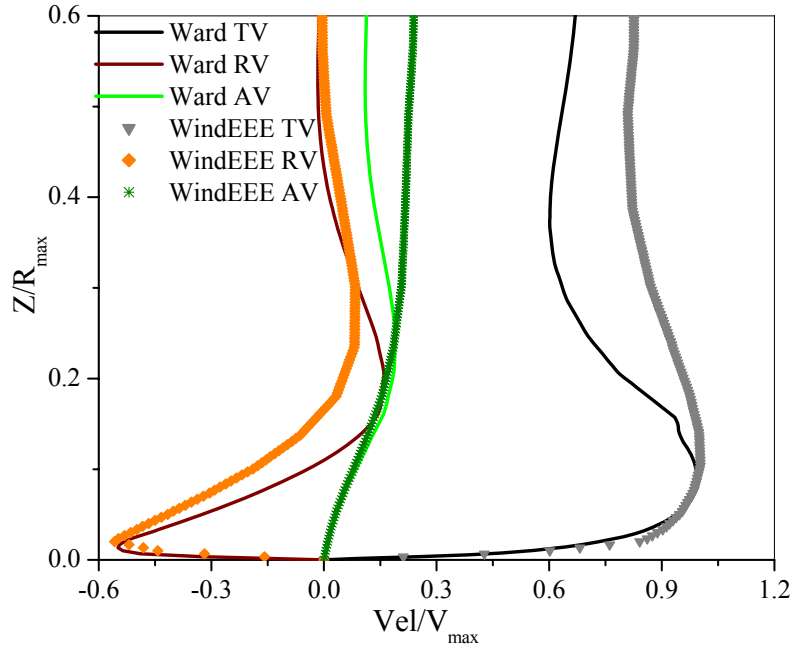


Figure 4.15: The plot of normalized velocity vs. the normalized height at core radius  $R_{max}$ , comparing the current CFD simulation of tornado in the WindEEEE dome and the CFD simulation of tornado of a Ward type TVC. (TV: Tangential velocity, RV: Radial velocity, AV: Axial velocity)

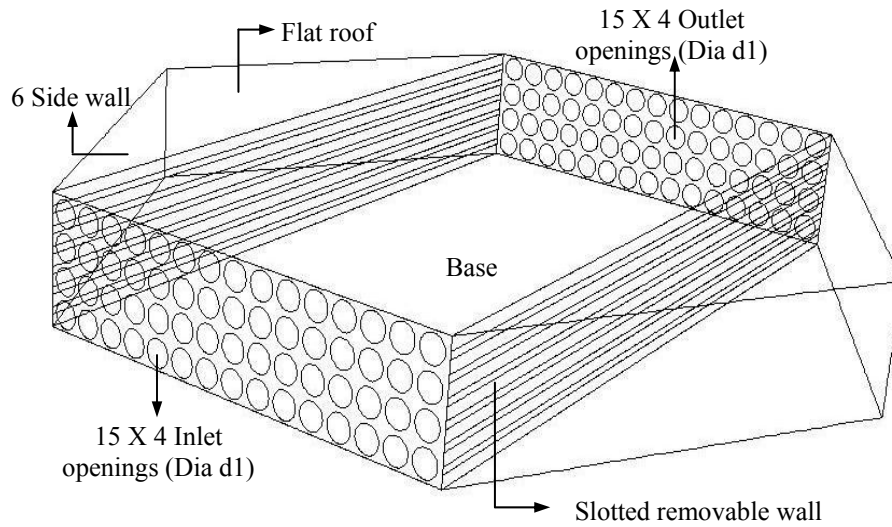


Figure 4.16: The computational domain: straight flow with side slotted walls.

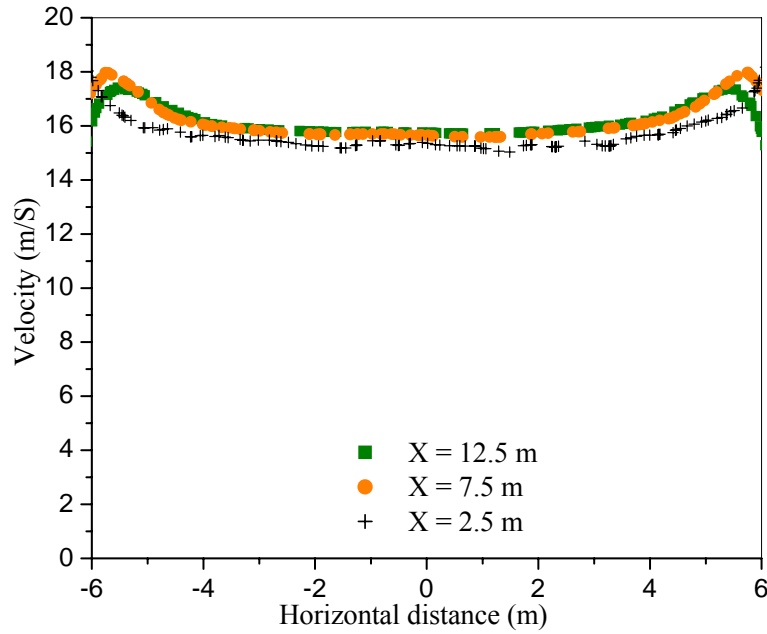


Figure 4.17: The plot of velocity vs. span-wise horizontal distance at mid height (2 m) at different length-wise distances ( $X = 2.5$  m,  $7.5$  m, and  $12.5$  m) from the wall (with the array of fans) for the straight flow.

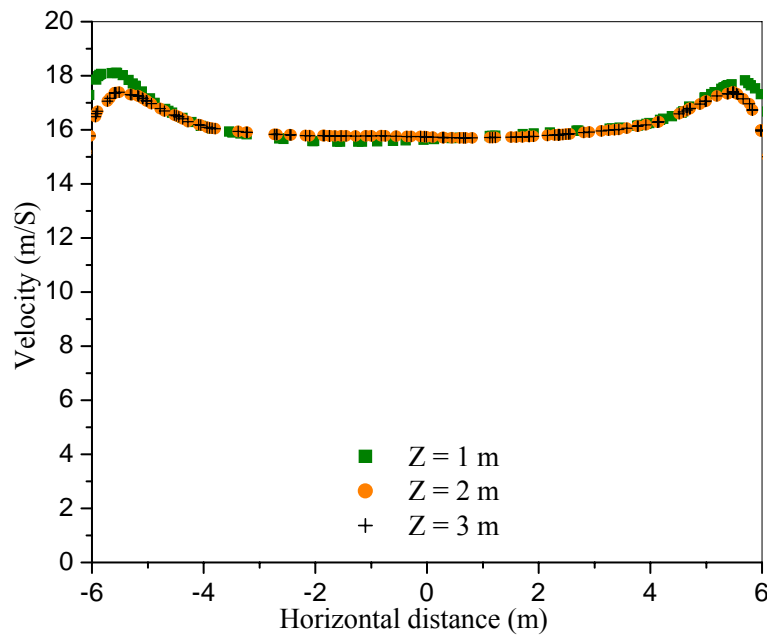


Figure 4.18: The plot of velocity vs. span-wise horizontal distance at mid-section ( $X = 12.5$  m) at different heights ( $Z = 1$  m,  $2$  m, and  $3$  m) from the base wall for the straight flow.

## Chapter 5: Numerical Simulation of Atmospheric Vortex Engine

### 5.1 Introduction:

The atmospheric vortex engine (AVE) is a green carbon free technology to produce electricity developed by Louis Michaud (<http://vortexengine.ca>). It uses an artificially created vortex to capture the mechanical energy produced during upward heat convection. The vortex is created by admitting warm or humid air tangentially into the base of a circular wall. The heat source can be solar energy, warm seawater or waste industrial heat. The mechanical energy is produced in peripheral turbo-generators.

The AVE has the same thermodynamic basis as the solar chimney (Schlaich et.al, 2005, Haaf et.al, 1983 and Haaf, 1984). A solar chimney consists of a tall vertical tube, a transparent solar collector surrounding the base and a turbine located at the inlet of the tube. One of the factors influencing the heat to work conversion efficiency of a solar chimney is the height of the chimney. The efficiency is directly proportional to the height. For example the Manzanares solar chimney built in Spain in the 1980's with a 200m tall chimney, diameter of 10 m and solar collector of diameter 250m had a heat to work conversion efficiency of 0.2% and the proposed EnviroMission chimney in Australia has a 1000m tall chimney with a diameter of 130 m and a solar collector of area 40 km<sup>2</sup> has a heat to work conversion efficiency of 3%. The costs of building high chimneys limit their height and in turn their efficiency.

Michaud (1975, 1977) suggested a possible way of eliminating the chimney by imitating naturally occurring tornado-like flows based on the observation that in tornado like vortex flows the convergence is limited to the bottom of the vortex close to the ground and the centrifugal force associated with the circular-velocity limits the convergence (i.e. mixing of ambient air) at other heights. In other words the centrifugal force in a vortex acts as the physical wall of a chimney. This typical convergence characteristic can be easily demonstrated in the case of a laboratory scale numerically simulated tornado. Figure 5.1 illustrates the results from such a study; it shows the

normalized radial and tangential velocity at the core radius along the height. It can be seen that the radial velocity is high close to the ground and reduces along the height whereas the tangential velocity increases along the height and reaches a constant value. The AVE uses the above characteristics of tornadic flow and the physical wall of a chimney is replaced by the centrifugal force of an artificially generated vortex, so the efficiency is not limited by the physical height of the chimney. Also power generation cost is lowered by saving the construction cost of the chimney. Further detailed thermodynamic basis for the AVE are presented in Michaud (1977), Michaud (1995) and Michaud (1996).

In the current chapter numerical simulations of a prototype model-scale AVE are presented. The objective of the simulations is to study the overall flow field produced by the AVE. The effects of varying the geometric and physical parameters are also studied with a view to future design optimization. Further, the effect of cross wind flow is also studied, on a full-scale AVE.

## **5.2 Numerical simulation:**

The prototype model scale AVE has an octagonal column with 8 tangential inlets for the air. The base of the AVE is heated and maintained at a constant temperature. At the roof of the AVE there is a circular opening through which air leaves the AVE and enters the atmosphere. Figures 5.2a and 5.2b show the elevation and plan view of the prototype AVE. The dimensions used in the current simulations for the model-scale geometry are given in Table 5.1. The full-scale geometry is 20 times the model scale and the dimensions are given in Table 5.2.

The computational domain for the simulation is shown in Figure 5.3. It consists of an outer cubic domain 3m X 3m X 2m representing the ambient atmosphere and the AVE is modeled at the centre of the base of the outer cubic domain. The height of the domain chosen is five times the height of the AVE. This is adequate for the preliminary simulations performed here to test effectiveness of the AVE to generate tornado-like

vortex extending beyond its physical height. The side faces of the outer cubic domain are set as inlet boundary conditions with atmospheric pressure and ambient temperature and the top face is set as outlet with atmospheric pressure and ambient temperature. The bottom face is set as wall. The base wall of the AVE is maintained at a constant temperature as a heated plate and the air enters the AVE through the tangential inlet at a higher temperature than the ambient atmosphere. The detailed boundary conditions used in the simulation are given in Table 5.3.

The commercial Computational Fluid Dynamic software, Fluent6.3 was used for the 3D numerical simulation. The software uses Finite Volume Method (FVM) to discretize the equations of motion (Navier-Stokes equations, the continuity equation and the energy equation) and the segregated implicit solver option was employed to solve the equations.

Fluent employs Boussinesq model to solve the buoyancy driven natural convection flow problems. This model assumes density ( $\rho$ ) as a constant value in all solved equations, except the buoyancy term in the momentum equation. The Boussinesq approximation  $\rho = \rho_0(1 - \beta\Delta T)$  is used to replace the density from the buoyancy term, where  $\rho_0$  is the constant density,  $\beta$  is the thermal expansion coefficient and  $\Delta T = (T - T_0)$  is the temperature difference between actual and ambient temperature (Fluent 6.3, 2006). This model was used in the current AVE simulations. The Boussinesq approximation is only valid when  $\beta(T - T_0) \ll 1$ , and in the current simulations  $\beta(T - T_0) \approx 0.067$ . Details of this value and the other physical parameters of relevance are presented in Appendix C.

In buoyancy driven flows Rayleigh number  $Ra < 10^8$  indicates a buoyancy-induced laminar flow and transition to turbulence occurs over the range of  $10^8 < Ra < 10^{10}$ . In the current simulations  $Ra = 2.06 \times 10^9$  for the model-scale AVE. Even though the Rayleigh number for the flow in AVE indicate a transitional turbulence induced buoyancy flow, a pilot study was carried out using laminar simulations on the model-scale AVE to do an initial assessment of the flow field. Further simulations were carried out using the second

order unsteady  $k-\varepsilon$  turbulence model. An unstructured grid was used and further grid convergence was done and grid sizes were considered to be sufficient to cover the domain in its relevant details. For the model-scale AVE, around 200,000 cells were used for laminar simulations and 400,000 cells were used for turbulent simulations. Around 800,000 cells were used for the full-scale simulations. The interaction of the vortex flow with the base of the AVE was not the focus of the study, so a standard wall function model was used in the near-wall region. The SIMPLEC pressure velocity coupling and second order discretization for pressure, momentum, energy, turbulent kinetic energy and specific dissipation rate were employed.

### 5.2.1 Preliminary laminar simulations on model-scale AVE:

A preliminary laminar simulation was performed for a temperature difference of  $\Delta T = 20$  K between the inlet air and ambient air. Figures 5.4 and 5.5 show the contour plot of the tangential velocity in the YZ plane and the vector plot of velocity magnitude at  $Z = 0.4$  m plane (at the exit of AVE). It can be seen from these plots that a tornado like vortex flow was generated inside the AVE and the flow extended into the atmosphere till the top of the domain. Figure 5.6 shows the contour plot of temperature in the YZ plane. It can be seen that the warm plume does not get dissipated and the high temperature is maintained till the top of the domain, confirming the earlier statement that the vortex acts like a physical chimney and arrests the dissipation of heat at heights above the AVE. Figure 5.7 shows the contour plot of the velocity magnitude in the YZ plane. It shows the two-celled structure characteristic of high swirl ratio tornadic flows. The maximum velocity of 1.15 m/s was obtained near the top of the domain and the velocity of the air as it exits the vortex generator was around 0.687 m/s. Figure 5.8 shows the contour plot of static pressure in the YZ plane and the pressure drop in the region around the center is also characteristic of the tornadic flow as discussed in section 2.2.4.

All these observations namely, tangential velocity, temperature, velocity magnitude and static pressure taken together signify that the AVE is able to generate a tornado-like vortex flow sustaining the high temperature till the top of the domain.

### 5.2.2 $k-\varepsilon$ simulations on model-scale AVE:

The above simulation was performed again using  $k-\varepsilon$  turbulence model for the same temperature difference of  $\Delta T = 20$  K between the inlet air and ambient air. Figures 5.9 and 5.10 show the contour plot of the tangential velocity and velocity magnitude in the YZ plane respectively. These figures again confirm that the AVE produces vortex like flow and it extends into the atmosphere. The maximum velocity magnitude and the tangential velocity of the turbulent simulations are smaller than the laminar case because of the energy dispersion due to turbulence.

### 5.2.3 Design optimization:

The CFD simulations indicate that the current model-scale AVE geometry can produce a spiraling upward flow extending well above the AVE. The current dimensions of the key geometric parameters like deflector gap 'g1' (5% of deflector diameter ring 'd1'), tangential entry height 'h1' (20% of deflector diameter ring 'd1'), octagonal cylinder height 'h2' (20% of deflector diameter ring 'd1'), roof opening 'D3' (30% of deflector diameter ring 'd1') have produced satisfactory results and is a good starting point for future designs. Further design optimization of AVE can be achieved by studying the effects of changes in physical and geometric parameters in the model-scale AVE. The changes in geometric parameters like increased roof opening (D3), and increased domain height (Z), and changes in physical parameters like increased temperature difference between inlet air and ambient temperature ( $\Delta T$ ) were studied here. Both laminar and turbulent  $k-\varepsilon$  simulations were performed for all the three cases.

The contour plot of static pressure (Figure 5.8) shows that there is build up of pressure near the roof of the AVE. To reduce the area of the roof, the roof opening (D3) diameter was increased from 300mm to 600mm. The increase in roof opening did not affect the vortex other than causing an increase on the diameter of vortex formed. Figure 5.11 shows the contour plot velocity magnitude of the vortex in the YZ plane for the



increased roof opening. It was inferred that the roof opening diameter is not a critical parameter and future designs should adopt the smaller diameter (30% of deflector diameter ring 'd1') to produce a tight vortex and avoid the straight octagonal cylinder with roof by replacing it with a convergent octagonal cylinder.

The vertical domain height was increased from 2000 mm to 6000 mm. Figures 5.12 and 5.13 show the contour plot velocity magnitude and temperature of the vortex in the YZ plane for the extended domain. The increase in the height does not dissipate the temperature much and plume extends till the top of the domain.

The key physical parameter, temperature difference between the inlet air and ambient air ( $\Delta T$ ) was increased from 20 K to 30 K. The increase produced a much stronger vortex. Figure 5.14 shows the contour plot of velocity magnitude of the vortex in the YZ plane for  $\Delta T = 30$  K case and the maximum velocity is approximately 20% higher than the  $\Delta T = 20$  K case (Figure 5.9). It can be concluded that for a given geometric configuration of AVE, the vortex strength and in turn the power output is mainly controlled by temperature difference between the inlet air and ambient air ( $\Delta T$ ).

#### **5.2.4 Full-scale AVE simulations with cross wind:**

The results presented so far pertain to a lab scale model which will be studied indoors and atmospheric wind plays no roll in this situation. Full-scale AVE will be located outdoors and will be subject to the influence of atmospheric wind. A full-scale AVE with geometry 20 times the model-scale AVE has been proposed to be built. Simulation of a full-scale AVE was done to study the effect of cross wind on the vortex generated. Detailed domain dimensions used in the simulation are given in Table 5.2. For the full-scale dimensions considered here the Rayleigh number  $Ra = 1.648 \times 10^{13}$ . This indicates that the flow will be turbulent in nature, so  $k-\epsilon$  turbulent model simulations were performed.

An initial simulation without cross wind was performed as base case for comparison with the cross wind case. Figure 5.15 shows the contour plot velocity magnitude of the vortex in the YZ plane and Figure 5.16 shows the static pressure in the YZ plane. The features observed in these figures are similar to those observed in the model scale simulations, confirming the formation of tornado-like flows in the full-scale AVE also. The simulation was repeated with the inclusion of horizontal cross wind in the positive X direction. The horizontal wind has a power law mean velocity profile corresponding to an open terrain (with a velocity of 1.2 m/s at 10 m height).

Figures 5.17 and 5.18 show the contour plot of velocity and temperature in the XZ plane for the full scale geometry with cross flow of wind. As expected the column of vortex gets tilted in the direction of the wind. The pressure contours shown in Figure 5.19 indicate that even though the plume gets tilted, the changes in pressure drop at the base of the AVE is negligible when compared to that of the no cross wind case (Figure 5.16). The pressure drop at the base of the AVE is responsible for drawing the air inside the AVE and driving the turbo-generators located at the inlets, so even though the cross wind tilts the vortex, it does not greatly affect the power generation capacity of the AVE.

### **5.3 Conclusion:**

The CFD analysis of a model-scale Atmospheric Vortex Engine (AVE) was performed. The results show that the AVE can generate a vortex flow in the atmosphere much above the AVE and the vortex acts as a physical chimney limiting the mixing of surrounding air into the raising plume of hot air. A parametric study was conducted and provides a good starting point for future designs. For a given geometry, the physical parameter  $\Delta T$  (temperature difference between the inlet air to AVE and ambient air) is the main parameter that controls the strength of the vortex and in turn the power output. The full scale simulations subjected to cross wind show that the power generation capacity is not affected by the cross winds.

The current full scale simulations do not consider actual temperature gradient present in the atmosphere. Future studies should include the effect of various atmospheric stratifications: stable, unstable and neutral for further accurate results.

#### **5.4 References:**

Haaf, W., 1984. Solar Chimneys - Part II: Preliminary Test Results from the Manzanares Pilot Plant. *International Journal of Solar Energy* 2(2), 141–161.

Haaf, W., Friedrich, K., Mayr, G., and Schlaich, J., 1983. Solar Chimneys. Part 1: Principle and Construction of the Pilot Plant in Manzanares. *International Journal of Solar Energy* 2(1), 3–20.

Fluent 6.3 User's guide, 2006. Fluent Inc, Lebanon, USA.

Michaud, L. M., 1975. Proposal for the use of a controlled tornado-like vortex to capture the mechanical energy produced in the atmosphere from solar energy. *Bulletin of the American Meteorological Society* 56, 530-534.

Michaud, L. M., 1977. On the energy and control of atmospheric vortices. *Journal de Recherches Atmospheriques* 11(2), 99-120.

Michaud, L. M., 1995. Heat to work conversion during upward heat convection. Part I: Carnot engine method. *Atmospheric Research* 39, 157-178.

Michaud, L. M., 1996. Heat to work conversion during upward heat convection. Part II: Internally generated entropy method. *Atmospheric Research* 41, 93-108.

Michaud, L. M., 1999. Vortex process for capturing mechanical energy during upward heat-convection in the atmosphere. *Applied Energy* 62, 241-251.

Schlaich, J., Bergermann, R., Schiel, W., and Weinrebe, G., 2005. Design of commercial solar tower systems—utilization of solar induced convective flows for power generation, *Journal of Solar Energy Engineering* 127, 117-124.

<b>Parameter Name</b>	<b>Parameter Description</b>	<b>Base Value (mm)</b>
d1	Inner octagonal cylinder diameter	1000
d2	Outer octagonal cylinder diameter	1050
d3	Roof opening diameter	300
d4	Floor opening diameter	0
d5	Upper circular cylinder diameter	800
g1	Gap between deflectors	50
h1	Tangential entry height	200
h2	Octagonal cylinder height	200
h3	Upper cylinder height	0
Z	Domain height	2000

Table 5.1: Dimensional specifications for prototype model-scale AVE

<b>Parameter Name</b>	<b>Parameter Description</b>	<b>Base Value (m)</b>
d1	Inner octagonal cylinder diameter	20
d2	Outer octagonal cylinder diameter	21
d3	Roof opening diameter	6
d4	Floor opening diameter	0
d5	Upper circular cylinder diameter	16
g1	Gap between deflectors	1
h1	Tangential entry height	4
h2	Octagonal cylinder height	4
h3	Upper cylinder height	0
Z	Domain height	120

Table 5.2: Dimensional specifications for prototype full-scale AVE

Boundary name	Boundary condition
Cubic domain side wall (4)	Pressure Inlet (Atm Pr, Ambient Temp T)
Cubic domain roof	Pressure outlet (Atm Pr, Ambient Temp T)
Cubic domain base	Free-slip wall
Tangential air inlet (8)	Pressure inlet (Atm Pr, Ambient Temp T + $\Delta T$ )
AVE base	No-slip wall (Temp T + $\Delta T$ )
AVE roof opening	Interior
AVE deflectors	No-slip wall
AVE octagonal cylindrical wall	No slip wall
AVE roof	No slip wall

Table 5.3: Boundary conditions for both model-scale and full-scale AVE simulations

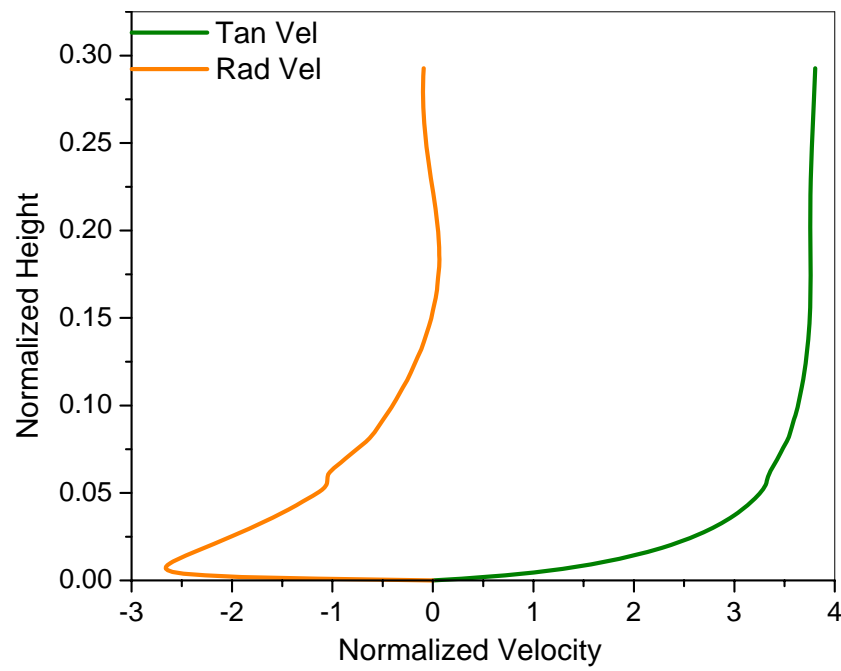


Figure 5.1: The radial and tangential velocity along the height at the core radius of a typical numerically simulated laboratory scale tornado.

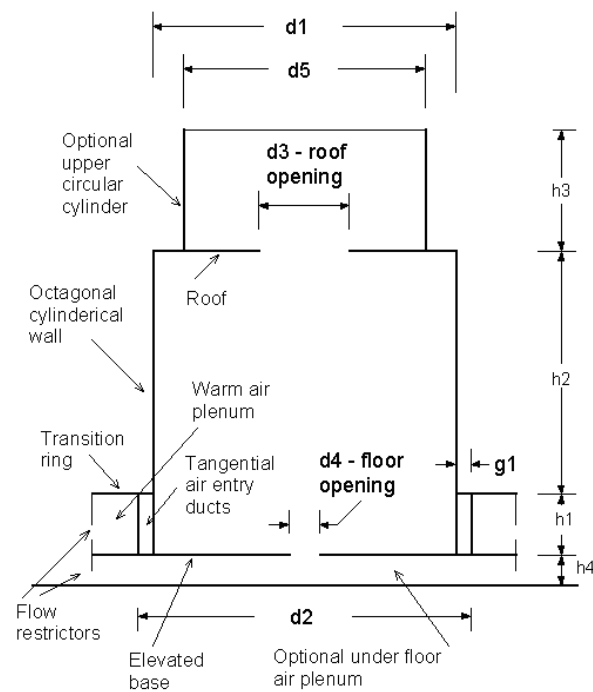


Figure 5.2a: Geometry of the prototype AVE used in the current simulations (Elevation)

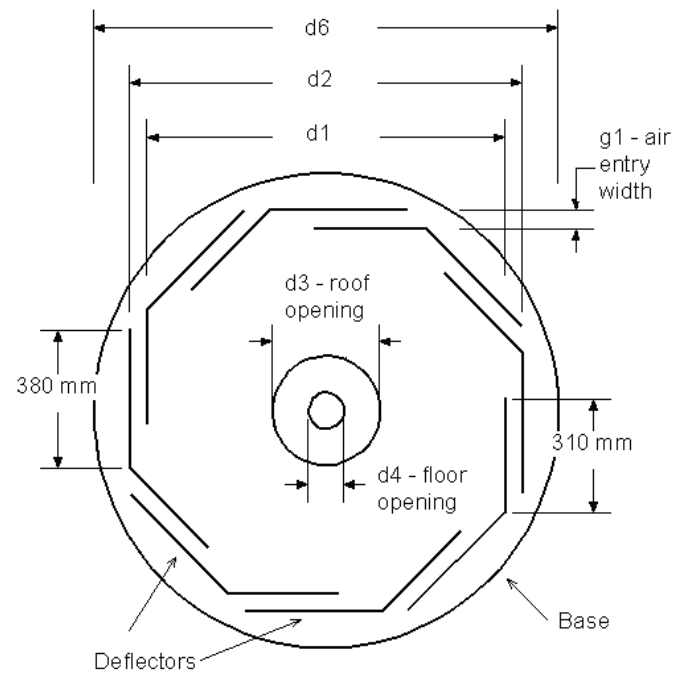


Figure 5.2b: Geometry of the prototype AVE used in the current simulations (Plan view)

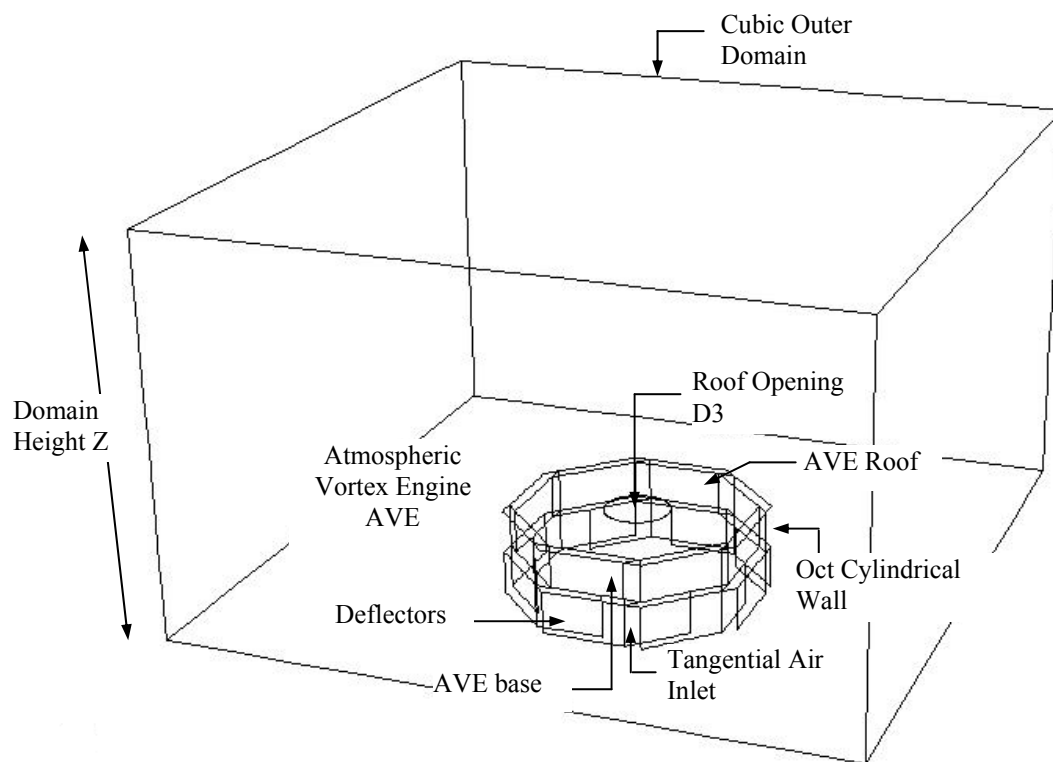


Figure 5.3: The computational domain



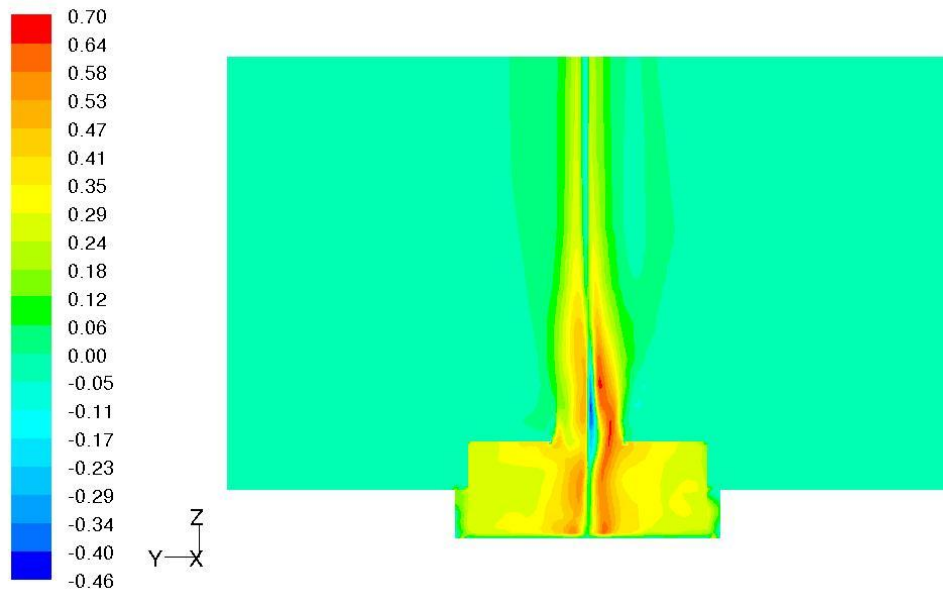


Figure 5.4: The contour plot of tangential velocity (m/s) in the YZ plane for model-scale AVE (Laminar Simulations)

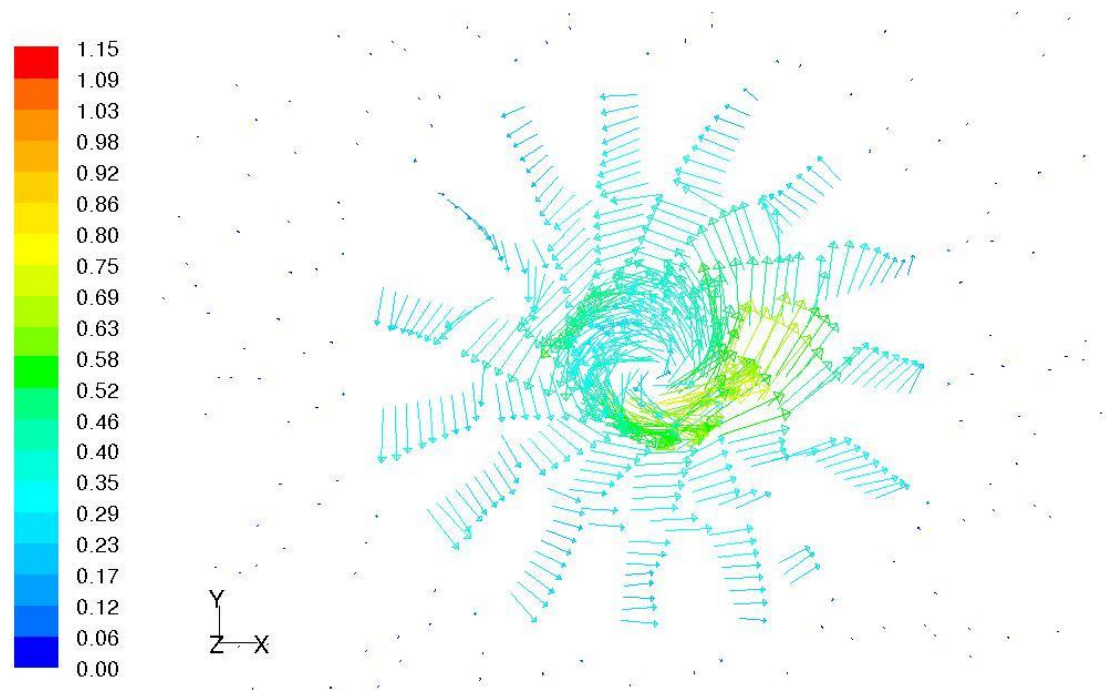


Figure 5.5: The vector plot of velocity magnitude (m/s) in the Z = 0.4m plane for model-scale AVE (Laminar Simulations)

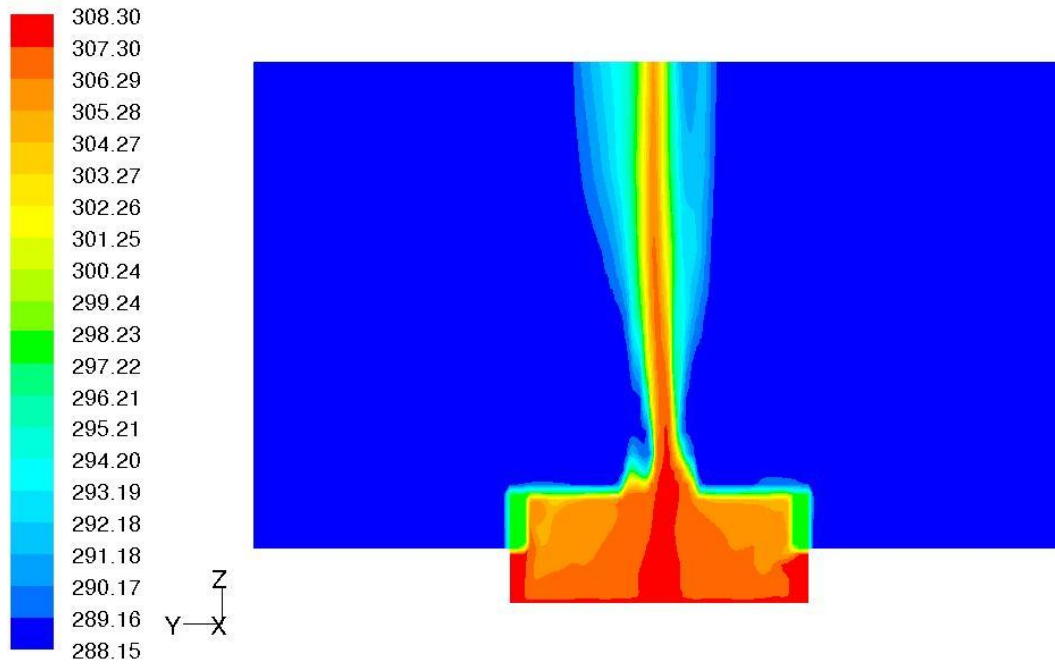


Figure 5.6: The contour plot of temperature (K) in the YZ plane for model-scale AVE (Laminar Simulations)

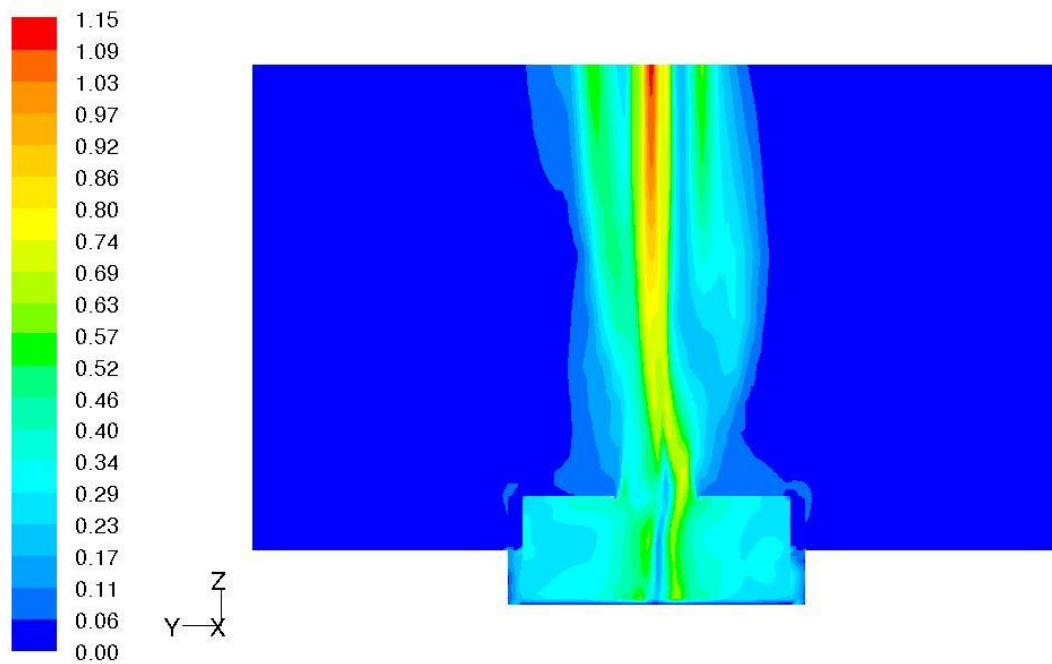


Figure 5.7: The contour plot of velocity magnitude (m/s) in the YZ plane for model-scale AVE (Laminar Simulations)

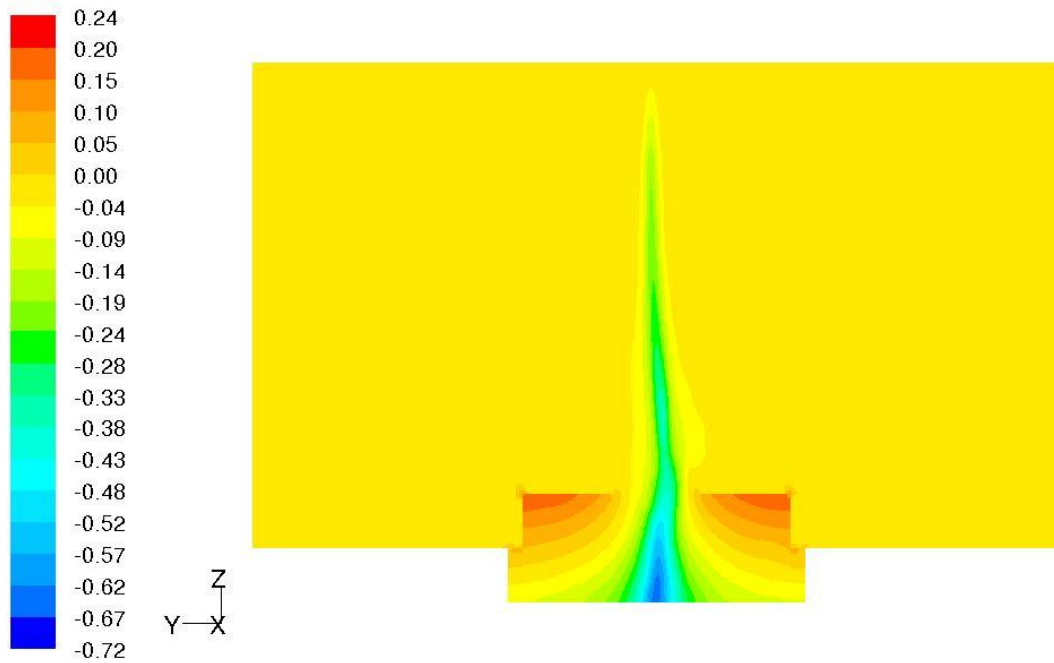


Figure 5.8: The contour plot of static pressure (Pa) in the YZ plane for model-scale AVE (Laminar Simulations)

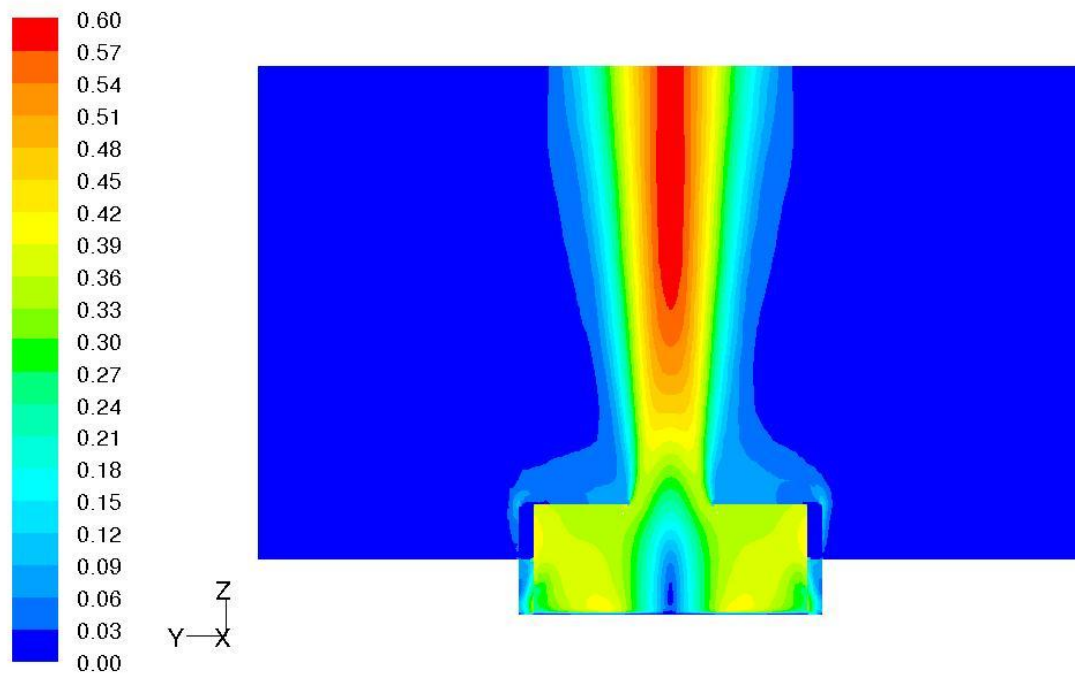


Figure 5.9: The contour plot of velocity magnitude (m/s) in the YZ plane for model-scale AVE (Turbulent Simulations)

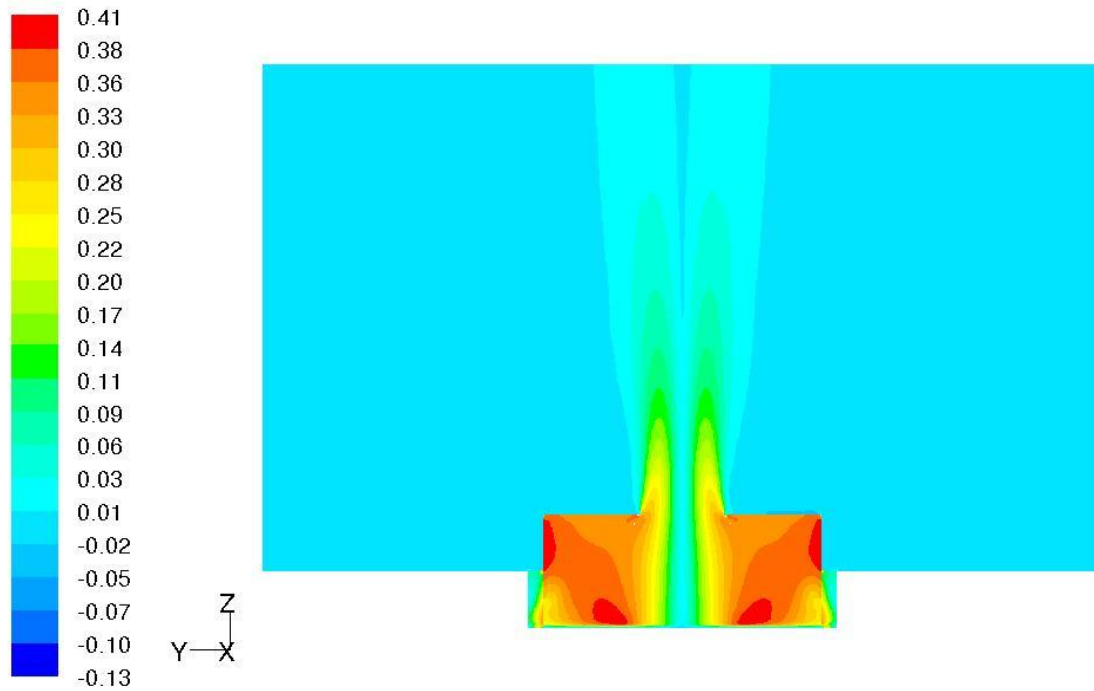


Figure 5.10: The contour plot of tangential velocity (m/s) in the YZ plane for model-scale AVE (Turbulent Simulations)

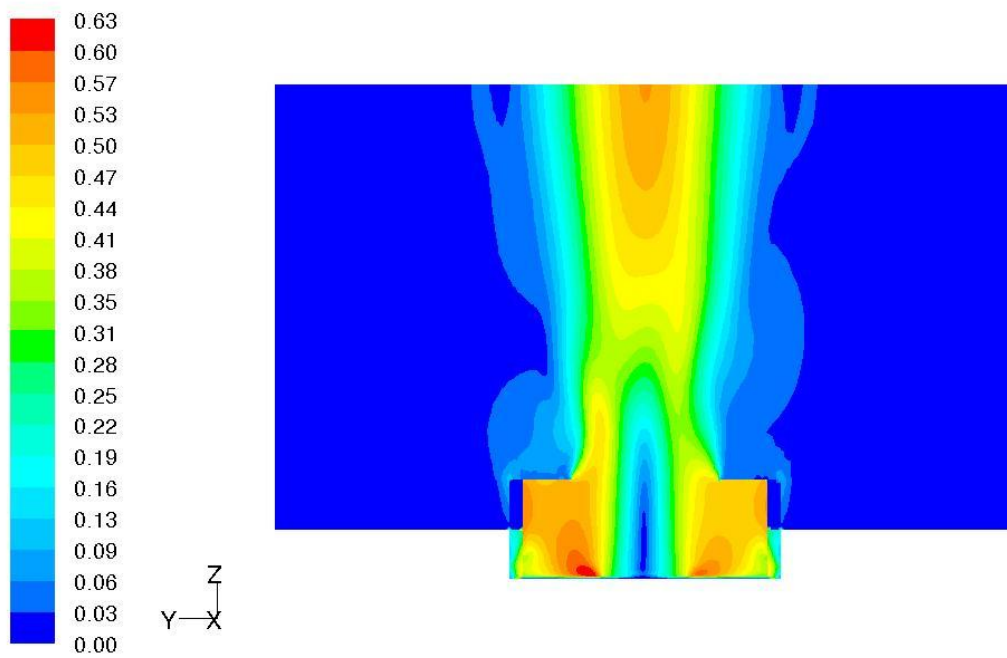


Figure 5.11: The contour plot of velocity magnitude (m/s) in the YZ plane for model-scale AVE with increased roof opening diameter D3 (Turbulent Simulations)

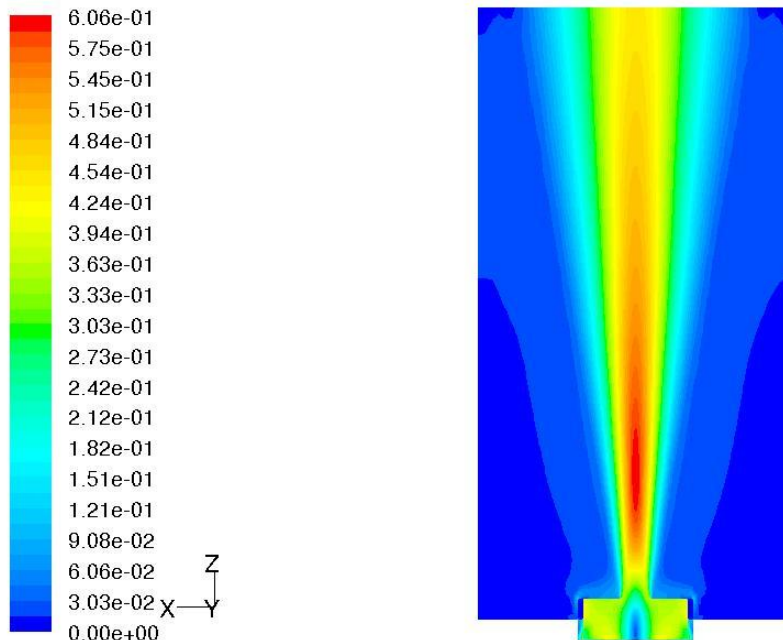


Figure 5.12: The contour plot of velocity magnitude (m/s) in the YZ plane for the extended domain ( $Z = 6000\text{mm}$ ) model-scale AVE (Turbulent Simulations)

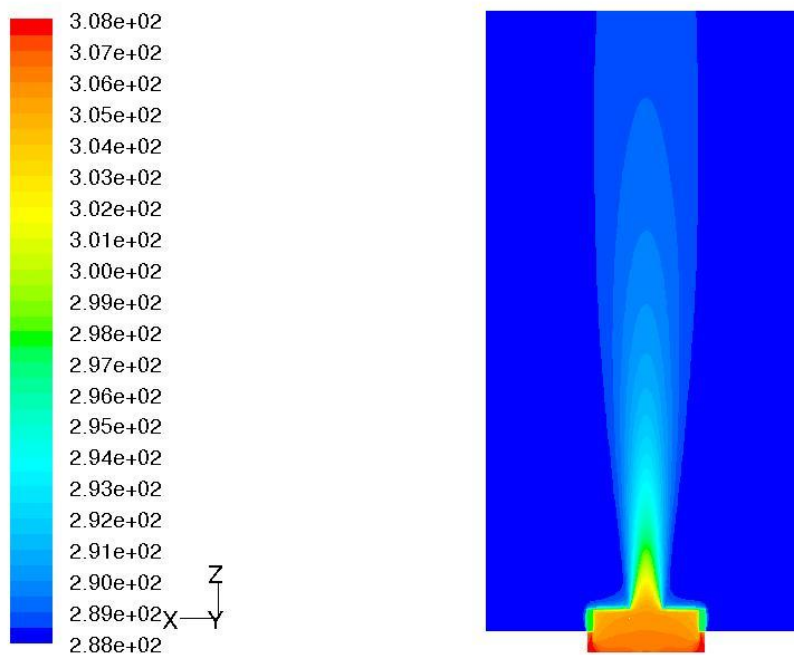


Figure 5.13: The contour plot of temperature (K) in the YZ plane for the extended domain ( $Z = 6000\text{mm}$ ) model-scale AVE (Turbulent Simulations)

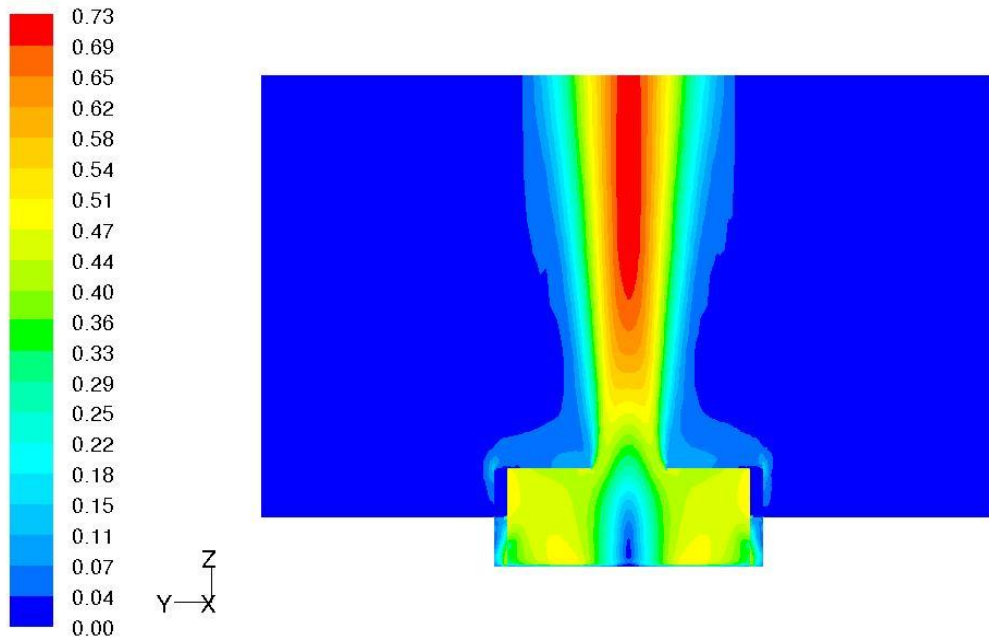


Figure 5.14: The contour plot of velocity magnitude (m/s) in the YZ plane for model-scale AVE with increased temperature difference between the inlet air and ambient air ( $\Delta T = 30$  K) (Turbulent Simulations)

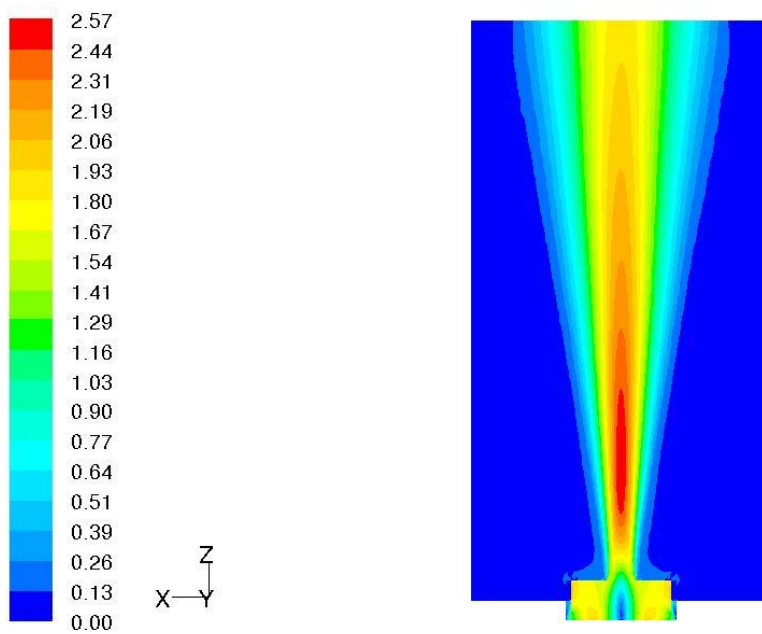


Figure 5.15: The contour plot of velocity magnitude (m/s) in the YZ plane for the full-scale AVE

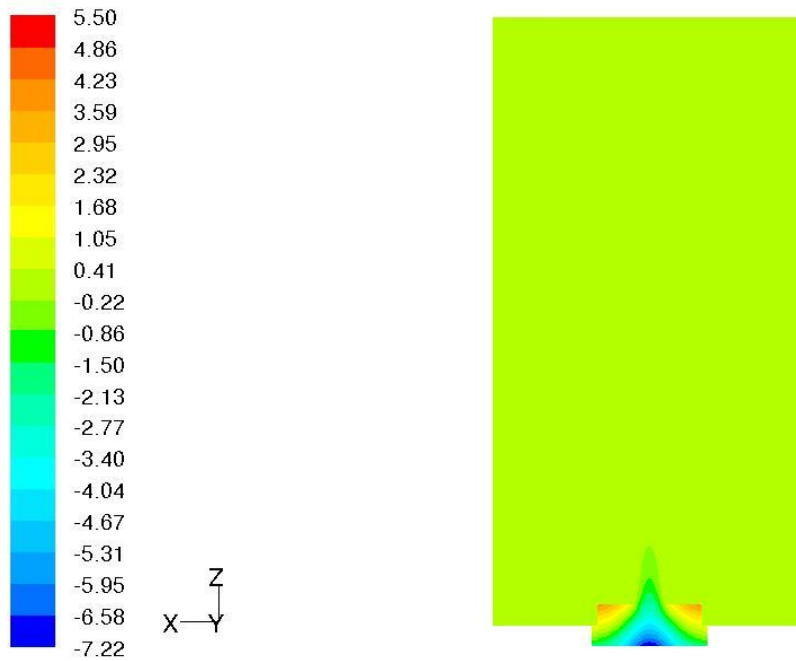


Figure 5.16: The contour plot of static pressure (Pa) in the YZ plane for the full-scale AVE

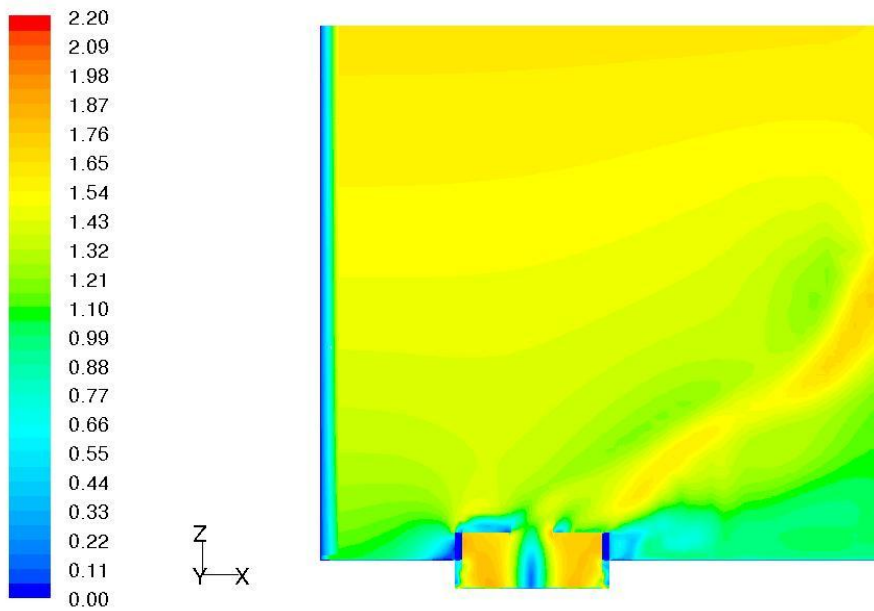


Figure 5.17: The contour plot of velocity magnitude (m/s) in the YZ plane for the full-scale AVE with cross wind

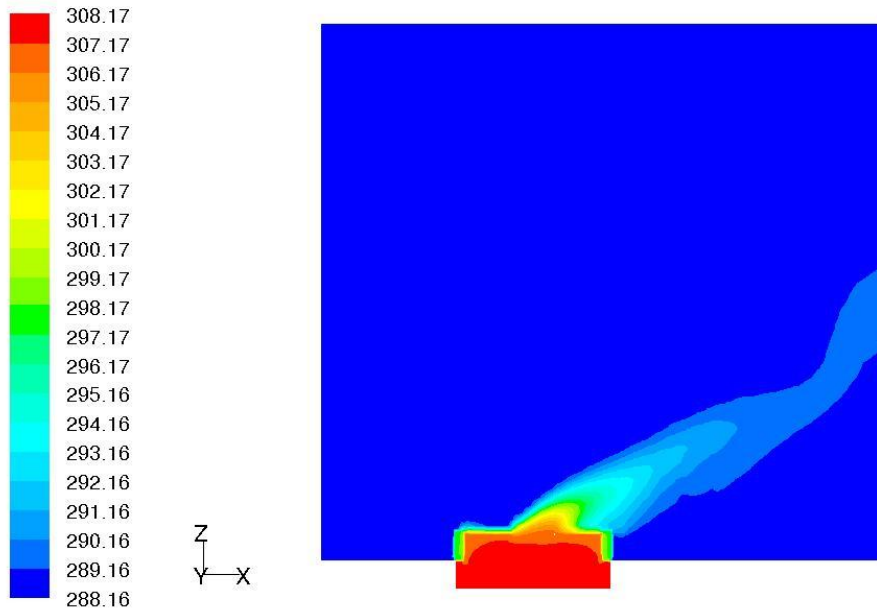


Figure 5.18: The contour plot of temperature (K) in the YZ plane for the full-scale AVE with cross wind

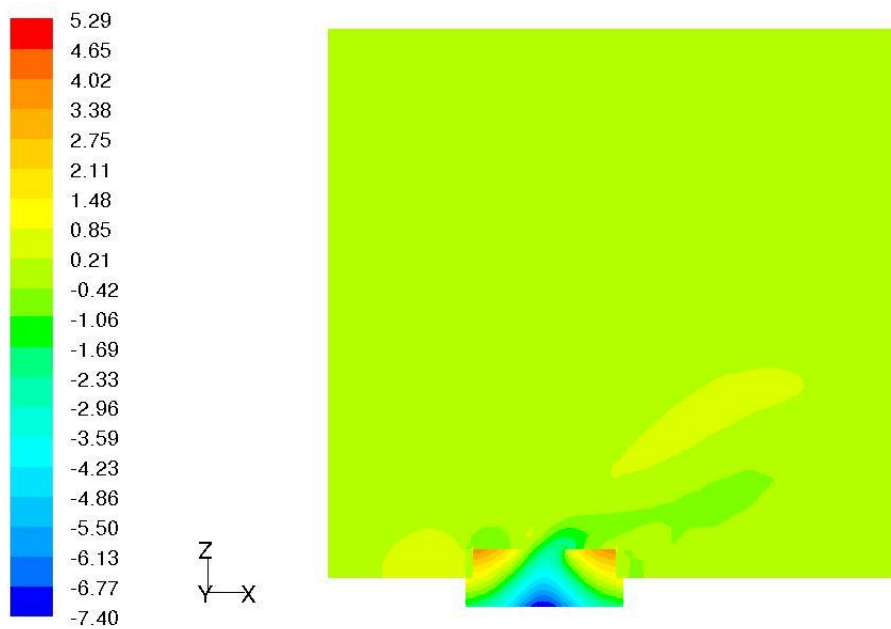


Figure 5.19: The contour plot of static pressure (Pa) in the YZ plane for the full-scale AVE with cross wind



## Chapter 6: Conclusion

The thesis has presented the results of numerical simulation of the flow characteristics of tornado like vortices produced by vortex generators. Three systems were investigated: Ward type Tornado Vortex Chamber (TVC), WinDEEE Dome and Atmospheric Vortex Engine (AVE).

The Computational Fluid Dynamics (CFD) software, Fluent 6.3 was used for the numerical simulations of laboratory scale Ward-type TVC. Reynolds Stress Model (RSM) and Large Eddy Simulation (LES) were used for modeling turbulence. The simulations were done for swirl ratios 0.1 to 2.0. The main observations are given below.

- For swirl ratios  $S < 1.0$ , the RSM model captures all flow features associated with different stages of evolution of the vortex, such as vortex break down (VBD) at  $S=0.28$ , vortex touch down (VTD) at  $S = 0.5$  and two celled vortex for  $S = 0.8$ . However, for  $S \geq 1$  the flow does not capture the transient multiple vortices as the simulation reaches a quasi steady state.
- LES model simulations capture the transient multiple vortices for  $S \geq 1$ . Unlike the past laboratory scale simulations the multiple vortices were observed without adding any external random noise.
- A peak in the mean tangential velocity is observed at  $S \sim 0.5$  when VBD touches the surface. A peak is also observed for  $S = 2.0$  corresponding to occurrence of transient multiple vortices. Also at  $S = 2.0$ , multiple vortices with transient velocities 36% greater than the mean velocities are observed. So the tornado is most destructive during the vortex touch down and multiple vortex stage.
- The height at which maximum tangential velocity occurs decreases initially with increase in swirl ratio ( $S = 0.1-0.5$ ). After VTD occurs for  $S \sim 0.5$ , peaks occur very close to the surface ( $Z/R_0 \leq 0.04$ ).

- The turbulent flow characteristics show that for low swirl ratios the r.m.s. velocities and shear stresses are concentrated within the core near the VBD and follow the VBD as it moves closer to the base surface as the swirl ratio increases. For higher swirl ratios the stresses are concentrated in an annular region around the core.
- For all swirl ratios the peak r.m.s velocities and shear stresses occur at heights and radial distances close to the height and radius at which the maximum tangential velocity occurs. Since the observed maximum tangential velocities are greater than the theoretic thermodynamic speed limit, it is very likely that close to the surface the velocities are influenced by the turbulent interaction of the vortex with the surface.
- The numerical simulation of tornado-like vortex in Ward-type TVC for a complete range of swirl ratios ( $S = 0.1$  to  $2.0$ ) has generated a comprehensive validated data which could serve as database for both modelers and experimenters.

LES simulations using the commercial CFD software Fluent 6.3 was performed to study the effects of translation and surface roughness on laboratory scale vortices in Ward-type TVC.

- The results show a key finding that the effect of translation is not uniform across the swirl ratios. For lower swirl ratios the translation adversely affects the formation of laminar end wall vortex and hence reduces the maximum mean tangential velocity. At high swirl ratios the translation causes local vortex intensification, resulting in a slight increase in the maximum mean tangential velocity.

- A preliminary study on the effects of surface roughness for low roughness case was performed by properly scaling the atmospheric roughness length for Ward-type TVC and using the equivalent sand-grain roughness option in Fluent. Limitations in Fluent software limit this study to only low roughness case and emphasizes the need for a more robust method.
- Effects of surface roughness were studied by modeling physical roughness elements representing a high roughness case (City-centre roughness). The results are closely in line with the past experimental studies. The adoption of proper scaling has not led to any significant differences compared to past studies. The introduction of roughness reduces the mean tangential velocity at all swirl ratios, in other words the roughness causes an effect similar to reducing the swirl ratio.

Numerical simulations for the WindEEE dome were performed and the results show the feasibility for generating axi-symmetric (tornado-like and downburst-like) and straight flow wind profiles.

- Initial simulations on a preliminary design using (SST) KW models show that an array of 8 by 2 fans (0.5 m dia) in the side walls combined with a roof opening of an equivalent diameter of 5m were found to be adequate to produce tornado-like and downburst-like wind profiles.
- Subsequently, design optimizations were introduced to enhance the capability of the dome with respect to straight flow and downburst modes of operations. Numerical analysis using RSM model shows that an array of 8 by 1 fans (0.8 m dia) in 4 side walls combined with an array of 15 by 4 fans (0.8 m dia) on the remaining pair of opposite walls, a pair of removable slotted partition and a top plenum fitted with automated shutter opening (4 m dia) offer adequate choices of inlet and outlet boundary conditions to realize all the three desired flow fields namely tornado-like, downburst-like and straight flow.

- In the downburst simulations the maximum radial velocity is obtained at heights within 5% of the initial jet diameter, as desired. Also the simulations show the production of ring-vortices generally observed in downburst-like flows due to Kelvin-Helmholtz instability.
- In the tornado simulation, a tornado with swirl ratio of approximately  $S = 2$  was simulated and results compare well with observed data from a real tornado and numerically simulated results from a Ward type TVC.
- The WindEEE dome design would evolve further following engineering design implementations. Future plans include the construction of a laboratory scale model of the complete WindEEE dome and experimental analysis of its flow fields. This model will be used to validate (benchmark) the present CFD simulations and to further address issues related to the translation of both tornadoes and downbursts.

The CFD analysis of a model-scale Atmospheric Vortex Engine (AVE) was performed using Fluent 6.3. The results show that the AVE can generate a vortex flow in the atmosphere much above the AVE and the vortex acts as a physical chimney limiting the mixing of surrounding air into the rising plume of hot air.

- For a given geometry, the physical parameter  $\Delta T$  (temperature difference between the inlet air to AVE and ambient air) is the main parameter that controls the strength of the vortex and in turn the power output.
- Increasing the roof opening does not affect the vortex other than causing an increase in the diameter of vortex formed. Future designs may adopt the smaller diameter (30% of deflector diameter ring 'd1') to produce a tight vortex and avoid the straight octagonal cylinder with roof by replacing it with a convergent octagonal cylinder.

- Increasing the domain height does not dissipate the temperature much, and the plume extends till the top of the domain.
- The full scale simulations subjected to cross wind show that the cross wind causes the plume to tilt slightly, but has no adverse impact on the power generation capacity.
- The current full scale simulations do not consider actual temperature gradient present in the atmosphere. Future studies should include the effect of various atmospheric stratifications: stable, unstable and neutral for further accurate results.

## Appendix A: RANS turbulence modeling

In 1895 Reynolds proposed a statistical approach to treat turbulence in fluid flow. According to that the flow variables can be expressed as a sum of mean (time-averaged) and fluctuating parts.

$$u_i = \overline{u_i} + u_i' \quad (A1)$$

$$\phi = \overline{\phi} + \phi' \quad (A2)$$

Where  $\overline{u_i}$  and  $u_i'$  denote the mean and fluctuating velocity components of instantaneous velocity  $u_i$  and  $\phi$  denotes scalars such as pressure, energy etc. Substituting the above forms of equations for flow variables in instantaneous continuity and momentum equations and taking a time average gives the Reynolds Averaged Navier-Stokes (RANS) equations:

$$\frac{\partial \overline{u_i}}{\partial x_i} = 0 \quad (A3)$$

$$\rho \frac{\partial \overline{u_i}}{\partial t} + \rho \overline{u_j} \frac{\partial \overline{u_i}}{\partial x_j} = -\frac{\partial \overline{p}}{\partial x_i} + \frac{\partial}{\partial x_j} \left( 2 \mu S_{ij} - \overline{\rho u_i' u_j'} \right) \quad S_{ij} = \frac{1}{2} \left( \frac{\partial \overline{u_i}}{\partial x_j} + \frac{\partial \overline{u_j}}{\partial x_i} \right) \quad (A4)$$

The term  $\overline{\rho u_i' u_j'}$  is called Reynolds stress tensor. In the above set of equations we have ten unknown variables (four unknown mean flow properties ( $p$ ,  $u_1$ ,  $u_2$ , and  $u_3$ ) and six Reynolds stress components) and only four sets of equation, so the system of equations is not closed. In order to close the system of equations of motion, we require additional equations. Different closure models are available and brief descriptions of the models used in this thesis are given below. Detailed descriptions are given in Fluent, 2006.

### **$k\varepsilon$ Model:**

In  $k\varepsilon$  model the Reynolds stresses are related to the velocity gradients using the Boussinesq hypothesis shown in Equation A5.

$$-\overline{\rho u_i u_j} = \mu_t \left( \frac{\partial u_i}{\partial x_j} + \frac{\partial u_j}{\partial x_i} \right) - \frac{2}{3} \left( \rho k + \mu_t \frac{\partial u_k}{\partial x_k} \right) \delta_{ij} \quad (\text{A5})$$

(In the above equations as well as the following ones, the bar over mean components has been omitted) The eddy viscosity  $\mu_t$  is computed using turbulent kinetic energy  $k$  and dissipation rate  $\varepsilon$  as shown in Equation A6. Two additional transport equations shown in Equations A7 and A8 are solved to calculate  $k$  and  $\varepsilon$ .

$$\mu_t = \rho C_\mu \frac{k^2}{\varepsilon} \quad (\text{A6})$$

$$\frac{\partial}{\partial t}(\rho k) + \frac{\partial}{\partial x_i}(\rho k u_i) = \frac{\partial}{\partial x_j} \left[ \left( \mu + \frac{\mu_t}{\sigma_k} \right) \frac{\partial k}{\partial x_j} \right] + G_k - \rho \varepsilon \quad (\text{A7})$$

$$\frac{\partial}{\partial t}(\rho \varepsilon) + \frac{\partial}{\partial x_i}(\rho \varepsilon u_i) = \frac{\partial}{\partial x_j} \left[ \left( \mu + \frac{\mu_t}{\sigma_\varepsilon} \right) \frac{\partial \varepsilon}{\partial x_j} \right] + C_{1\varepsilon} \frac{\varepsilon}{k} G_k - C_{2\varepsilon} \rho \frac{\varepsilon^2}{k} \quad (\text{A8})$$

In the above equations  $G_k$  is the generation of turbulence kinetic energy due to the mean velocity gradients,  $C_{1\varepsilon} = 1.44$ ,  $C_{2\varepsilon} = 1.92$  and  $C_\mu = 0.09$  are constants.  $\sigma_k = 1.0$  and  $\sigma_\varepsilon = 1.3$  are the turbulent Prandtl numbers for  $k$  and  $\varepsilon$ .

### (SST) $k\omega$ Model:

(SST)  $k\omega$  model also uses the Boussinesq hypothesis and is a combination of both  $k\omega$  and  $k\varepsilon$  models. It uses a blending function to activate  $k\omega$  model in the near-wall region and  $k\varepsilon$  model in the far field. The eddy viscosity is calculated as a function of turbulence kinetic energy ( $k$ ) and specific dissipation rate ( $\omega$ ), which are solved using transport equations given below

$$\frac{\partial}{\partial t}(\rho k) + \frac{\partial}{\partial x_i}(\rho k u_i) = \frac{\partial}{\partial x_j} \left[ \Gamma_k \frac{\partial k}{\partial x_j} \right] + \tilde{G}_k - Y_k \quad (\text{A9})$$

$$\frac{\partial}{\partial t}(\rho \omega) + \frac{\partial}{\partial x_i}(\rho \omega u_i) = \frac{\partial}{\partial x_j} \left[ \Gamma_\omega \frac{\partial \omega}{\partial x_j} \right] + G_\omega - Y_\omega + D_\omega \quad (\text{A10})$$

Where  $G_k$  is the generation of turbulence kinetic energy due to mean velocity gradient,  $G_\omega$  represents the generation of  $\omega$ ,  $Y_k$  and  $Y_\omega$  represents the dissipation of  $k$  and  $\omega$  due to turbulence.  $D_\omega$  is the cross-diffusion term introduced due to the transformation of the  $k\varepsilon$  model into equations based on  $k$  and  $\omega$ .  $\Gamma_k$  and  $\Gamma_\omega$  are the effective diffusivity and calculated as given in Equations A11 and A12.

$$\Gamma_k = \mu + \frac{\mu_t}{\sigma_k} \quad (\text{A11})$$

$$\Gamma_\omega = \mu + \frac{\mu_t}{\sigma_\omega} \quad (\text{A12})$$

Where  $\mu_t$  is the eddy viscosity,  $\sigma_k$  and  $\sigma_\omega$  are the turbulent Prandtl numbers for  $k$  and  $\varepsilon$ . These are calculated as function of  $k$ ,  $\omega$  and blending functions.

### Reynolds Stress Model:



Reynolds Stress Model (RSM) closes the system of equations by using transport equations for each of the six terms in the Reynolds stress tensor and a scale-determining equation (transport equation for dissipation rate  $\varepsilon$ ). So the RSM models is also called seven equation model.

Reynolds Stress Transport Equation:

The Equation A13 gives the transport equation of Reynolds stresses where  $C_{ij}$ ,  $D_{T,ij}$ ,  $D_{L,ij}$ ,  $P_{ij}$ ,  $G_{ij}$ ,  $\phi_{ij}$ ,  $\varepsilon_{ij}$ ,  $F_{ij}$  and  $S_{user}$  are convection, turbulent diffusion, molecular diffusion, stress production, buoyancy production, pressure strain, dissipation, production by system rotation and user-defined source terms, respectively (Equations A14-A21). Among these  $D_{T,ij}$ ,  $G_{ij}$ ,  $\phi_{ij}$  and  $\varepsilon_{ij}$  require modeling to close the equations. The current simulations do not consider temperature gradient in the flow so the modeling of buoyancy production term ( $G_{ij}$ ) is not presented here.

$$\frac{\partial}{\partial t} \left( \overline{\rho u'_i u'_j} \right) + C_{ij} = D_{T,ij} + D_{L,ij} + P_{ij} + G_{ij} + \phi_{ij} - \varepsilon_{ij} + F_{ij} + S_{user} \quad (A13)$$

Where

$$C_{ij} = \frac{\partial}{\partial x_k} \left( \rho u'_k \overline{u'_i u'_j} \right) \quad (A14)$$

$$D_{T,ij} = - \frac{\partial}{\partial x_k} \left( \overline{\rho u'_i u'_j u'_k} + p \left( \overline{\delta_{kj} u'_i} + \overline{\delta_{ik} u'_j} \right) \right) \quad (A15)$$

$$D_{L,ij} = \frac{\partial}{\partial x_k} \left[ \mu \frac{\partial}{\partial x_k} \left( \overline{u'_i u'_j} \right) \right] \quad (A16)$$

$$P_{ij} = -\rho \left( \overline{u'_i u'_k} \frac{\partial u'_j}{\partial x_k} + \overline{u'_j u'_k} \frac{\partial u'_i}{\partial x_k} \right) \quad (A17)$$

$$G_{ij} = -\rho\beta(g_i \overline{u'_j \theta} + g_j \overline{u'_i \theta}) \quad (A18)$$

$$\varphi_{ij} = \overline{p \left( \frac{\partial u'_i}{\partial x_j} + \frac{\partial u'_j}{\partial x_i} \right)} \quad (A19)$$

$$\varepsilon_{ij} = 2\mu \overline{\left( \frac{\partial u'_i}{\partial x_k} \frac{\partial u'_j}{\partial x_k} \right)} \quad (A20)$$

$$F_{ij} = -2\rho\rho_k \left( \overline{u'_j u'_m} \varepsilon_{ikm} + \overline{u'_i u'_m} \varepsilon_{jkm} \right) \quad (A21)$$

Modeling Turbulent Diffusive Transport:

The turbulent diffusion term ( $D_{T,ij}$ ) given in Equation A15 is modeled as shown in Equation A22 and the constant  $\sigma_k = 0.82$ . The eddy viscosity  $\mu_t$  is modeled as shown in Equation A23, where  $C_\mu = 0.09$ .

$$D_{T,ij} = \frac{\partial}{\partial x_k} \left( \frac{\mu_t}{\sigma_k} \frac{\partial \overline{u'_i u'_j}}{\partial x_k} \right) \quad (A22)$$

$$\mu_t = \rho C_\mu \frac{k^2}{\varepsilon} \quad (A23)$$

Modeling the Pressure-Strain Term:

‘Linear Pressure-Strain model’ option in Fluent is used in the current simulations. This model is used to model the pressure-strain term ( $\varphi_{ij}$ ) given in Equation A19. The pressure-strain term is decomposed into a slow pressure-strain term, rapid pressure-strain term and a wall-reflection term as shown in Equation A24. The slow pressure-strain term

is modeled as shown in Equation A25 with constant  $C_1 = 1.8$ . The rapid pressure-strain term is modeled as shown in Equation A26, where  $C_2 = 0.6$ ,  $C_{ij}$ ,  $P_{ij}$ ,  $G_{ij}$  and  $F_{ij}$  are as defined in Equations A14, A17, A18 and A21,  $P = \frac{1}{2} P_{kk}$ ,  $G = \frac{1}{2} G_{kk}$ ,  $C = \frac{1}{2} C_{kk}$  (Note  $G_{ij}$ ,  $G_{kk}$ : effects of buoyancy are not considered in the current simulations). The wall-reflection term is modeled as shown in Equation A27, where  $C_1' = 0.5$ ,  $C_2' = 0.3$ ,  $n_k$  is the  $x_k$  component of the unit normal to the wall,  $d$  is the normal distance to the wall and  $C_1 = C_\mu^{3/4}/\kappa$ , where  $C_\mu = 0.09$  and the von Karman constant  $\kappa = 0.4187$ .

$$\varphi_{ij} = \varphi_{ij,1} + \varphi_{ij,2} + \varphi_{ij,w} \quad (A24)$$

$$\varphi_{ij,1} = -C_1 \rho \frac{\varepsilon}{k} \left[ \overline{u_i' u_j'} - \frac{2}{3} \delta_{ij} k \right] \quad (A25)$$

$$\varphi_{ij,2} = -C_2 \left[ (P_{ij} + F_{ij} + G_{ij} - C_{ij}) - \frac{2}{3} \delta_{ij} (P + G - C) \right] \quad (A26)$$

$$\begin{aligned} \varphi_{ij,w} = & -C_1' \frac{\varepsilon}{k} \left( \overline{u_k' u_m'} n_k n_m \delta_{ij} - \frac{3}{2} \overline{u_i' u_k'} n_j n_k - \frac{3}{2} \overline{u_j' u_k'} n_i n_k \right) \frac{C_1 k^{3/2}}{\varepsilon d} \\ & + C_2' \left( \varphi_{km,2} n_k n_m \delta_{ij} - \frac{3}{2} \varphi_{ik,2} n_j n_k - \frac{3}{2} \varphi_{jk,2} n_i n_k \right) \frac{C_1 k^{3/2}}{\varepsilon d} \end{aligned} \quad (A27)$$

Modeling the Turbulent Kinetic Energy:

The turbulent kinetic energy ( $k$ ) needed for modeling in the above equations (Equations A15 and A17) is obtained from Equation A28.

$$k = \frac{1}{2} \overline{u_i' u_i'} \quad (A28)$$

Modeling the Dissipation Rate:

The dissipation tensor ( $\epsilon_{ij}$ ) is modeled as shown in Equation A29. The current simulations are for incompressible flows, so the ‘dilatation dissipation’ term  $Y_M$  included to account for compressibility effect on turbulence is neglected. The scalar dissipation rate ( $\epsilon$ ) in Equation A29 is computed with transport equation shown in Equation A30 with constants  $\sigma_\epsilon = 1.0$ ,  $C_{\epsilon 1} = 1.44$ ,  $C_{\epsilon 2} = 1.92$  and the buoyancy effects on turbulence ( $G_{ii}$ ) is neglected in the current simulations.

$$\epsilon_{ij} = \frac{2}{3} \delta_{ij} (\rho \epsilon + Y_M) \quad (A29)$$

$$\frac{\partial}{\partial t} (\rho \epsilon) + \frac{\partial}{\partial x_i} (\rho \epsilon u_i) = \frac{\partial}{\partial x_j} \left[ \left( \mu + \frac{\mu_t}{\sigma_\epsilon} \right) \frac{\partial \epsilon}{\partial x_j} \right] C_{\epsilon 1} \frac{1}{2} (P_{ii} + C_{\epsilon 3} G_{ii}) \frac{\epsilon}{k} - C_{\epsilon 2} \rho \frac{\epsilon^2}{k} + S_\epsilon \quad (A30)$$

### Reference:

FLUENT 6.3 User’s guide, 2006. Fluent Inc, Lebanon, USA

## Appendix B: LES turbulence modeling

In turbulent flows the large eddies are generally dependent on the geometry and small scale eddies tend to be more isotropic and less dependent on the geometry. Large Eddy Simulation (LES) is based on the above observation, so in LES the large eddies are resolved directly and only the small eddies are modeled. In the current thesis the CFD software Fluent 6.3 was used for LES simulation and a brief description of the model is given here. Detailed descriptions are given in Fluent, 2006.

The filtering used in separating the large scale and small scale motions in LES is shown in Equation B1.

$$\bar{\phi}(X) = \int_D \phi(X') G(X, X') dX' \quad (B1)$$

Where  $G$  is the filter function and  $D$  is the fluid domain. Every filter has an associated length scale  $\Delta$ . In rough sense, eddies of size larger than  $\Delta$  are large eddies and are resolved directly while those smaller than  $\Delta$  are small eddies and are modeled. In Fluent the finite-volume discretization is used as filter and the filter function is as shown in Equation B2 where  $V$  is the volume of the computational cell.

$$G(X, X') = \begin{cases} 1/V, & X' \in V \\ 0, & X' \text{ otherwise} \end{cases} \quad (B2)$$

Applying the filtering to the continuity and Navier-Stokes equation results in the following equations

$$\frac{\partial \bar{\rho}}{\partial t} + \frac{\partial (\bar{\rho} \bar{u}_i)}{\partial x_i} = 0 \quad (B3)$$

$$\frac{\partial(\rho \bar{u}_i)}{\partial t} + \frac{\partial(\rho \bar{u}_i \bar{u}_j)}{\partial x_j} = \frac{\partial}{\partial x_j} \left( \mu \frac{\partial \sigma_{ij}}{\partial x_j} \right) - \frac{\partial \bar{p}}{\partial x_i} + \frac{\partial T_{ij}}{\partial x_j}, \text{ Where } \sigma_{ij} = \mu \left( \frac{\partial \bar{u}_i}{\partial x_j} + \frac{\partial \bar{u}_j}{\partial x_i} \right) - \frac{2}{3} \mu \frac{\partial \bar{u}_l}{\partial x_l} \delta_{ij} \quad (\text{B4})$$

Where  $T_{ij}$  is the subgrid scale stress and expanded in Equation B5. Fluent employs Boussinesq hypothesis to model subgrid scale stress and computes it from Equation B6. Where  $S_{ij}$  is the rate-of-strain tensor and  $\mu_t$  is the subgrid scale turbulent viscosity.

$$T_{ij} \equiv \overline{\rho u_i u_j} - \rho \bar{u}_i \bar{u}_j \quad (\text{B5})$$

$$T_{ij} - \frac{1}{3} T_{kk} \delta_{ij} = -2 \mu_t \bar{S}_{ij} \quad \bar{S}_{ij} \equiv \frac{1}{2} \left( \frac{\partial \bar{u}_i}{\partial x_j} + \frac{\partial \bar{u}_j}{\partial x_i} \right) \quad (\text{B6})$$

The current simulations use the ‘Dynamic Smagorinsky-Lilly model’ option in Fluent to model the eddy viscosity and modeling is shown in Equation B7. Where  $L_s$  is the mixing length for the subgrid scales and is computed using Equation B8. In Equation B8,  $\kappa$  is the Von Karman constant,  $d$  is the distance to the closest wall and  $C_s$  is a dynamically calculated constant.

$$\mu_t = \rho L_s^2 \sqrt{2 \bar{S}_{ij} \bar{S}_{ij}} \quad (\text{B7})$$

$$L = \min(\kappa d, C_s V^{1/3}) \quad (\text{B8})$$

## Reference:

FLUENT 6.3 User’s guide, 2006. Fluent Inc, Lebanon, USA

## Appendix C: Rayleigh number calculation for AVE simulations

Rayleigh number (Ra):

$$Ra = \frac{g\beta(T_s - T_\infty)x^3}{\nu\alpha}$$

Variables	Model-scale AVE	Full-scale AVE
AVE base diameter: X (m)	1	20
Inlet air temperature: $T_s$ (K)	308.16	308.16
Ambient temperature: $T_\infty$ (K)	288.16	288.16
Film Temp: $T_f = \frac{T_s + T_\infty}{2}$	298.16	298.16
Thermal expansion coefficient (1/K): $\beta = \frac{1}{T_f}$	$3.35 \times 10^{-3}$	$3.35 \times 10^{-3}$
Kinematic viscosity at $T_f$ : $\nu$ (m <sup>2</sup> /s)	$1.5 \times 10^{-5}$	$1.5 \times 10^{-5}$
Thermal diffusivity at $T_f$ : $\alpha$ (m <sup>2</sup> /s)	$2.112 \times 10^{-3}$	$2.112 \times 10^{-3}$
Ra	$2.06 \times 10^9$	$1.648 \times 10^{13}$

Boussinesq model:

The Boussinesq approximation is only valid when  $\beta(T - T_0) \ll 1$ . In the current simulations the temperature difference between actual and ambient temperature  $\Delta T = (T - T_0) = (308.16 - 288.16) = 20\text{K}$  and the thermal expansion coefficient  $\beta = 3.35 \times 10^{-3} \text{ 1/K}$ , therefore  $\beta(T - T_0) = 0.067$ .

## Curriculum Vitae

**Name:** Diwakar Natarajan

**Education:** Bachelor of Technology - Jun 02  
Pondicherry University, Pondicherry, India

Master of Engineering - Dec 05  
Birla Institute of Technology and Science – Pilani, Rajasthan,  
India

Doctor of Philosophy - Jan 11  
University of Western Ontario, London, ON, Canada

**Awards:** Govt. of Pondicherry prize for academic excellence:  
undergraduate studies, Pondicherry, India, 2002.

**Related Work** Teaching Assistant - Jan 07 – May 10  
**Experience:** University of Western Ontario, London, ON, Canada

**Publication:** Natarajan, D., and Hangan, H., “Preliminary numerical  
simulation of axi-symmetric flows in WindEEE dome facility”,  
The Firth International Symposium on Computational Wind  
Engineering (CWE2010), Chapel Hill, North Carolina, USA  
May 23-27, 2010.



Natarajan, D., and Hangan, H., “Numerical study on the effects of surface roughness on tornado-like flows”, 11<sup>th</sup> Americas Conference on Wind Engineering (11ACWE), San Juan, Puerto Rico, June 22-26, 2009.

Natarajan, D., Kim, J., and Hangan, H.,”A CFD study of artificial atmospheric vortex generator”, Boundary Layer Wind Tunnel Report ‘BLWT-SS22-2007’, London, ON, Canada, Jun 2007.